12-2024

Constraining Decadal-Scale Erosion and Delivery of Post-Wildfire Debris Flow Deposits

Casey Langstroth
Utah State University

CONSTRAINING DECADAL-SCALE EROSION AND DELIVERY OF POST-WILDFIRE DEBRIS FLOW DEPOSITS

by

Casey Langstroth

A thesis submitted in partial fulfillment
of the requirements of the degree

of

MASTER OF SCIENCE

in

Watershed Science

Approved:

_____	_____
Patrick Belmont, Ph.D. Major Professor	Brendan Murphy, Ph.D. Co-Advisor
_____	_____
Belize Lane, Ph.D. Committee Member	D. Richard Cutler, Ph.D. Vice Provost of Graduate Studies

UTAH STATE UNIVERSITY
Logan, Utah

2024

ABSTRACT

Constraining Decadal-scale Erosion and Delivery

of Post-wildfire Debris Flow Deposits

by

Casey Langstroth, Master of Science

Utah State University, 2024

Major Professors: Dr. Patrick Belmont and Dr. Brendan Murphy
Department: Watershed Sciences

Debris flows generated after wildfire pose significant hazards, including increased sedimentation in river networks, degradation of water quality, and accumulated sediment in downstream reservoirs. Despite an abundance of prior research investigating post-fire debris flows focused on their probability of generation and initial conditions (e.g., depositional volumes and grain size), there remains a significant knowledge gap related to the evolution of these deposits after their initial emplacement. To investigate the temporal evolution of debris flow deposits (i.e., the erosion and delivery of sediment to river networks), two questions must be first be addressed: 1) How does sediment delivery to river networks from post-wildfire debris flow deposits change over time? and 2) Which local, reach-scale hydrogeomorphic features influence the relative magnitude of debris flow sediment delivery over time? Employing a combination of fieldwork and remote sensing analysis, we have compiled a dataset quantifying volume loss over time from 58 identified post-fire debris flow deposits across the state of Utah. From our analysis, we identified three processes responsible for eroding debris flow deposits: lateral toe erosion resulting from fluvial processes of the axial river, tributary channel incision through the

deposit, and surface deflation of the deposit resulting from runoff and sheetwash processes. We analyzed factors influencing the initial delivery of deposits to the axial river, the relative volume loss due to each of the dominant erosional processes, and the variability in temporal trends due to each process. Additionally, we evaluated existing models of initial delivery and developed a modified approach, the Debris Flow Delivery Potential model, which produced more accurate estimates of initial sediment delivery to the river network. We verified our initial hypothesis that volume loss of debris flow deposits that are primarily eroding by toe erosion can be reasonably modeled with an exponential decay function. Ultimately, this work represents an in-depth investigation into the morphologic influence of debris flow deposits, valley bottom, and channel on decadal-scale sediment delivery of post-wildfire debris flows to rivers. The datasets produced through this work will help improve understanding of how large sediment pulses may influence downstream ecological habitat and impact reservoirs or other infrastructure.

(151 pages)

PUBLIC ABSTRACT

Constraining Decadal-scale Erosion and Delivery

of Post-wildfire Debris Flow Deposits

Casey Langstroth

Debris flows generated from wildfire pose significant risk to increased sedimentation to instream river networks, degradation of water quality, and accumulated sediment behind downstream reservoirs. Despite an abundance of research investigating the probability of debris flow generation, the constraints on deposit initial volume, and most recently the initial grain size distribution, there remains a significant knowledge gap in understanding the temporal scale at which debris flows supply sediment to river networks after deposition. To provide reliable estimates of sediment delivery from debris flow deposits over time, two important metrics must be constrained: 1) how does sediment delivery to river networks from post-wildfire debris flow deposits change over time, and 2) which local, reach-scale hydrogeomorphic features influence the relative magnitude of debris flow sediment delivery over time? With a combination of remote analysis and fieldwork of 58 identified debris flows in the state of Utah, we have compiled a dataset representing volume loss from debris flow deposits through time.

Three erosional processes are responsible for removing debris flow sediment over time. The axial river removes the largest magnitude of sediment from post-wildfire debris flow deposits due to fluvial processes at the toe of the deposit. We additionally observed channel incision on the deposit surface via tributary channels emerging from the generating tributary catchment. Lastly, we inferred a third process, surface deflation, that

results in volume loss from the debris flow deposit without any change to the deposit area. We found that initial volume loss is heavily driven by channel confinement and long-term erosion by the axial river can be modeled as an exponential decay function. Additionally, we proposed a new metric, the Debris Flow Delivery Potential, as a method to estimate the probability that a debris flow deposit would be initially delivered into the axial river. The framework presented here is aimed to improve long-term hazard assessment models regarding post-wildfire debris flow mitigation and planning.

ACKNOWLEDGMENTS

This research was funded by the Joint Fire Science Program and Utah Department of Transportation. Additionally, this research could not have been done without the support of my field technician, Quinn Olpin. Thank you for embarking on this adventure of a thesis with me, and for always having the best attitude, even if you spent 10+ hours counting pebbles in a stream in the hot sun. I cannot thank my advisors, Dr. Patrick Belmont and Dr. Brendan Murphy, enough for their amazing guidance and enthusiasm for this project. These two have taught me how to be a better scientist by encouraging my ambitions and giving me the space and confidence to share my ideas. Additionally, I want to thank Dr. Scott David, who was instrumental in helping me develop my coding skills, presenting my data, and spending the time to help me think about my predictive models. Lastly, I want to thank our broader post-wildfire research group for their collaborative and welcomed feedback through every step of this process.

In November of 2023, I broke my leg in a spectacular display of football athleticism. I cannot thank the entire community of Logan, QCNR, and the Watershed Sciences Department enough for their amazing support as I healed. Patrick, I will never forget your kind delivery of mashed potatoes to the ER. Thank you to my friends and family for listening to me ramble about debris flows and sediment transport for the last two years. Specifically, thank you to my partner Andrew for his constant enthusiasm and interest in this project, as well as helping me wash my hair and keeping me fed while I was on crutches, recovering from surgery, and finishing my thesis.

Casey Langstroth

CONTENTS

Page

LIST OF TABLES

Page

LIST OF FIGURES

Page

LIST OF EQUATIONS

Page

INTRODUCTION

Water security, or the availability of clean water for humans and ecosystems, is increasingly threatened by climate change and other natural and anthropogenic disturbances throughout the world (Stringer et al., 2021; Daneshi et al., 2020; Brown et al., 2019). In the western United States, communities are heavily dependent on reservoirs for drinking water, agricultural use, and energy via hydropower (Graf et al., 2010; Dettinger et al., 2015). As populations in the western states continue to grow, increased demand for water resources inevitably imposes stress on water infrastructure (Dettinger et al., 2015). Climate change has increased global temperatures, enhanced drought and aridity, and the increased the intensity and frequency of heavy rainfall and extreme weather events (USGCRP, 2018; Overpack and Udall, 2020; Dettinger et al., 2015). The combination of climate change and historical water, fire, and forest management practices make wildfire a considerable threat to water security for humans and ecosystems in many parts of the world, including western North America (Murphy et al., 2018; Martin, 2016; Hallema et al., 2018).

Climate change has contributed to increased aridity and decreased snowpack, while in addition, historical wildfire suppression has unnaturally increased fuel loads in forested watersheds (Westerling et al., 2006; Boisramé et al., 2022). Altogether, these factors are responsible for projected increase in wildfire frequency, size, and severity in the western US in the coming decades (Abatzoglou and Williams, 2016). This is a pressing concern because forested watersheds are large contributors of freshwater in the United States (Brown et al., 2008; Daneshi et al., 2020). Wildfire can rapidly reshape the landscape by increasing the potential for erosion and lowering the rainfall thresholds for

intense flooding in the months and years following the fire (Moody and Martin, 2009). A lasting impact that can result from the ecosystem damage caused by wildfire is an increase in sedimentation rates to instream networks and downstream infrastructure (Moody and Martin, 2004; Hohner et al., 2016). Sediment accumulation in downstream reservoirs is of major concern in the western US due to the threat of reduced storage capacity and degraded water quality for dependent communities (Murphy et al., 2018). To predict and respond proactively to post-wildfire risks, many federal agencies rely on empirical models to better understand the potential fire-induced responses in watersheds.

A potentially catastrophic, and yet common, fire-induced response in forested watersheds is the generation of debris flows. Existing post-wildfire hazard assessment models typically focus on predicting the probability of occurrence (Staley et al., 2017), initial sediment volume (Gartner et al., 2008; Gartner et al., 2014; Wall et al., 2023) and grain size distribution of debris flows (Wall et al., 2023) emerging from burned tributary catchments. In addition, recent research has investigated the initial delivery and spatial distribution of post-wildfire sediment in river networks (e.g., Murphy et al., 2019; Brogan et al., 2019; Nyman et al., 2020). However, many models used in post-wildfire planning and mitigation end at predicting debris flow generation, volume, and initial delivery into a river; no existing model has constrained the temporal scale over which debris flow deposits contribute sediment to river networks in the years or decades following a wildfire.

To predict and plan for the cascade of hydrologic, geomorphic, and ecologic dynamics that occur within a watershed after a wildfire, Murphy et al. 2019 developed a framework that links models of post-fire debris flow probability, volumetric yield, initial

sediment delivery into an axial river, and network routing at the watershed scale. This model relies on empirical relationships from Rickenmann (1999) to estimate the runout length of a debris flow deposit based on the deposit's initial volume. Runout length, that is the length of the deposit from its apex to its toe (Figure 1), ultimately depends upon debris flow's sediment volume, flow velocity, and peak discharge (Figure 1; Murphy et al., 2019; Benda and Dunne, 1997; Giles et al., 2016). A notable limitation of the delivery model presented by Murphy et al. (2019) is that it only estimates the initial delivery of debris flow sediment to a river network and does not provide a means to estimate long-term delivery. Although not all post-wildfire debris flows are delivered an axial river, many are, and sediment fluxes in burned watersheds have been observed to remain elevated compared to background rates (Kirchner et al., 2001; Riley, 2012). There has not previously been a basis to predict the amount of sediment eroded from a debris flow deposit over time, and this information is lacking in network scale models.

Initial effects from an increased sediment load following wildfire may include negative impacts to aquatic species such as submerged aquatic vegetation, macroinvertebrates, and fish communities. For example, fine sediment increases turbidity in river systems, which in turn can increase water temperature for many dependent fish and aquatic vegetation (Reale et al., 2015; Beakes et al., 2014). Elevated turbidity additionally reduces dissolved oxygen, as many submerged aquatic plants cannot survive with decreased sunlight (Sanders et al., 2022; Reale et al., 2015). Increased turbidity can persist for 5 to 10 years following wildfire, and debris flows deposited in the valley bottom can persist for millennia, supplying coarse- and fine-grained sediment many years after wildfire (Benda and Dunne, 1997; Verkaik et al, 2013; Rhoades et al., 2011; Nyman

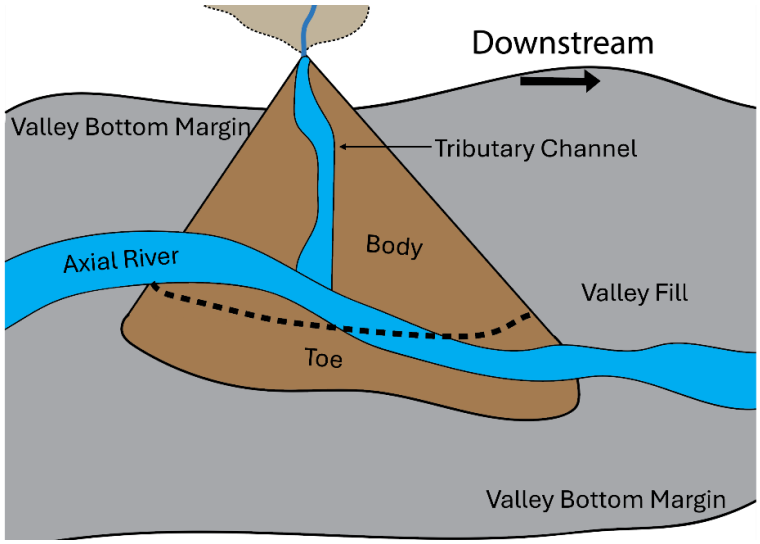

Figure 1. A conceptual plan view illustration of a debris flow fan deposit in an axial valley bottom. Similar to the identified study sites, the debris flow deposit (brown) is initiated from a tributary catchment and deposited in the valley bottom (gray) of the axial river (light blue). In this example, the debris flow runout extends beyond the initial axial river position in the valley bottom, and both the axial river and tributary stream are shown incising through the body of the debris flow deposit.

et al., 2020; Meyer and Pierce, 2003). Rivers more readily transport fine-grained hillslope sediments that are transported as washload or suspended sediment load (Nyman et al., 2020; Reneau et al., 2007). However, post-wildfire debris flows often supply much larger magnitudes, and typically larger grain sizes, of sediment compared with hillslope rilling or sheetwash (Moody and Martin, 2009; Murphy et al., 2019). Conventional sediment routing models (e.g. SWAT, HEC-HMS, HEC-RAS, GeoWEPP) do not consider long-term sediment delivery from post-wildfire debris flows deposited within the valley bottom. Critically, GeoWEPP, a commonly used model to estimate post-fire erosion, only routes sediment from planar hillslopes based off long-term runoff data at small scale watersheds, effectively discounting any sediment sourced via debris flows (Miller et al., 2011; Renschler, 2003).

To date, long-term post-wildfire sediment storage and delivery has yet to be well-documented and thus is not captured by available post-fire geomorphic models. This is compounded by the "messy" nature of post-wildfire sediment; it is often poorly sorted, has the potential to include and deliver large woody debris into channels, and can drastically alter river morphology and connectivity (Nyman et al., 2020; Benda et al., 2003; Rust et al., 2019). Many have attempted to quantify the rate of sedimentation to reservoirs following wildfire, and recently, advanced sediment routing models, such as the Network Sediment Transporter (NST; Pfeiffer et al., 2020; Czuba et al., 2018), have been applied to predict downstream sedimentation impacts after wildfire (Murphy et al., 2019). However, critical limitations still exist for post-wildfire sediment routing, including the lack of constraints on temporal trends of debris flows sediment delivery to river networks, how they influence the river's ability to transport sediment, and the effects large sediment fluxes may have on network connectivity. Thus, it is crucial to quantify the rates of debris flow deposit erosion over time.

Previous studies of alluvial fans deposited in valley bottoms have identified commonalities in erosional patterns, such as fluvial toe-cutting and the development of "feeder streams" on the fan surface (Giles et al., 2016; Leeder and Mack 2001). Observations suggest lateral erosion of alluvial fans by the axial river is driven by both external mechanisms, such as climatic forcing and tectonic tilting, and local geomorphic mechanisms, such as the river's ability to transport sediment (or stream power), which is a function of shear stress, discharge, and channel slope (Giles et al., 2016; Leeder and Mack, 2001; Bagnold, 1966). For example, preferential erosion along the upstream edge of the alluvial deposit may be driven by the angle the axial river intersects the deposit,

while toe cutting may be heavily dependent on sediment supply and transport capacity (Giles et al., 2016; Leeder and Mack, 2001). While many studies have focused on the geomorphic response to large inputs of sediment to fluvial systems, very little research has focused on quantifying erosion rates of sediment deposits in the valley bottom due to the observed erosional processes. Furthermore, improved understanding of fluvial erosion of post wildfire debris flow deposits has implications for the broader geomorphic community; alluvial fans, landslides, fluvial terraces, and glacial deposits are similar examples of potential large sediment sources that may be eroded by rivers in processes and rates similar to those explored here.

Research Objectives and Hypotheses

To understand the temporal scale of sediment contribution from post-wildfire debris flow deposits, two research questions must be addressed:

1) How does the erosion of post-wildfire debris flow deposits and delivery of sediment to higher order rivers change over time?
2) Which local, reach-scale hydrogeomorphic features influence the relative magnitude of debris flow sediment delivery over time?

To address these knowledge gaps, we developed a comprehensive dataset quantifying changes in the volume of post-wildfire debris flow deposits after deposition. The data in this study was obtained with a combination of fieldwork to obtain high resolution data of identified debris flow deposits at present day and remote sensing techniques, such as analysis in ArcGIS and aerial imagery, to measure changes over time. We first identified locations in historical imagery where debris flows had been generated in burned tributary catchments, were deposited within a valley bottom, and had the

potential to interact with axial rivers (Figure 1). For post-wildfire debris flow deposits that were initially delivered to the axial river, we evaluated the effects of channel confinement, local stream power, and other relevant morphometrics that may inform relative magnitude of debris flow sediment delivery over time. We hypothesized:

1) Annual rates of post-wildfire debris flow deposit erosion will decay exponentially over time.
2) The rate of sediment delivery is controlled by valley bottom morphology, debris flow deposit volume, and sedimentological characteristics.

STUDY AREA

All study sites identified for this study were within the state of Utah. Like many western U.S. states, Utah's historical fire management practices consisted mainly of fire suppression (Westerling et al., 2006). Many of the large historical fires were from a time before western settlers arrived in Utah (Choate, 1965; Wagtendonk, 2007). Historical fire suppression in the state of Utah promoted the growth of less fire-resistant tree stands and artificially high fuel loads (Choate, 1965; Halofsky et al., 2018). Unnaturally high fuel loads promote higher severity wildfire and in turn, potentially large sediment fluxes into Utah's watersheds. Increased sedimentation of Utah's river systems has resulted in concern over the state's infrastructure, especially freshwater reservoirs, bridges, roads, culverts, and urbanized areas (UDWR, 2010). Furthermore, as the population in the state of Utah continues to grow, many communities are expanding into the Wildland Urban Interface (WUI) and more infrastructure is moving into fire-prone land (Halofsky et al., 2018; Radeloff et al., 2018).

Most of the freshwater supply in Utah is sourced from precipitation in the form of snowpack in forested watersheds, which account for over 25% of the state's landcover (UDWR, 2021; Choate, 1965). Additionally, Utah consistently ranks as the second driest state in the United States, receiving an average of 13 inches of precipitation a year (UDWR, 2021). Under all projected climate scenarios, Utah snow accumulation is projected to decrease, and snowmelt is expected earlier in the year, imposing further stress on Utah's water security (Khatri & Strong, 2020; EPA 2016). Despite the projected population growth (UDWR, 2021), projected water deficit (Khatri & Strong, 2020; EPA, 2016), and projected increase in wildfire frequency and severity (Abatzoglou et al., 2021; Westerling et al., 2006), the state of Utah has yet to address its reservoir vulnerability to excessive sedimentation resulting from wildfire beyond background sedimentation rates (UDWR, 2021). The conditions from historical wildfire management coupled with risky development patterns and projected water scarcity in Utah underscores the growing need to understand the hydrologic and geomorphic risks wildfire poses to the state's infrastructure.

Study Sites

Potential study sites (i.e., post-fire debris flow deposits) were all initially identified from aerial imagery. Criteria for site identification via aerial imagery included: the debris flow deposit was located within a mapped wildfire perimeter, the debris flow deposit extent was clear and unambiguous with minimal vegetation or shade, satellite imagery was available at ≤ 1-meter spatial resolution, the debris flow had been deposited within a valley bottom as opposed to within a tributary catchment, and the debris flow deposit was deposited adjacent to an axial river (Figure 1). Additionally, because one of

the primary goals of this research was to identify changes to debris flow sediment delivered over time, study sites were required to have at least three dates of imagery, including the initial imagery showing deposition.

The identified debris flow deposits for this study were within seven wildfire perimeters across the state of Utah. Using data sourced from the Monitoring Trends in Burn Severity (MTBS) website (Eidenshink et al., 2007), seven burn perimeters within the state of Utah were identified for this study (Figure 2a). The oldest fire included in this study was the 2010 Twitchell Canyon Fire, and the youngest fires were the Dollar Ridge, Pole Creek, and Trail Mountain Fires, which all ignited in 2018. The lowest elevation site was 1874 meters above sea level (masl), and the highest elevation was 2982 masl. Most of the debris flow deposits intersected a perennial stream, except in the Clay Springs Fire, where debris flows occurred within an intermittent watershed (Table 1). Within the seven

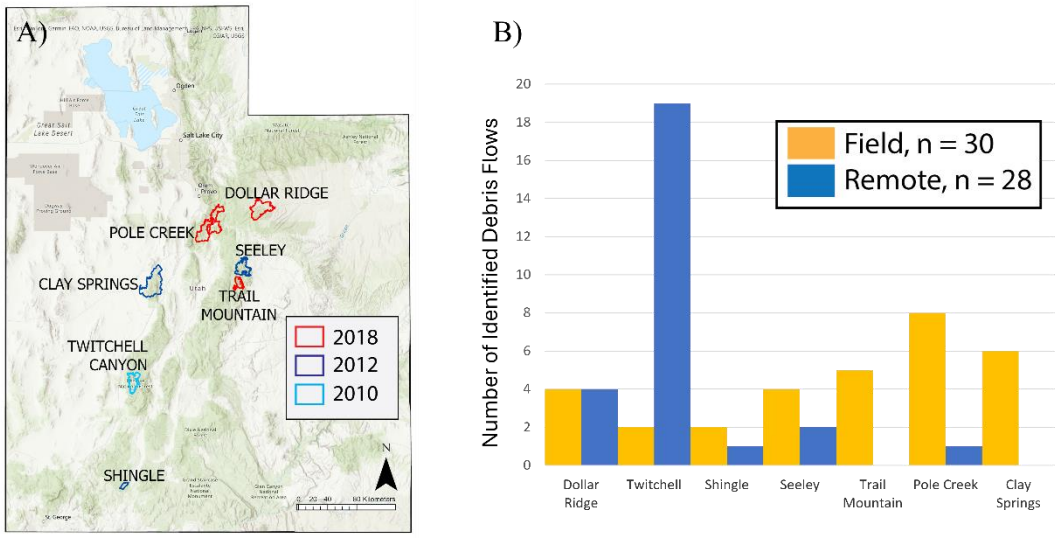

Figure 2. A) Perimeters of wildfires within the state of Utah that were attributed to the debris flow deposits included in this study. The polygon color indicates the year of ignition, denoted in the legend. B) Total count of all the identified sites for this study by each fire. Gold represents sites surveyed in the field and navy blue represents sites documented by remote analysis only.

Table 1. Fire and watershed statistics in this study. NHD = National Hydrography Dataset (USGS, 2019), I = Intermittent, P = Perennial, MAP = 30-yr mean annual precipitation, Ro = Annual Runoff, MAT = 30-yr mean annual temperature, sourced from StreamCat (Hill et al., 2015). Bmh = percentage of area burned at moderate or high severity, sourced via MTBS.gov (Eidenshink et al., 2007).

Fire			**Watershed**							
Fire, Year	Burn Area (km^2)	Bmh (%)	Name	Area (km^2)	Relief (m)	MAT (°C)	MAP (mm)	Ro (mm)	Mean Elev. (m)	NHD Stream Class.
Clay Springs, 2012	437.6	68	Fool Creek	39.2	1343.6	9.8	495.7	29.0	2231.4	I
			Wild Horse Cyn.	9.0	642.8	8.6	422.8	29.0	2058.0	I
			Little Oak Cyn.	5.4	1091.0	8.6	491.5	29.0	2160.2	I
			Hands crabble Cyn.	2.0	956.1	9.8	491.5	29.0	2326.5	I
Dollar Ridge, 2018	234.3	31	Avintaquin Cyn. *	66.6	1038.0	6.3	528.6	57.8	2458.3	P
			Timber Cyn. *	120.4	1091.8	4.5	574.9	58.0	2617.2	P
Pole Creek, 2018	419.0	24	Lake Fork	121	1303.2	6.5	631.8	245.8	2341.8	P
			Blind Cyn.	553.1	1715.1	7.0	478.3	248.0	1992.8	P
			Spanish Fork	60.0	960.2	7.0	554.8	245.0	2260.0	P
Seeley, 2012	194.5	16	Huntington Creek *	16.4	823.3	3.0	740.2	24.5	2830.7	P
			Left Fork Huntington *	105.0	850.6	3.0	689.6	24.6	2797.5	P
Shingle, 2012	32.6	40	Dairy Cyn	10.8	502.1	6.7	507.7	38.0	2317.7	P
Trail Mountain, 2018	71.6	78	Mill Fork	16.3	1099.2	4.0	684.8	24.0	2717.6	P

Table 1. (cont.)

Twitchell Canyon, 2010	181.6	67	Fish Creek	174.5	1818.8	6.5	790.4	67.4	2734.2	P
			North Fork North Creek	14.7	1408.4	4.9	722.5	30.3	2695.2	P

*Indicates presence of an upstream reservoir

identified burn perimeters, 58 debris flow deposits were identified and analyzed for this study (Fig. 2). Of the 58 total study sites, 30 were surveyed in the field during summer 2023, and the remaining 28 sites could only be analyzed using remote sensing via aerial imagery (Fig. 2b).

The 58 identified sites exhibited a wide range of catchment characteristics, such as slope, wetness index, and soil depth, which have all been identified as controls on the initial grain size distribution of post-fire debris flow deposits (Wall et al., 2023). Additionally, each tributary catchment experienced a range of burn severities, which likely influenced their initial volume (Gartner et al., 2014; Wall et al., 2023). The range in initial debris flow deposit areas for the 58 identified sites was between approximately 400 m^2 to 20,000 m^2. Sites selected for more detailed field surveys were selected primarily based on their accessibility, and in some cases, also the availability of previous field data (Wall et al., 2023; Murphy et al., 2019).

METHODS

To identify factors influencing the temporal scale of post-wildfire debris flow deposit erosion and sediment delivery into river networks, we used a combination of remote sensing, fieldwork, and statistical modelling outlined below. Primary observations

of changes to debris flow deposit area were made via aerial imagery. We measured various metrics remotely in ArcGIS, such as tributary catchment characteristics, valley bottom morphology, and plan view channel change of the axial river. Fieldwork surveys were conducted in the summer of 2023. Surveys made in the field were primarily focused on documenting the debris flow deposit present-day extent, the depth of the deposit, and lastly the grain size distribution of the deposit. Additionally, we surveyed the axial river in the form of cross-section surveys and grain size analysis of the channel bed. Data obtained by 2023 field surveys were additionally used to verify any assumptions in debris flow extent (e.g., areas obscured by shade or vegetation) made via imagery.

Historical Imagery Analysis

Changes in area of debris flow deposits were delineated via imagery sourced by a combination of Google Earth Pro, National Agriculture Imagery Program (NAIP; naip-usdaonline.hub.arcgis.com), and Hexagon imagery obtained from the Utah Remote Reference Center (UGRC; gis.utah.gov). The Hexagon imagery was available in 15-centimeter and 30-centimeter resolution in the years 2018 and 2021, respectively. The availability of repeat imagery varied by site, with the minimum number of images being set at three and the maximum number of images at any site being six (Table 2). The highest resolution images were in 2018 at 15-centimeter resolution in the form of Hexagon tiles. The lowest resolution images were 1-meter from NAIP used only for two sites that initiated in 2016 from the Twitchell Canyon Fire in 2010. Imagery of pre-fire conditions was sourced from Google Earth Pro. Available pre-fire imagery for each site varied in spatial resolution and in some cases was limited by dense vegetation. Analysis regarding pre-fire axial river morphology was limited to sites with clear (e.g. spatial

Table 2. Each fire identified for this study with their imagery sources by year. The cell with the fire abbreviation represents the year of ignition. Red lines between years represent gaps in times omitted for space. In these gaps, there was no available or clear imagery for any sites.

2002	2005	2010	2011	2012	2013	2014	2015	2016	2018	2019	2020	2021	2022
		Tw											
				CS									
				S									
				Sh									
Google Earth									TM				
Hexagon									PC				
NAIP									DR				

Tw = Twichell, CS = Clay Springs, S = Seeley, Sh = Shingle, TM = Trail Mountain, PC = Pole Creek, DR = Dollar Ridge

resolution, shade, vegetation) imagery before the wildfire. The availability of aerial imagery ensured there was always one image before debris flow deposition at each site.

Debris Flow Deposit Delineation

For the first year of imagery after wildfire where a debris flow deposit was observed, the initial deposit was delineated by hand in ArcGIS. The observations made via the first year of imagery set two boundary conditions: the projected initial debris flow extent, which informed the initial volume estimate (V_{int}), and the volume of the debris flow deposit remaining after accounting for the conditionally delivered sediment within the first year of deposition (V_0). Any potential volume difference between V_{int} and V_0 is limited to erosion that occurred in the time between deposition and the first image revealing the deposit. In these cases, we typically observed via imagery that the deposit appeared to have runout into and/or across the axial river; however, the axial river was unimpeded and clear of sediment fill (e.g., Figure 1). Thus, it was assumed the axial river had eroded this channel spanning sediment fill is eroded sometime within the first year.

To maintain consistency in delineating the initial debris flow extents, the deposit apex was always terminated at the valley bottom margin closest to the tributary catchment. If there was visual evidence that a debris flow deposit had runout across the axial river channel, the initial area was estimated by extending a polygon across the channel to include this extent. Initial changes to area were then delineated for the same initial image but represented the visible debris flow sediment, informing estimates for V_0. To ensure consistency in the debris flow deposit polygons between years of imagery, each polygon was copied between years and only reshaped if and where change was evident. If there was clear evidence of a secondary depositional event, resulting in an increase in the polygon area, the time since deposition was restarted at zero. This scenario was evident in only four sites across the total 58 sites. All final delineated debris flow deposit polygons were projected from the imagery coordinate system of WGS 1984 into the UTM projected coordinate system with their area and distances preserved, and then their areas were calculated in ArcGIS.

Field Surveys

Field surveys were conducted at 30 of the 58 sites. Field data collection included the debris flow deposit areal extent and depth in summer 2023 and the deposit surface grain size distribution (GSD). Additionally, we surveyed axial channel cross sections and documented the channel bed GSD. Field data were useful to understand how flow and sedimentological characteristics might influence the relative magnitude of debris flow sediment delivery to axial rivers over time as well as verify the debris flow extents mapped via imagery. There were a total of 12 sites, with at least one site in each wildfire

perimeter, in which we had previous GSD collected from a deposit in either summer 2020 by Wall et al., (2023) or 2017 by Murphy et al., (2019).

Debris Flow Deposit Surveys

Field surveys of the debris flow deposits were conducted using a Real Time Kinematic- (RTK) GPS survey device with centimeter-grade accuracy. At each observation point along the deposit perimeter, on the deposit surface, and on the identified pre-debris flow surface (*explained in more detail below*), we recorded a GPS coordinate along with a corresponding descriptive ID. After field surveys were complete, the RTK-GPS data was uploaded to the Online Positioning User Service (OPUS) to ensure maximum accuracy of the survey data. In cases where it was unfeasible to hike RTK-GPS survey equipment to field sites, the areal extent of the debris flow deposit was documented using a handheld GPS and mapped in ArcMap.

The polygons of debris flow deposit areas initially delineated via aerial imagery were used to help inform field mapping. In the field, the perimeters of the debris flow deposits were identified based on lateral transitions observed in material and grain size characteristics of the deposit versus underlying soil or sediment, as well transitions in vegetation between the debris flow surface (where vegetation was either absent, less dense, or more recently established) and the more established vegetation on hillslopes or soil surfaces (Figure 3). In cases where post-fire debris flow sediment was interpreted to be deposited on top of a historical, pre-fire alluvial fan surface, the most recent post-wildfire deposit was distinguished from older deposits based on the relative degree of visible surficial weathering (e.g., desert varnish) and/or the presence/absence of lichen

(Figure 3). If any recent debris flow sediment was observed on the distal side of the axial river, it was also surveyed. In cases where the debris flow deposit appeared to have

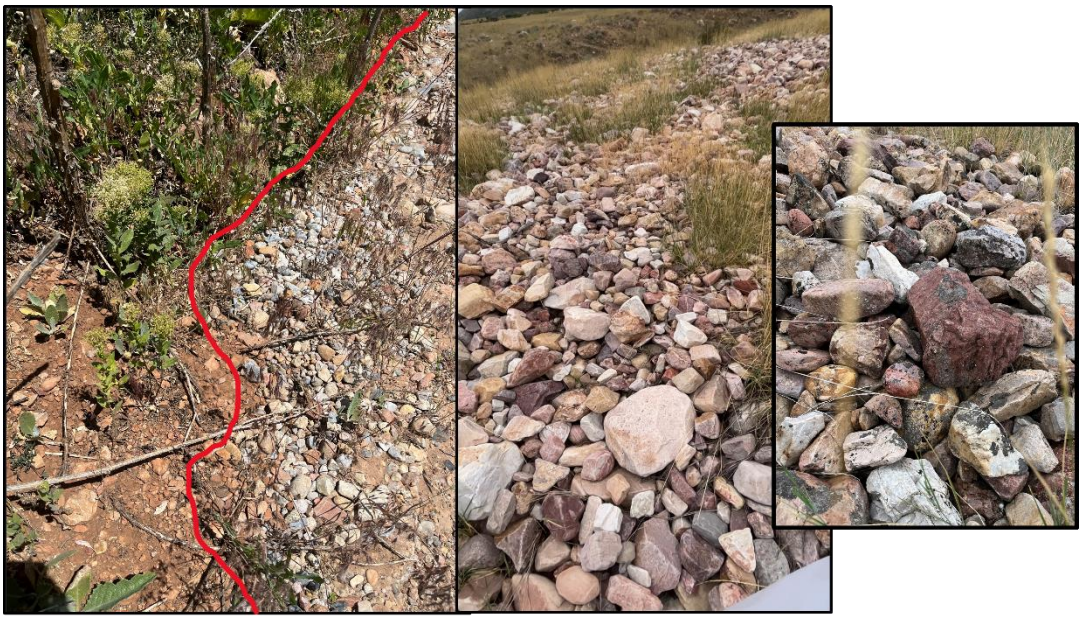

Figure 3. Field images showing the interpreted boundary of debris flow deposit extents. The left most image shows the perimeter of a debris flow deposit (in red) at a boundary with vegetation and hillslope sediment. The image to the right shows fresh debris flow sediment and the inset image shows characteristics of physical weathering in deposits interpreted to be from historic debris flow events.

reached and delivered sediment to the axial river at time of occurrence, the active channel was not included in the surveyed deposit extent.

After surveying the areal extent of each debris flow deposit, we identified and additionally surveyed both the pre- and post-debris flow surfaces to provide estimates of the approximate depth of each deposit. The post-debris flow surface was defined as the surface of the present-day debris flow deposit, and the pre-debris flow surface was any surface interpreted as present before deposition. The pre-debris flow surfaces within the deposit extent were identified where tributary channels had incised into the deposit or where the axial river had cut into the deposit and exposed the boundary with the present-

day debris flow deposit. In locations where the debris flow deposit was not exposed via eroded surfaces, we dug pits into the body of the debris flow deposit to locate and survey the elevations of the pre-debris flow surface. A minimum number of depth measurements was collected at each site based on the deposit area, with at least one depth measurement for every 1,000 square meters (e.g. a 5000 m^2 deposit had ≥ 5 depth measurements), resulting in depth measurements ranging from n = 5 to 40 per deposit across our sites. Locations of depth measurements varied between sites, but in general, the intention was to survey near the apex of the deposit, near the upstream and downstream extents (with respect to the axial river), at the toe, and at locations within the deposit body to ensure the deposit thickness was accurately represented. In cases where we were without the RTK-GPS unit, we manually measured the depth of the debris flow based on a relativized datum (z = 0) based on the pre-deposit surface at each measurement location.

At each location, the boundary between pre-debris flow surface and post-debris flow surface was primarily identified based on changes in sediment size and texture (e.g., a transition from coarse gravel underlaid by fine floodplain sediment or soil, as well as degree of sorting and grading). Previous research has suggested that debris flow deposits can be inversely graded (i.e., coarsen upwards), due to the process of kinetic sieving (Wall et al., 2023; Naylor, M., 1980). This insight proved critical in our identification of the boundaries between the post-debris flow surface from the pre-debris flow surface, especially in cases where there was evidence of multiple stratified debris flow deposits. Specifically, we distinguished the boundary between the most recent deposit from previous deposits by the transition from relatively fine, unsorted sediment to a distinct

layer of coarser sediment, which we interpreted as the upper surface of a previous debris flow deposit.

Lastly, at each field site, we conducted a Wolman pebble count (Wolman, 1954) to estimate the grain size distribution of the debris flow deposit surface. The grain size distribution measured on each debris flow surface consisted of a minimum of 200 observations made during a random walk and measured via gravelometer. The largest grain size class represented was > 250-mm and the smallest class was < 2-mm. Where applicable, we compared surface grain size distributions from field surveys with those previously conducted on the same deposits (Murphy et al., 2019; Wall et al., 2023).

In total, we evaluated 12 sites for changes in their surface grain size distribution (specifically changes to the median grain size, D_{50}) due to the availability of previous documented grain size analysis. These include 10 sites which overlapped with 2020 field surveys conducted by Wall et al., (2023) (Trail Mountain 1, Dollar Ridge 1, 4 and 5, Clay Springs 1 and 2, Seeley 1, Shingle 1, Pole Creek 1, and Lake Fork 1). The two remaining sites in which we could compare previous surface grain size distributions were Fish Creek 5 and 7, within the Twitchell Canyon Fire, that were surveyed in 2017 by Murphy et al., (2019).

Axial Channel Surveys

To understand the influence of the axial river on the erosion of debris flow sediment over time, we additionally collected data on the axial channel over a reach extending 500-meters upstream and 500-meters downstream of the approximate center of the deposit at each of the 30 surveyed deposits. We documented at least one cross-section at the toe of the deposit, one upstream of the deposit, and one downstream of the deposit,

where accessible. At each site, we used the RTK-GPS to measure channel cross-sections and longitudinal bed slope. Between each cross-section, we surveyed the channel thalweg approximately every meter to characterize the bed slope through the deposit reach. In selecting specific cross-section locations, we identified areas that were accessible, safe to wade, and appeared representative of the local reach conditions. For example, we generally avoided surveying cross-sections at knickzones, wood jams, or any other large obstructions that might affect reach geometry. Survey data were uploaded to R, and we used the *splancs* package to calculate the cross-sectional area of the maximum channel depth observed in field surveys (Rowlingson and Diggle, 1993).

At each debris flow in which we surveyed the axial channel, we conducted a Wolman pebble count with a gravelometer consisting of at least 100 measurements in the axial channel bed through the reach intersecting the deposit (no more than 100 meters upstream or downstream of the center of the deposit). The grain size classes were the same as those for the deposit surface grain size data collection. Any sediment measured in the active channel was categorized as channel bed sediment, even if it was interpreted to be sourced from the adjacent debris flow deposit.

Debris Flow Deposit Volume Modeling

Field-based 3D Volume Reconstruction

From the measured elevations of pre- and post- debris flow surfaces, we calculated the field-surveyed volumes and estimated the initial volume of the deposit. To calculate the volumes surveyed in summer 2023, field data points were imported into ArcGIS as XYZ points and used to create Triangular Irregulated Network (TIN) surfaces of the pre- and post-debris flow topography at each site (Figure 4). In cases where

relative depths were measured by hand (at recorded XY coordinates), the pre-debris flow surface was assumed to be a planar surface with a uniform elevation.

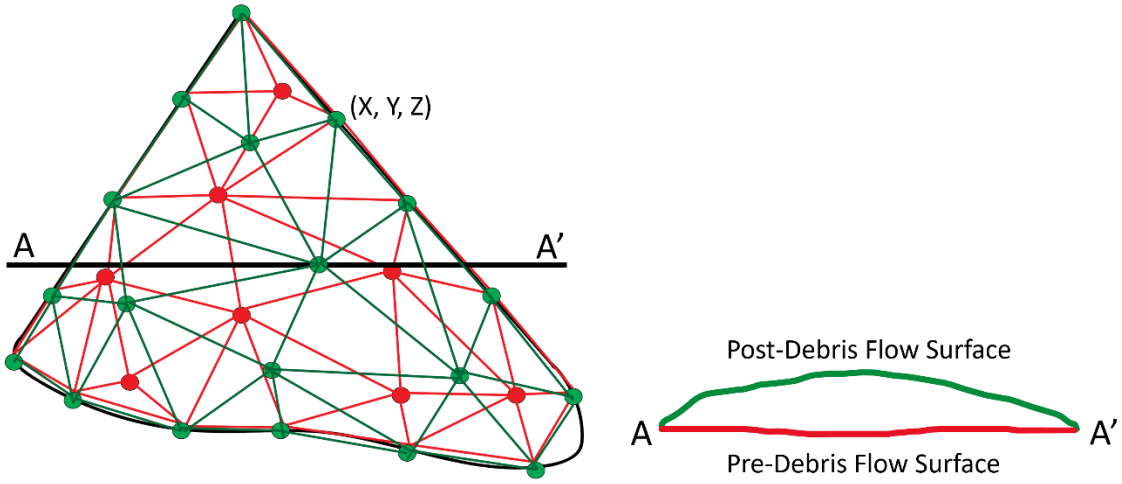

Figure 4. A conceptual figure of a pre- (red) and post-debris flow (green) TIN surface for a deposit. The diagram on the right depicts the cross-sectional transect A to A' shown in the plan view figure of the deposit on the left. The points shown in the plan view TIN surface represent the spatially explicit locations of depth measurements collected from across the deposit.

The pre- and post-debris flow TIN surfaces were both converted to gridded Digital Elevation Models (DEMs) with a 1-meter cell resolution (i.e., smaller than the spacing between depth measurements), and the pre-deposition DEM was subtracted from the post-debris flow DEM to create a spatially explicit map of the deposit thickness. The deposit volumes could then be calculated as the summation of the deposit thickness raster multiplied by the area of each grid cell (here = 1 m^2).

In cases where the debris flow deposit was interpreted to have crossed and filled the axial river at the time of initial deposition, estimates of initial deposit volume were made by interpolating deposit surfaces across the entire mapped extent of the deposit as delineated from historical aerial imagery (Figure 5). The volume of sediment that

potentially filled the axial river (referred to here as “channel fill”) was then approximated based on estimates of pre-deposit channel geometry. Although we field surveyed the channel cross-sections in summer 2023, given the likelihood of post-fire changes in flow and sediment dynamics through the reach following the debris flow input, we did not assume this depth to be representative of its pre-fire condition. Thus, as many of our study sites were ungauged and all lacked pre-deposit channel surveys, we relied on regional curves to estimate the bankfull depth of the pre-fire channel based on the upstream drainage area of the axial river at the depositional reach (Bieger et al., 2015).

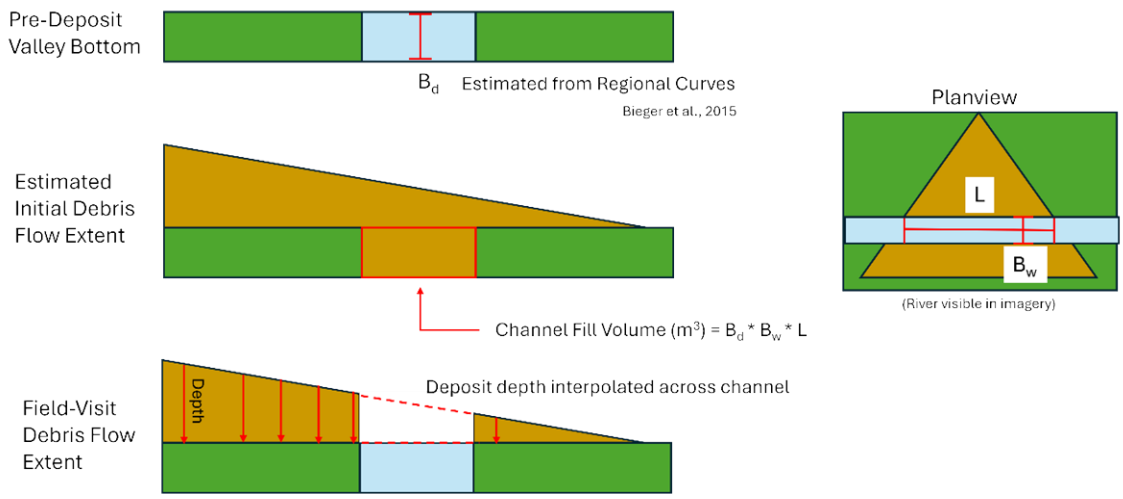

Figure 5. Conceptual diagram illustrating how the initial extent of the debris flow deposit (brown) and channel fill volumes were estimated. Green areas represent the pre-debris flow surface. The bottom panel on the left depicts the interpolated debris flow extent over the axial river where the red lines represent examples of depth measurements throughout the deposit. B_d = estimated channel bankfull depth (based on Bieger et al., 2015), B_w = channel bankfull width, L = channel length measured in plan view from imagery either in pre-fire imagery or in the first image the deposit was observed.

Next, we estimated the length and average pre-fire axial channel width through the depositional reach based on measurements from the pre-fire aerial imagery and/or the first available image where the deposit was visible after wildfire (Figure 5). The product

of the estimated pre-fire channel depth, length, and width through the depositional reach was then used as an estimate of the volume of sediment that had filled the channel at time of deposition and subsequently been eroded. At sites where there was no evidence of initial delivery to the axial river, this channel fill volume was assumed to be zero.

There were numerous points of uncertainty and potential error in estimates of channel fill and erosion. First, our estimates of bankfull channel depth from regional curves may not have accurately captured local variability that existed in the channels. Second, our calculations assumed the axial river geometry (and thus channel fill) could be reasonably estimated as a rectangular channel. Third, we assumed deposits filled the axial channel completely, such that the bankfull depth of the channel is equal to the deposit thickness. And finally, with respect to the timing of delivery and erosion, we assumed in all cases that the estimated channel fill sediment was completely eroded within the first year following deposition (from V_{int} to V_0). Although there was no way to confirm the magnitude or timing of our eroded channel fill estimates, we were limited by the available data and suggest that the approach taken can at least provide an estimate of an eroded volume of sediment that would otherwise go unaccounted for and, at least in some cases, may represent a substantial percentage of the total delivered sediment.

Partitioning Eroded Volumes by Observed Processes

Repeat aerial imagery provided us with the ability to observe two distinct processes responsible for eroding debris flow deposits: incision across the body of deposit by tributary channels and erosion of the deposit toe by the axial river. To estimate the volumes removed each year from the visible changes to debris flow area, we delineated polygons representing the area lost at the toe of the deposit and separately for

the area lost from incision into the deposit surface between all available years of imagery. The raster of the debris flow deposit thickness was then clipped by the respective polygons (Figure 6) and multiplied by the cell area to estimate the volume loss at the toe of each debris flow deposit and into the body of the deposit, as applicable.

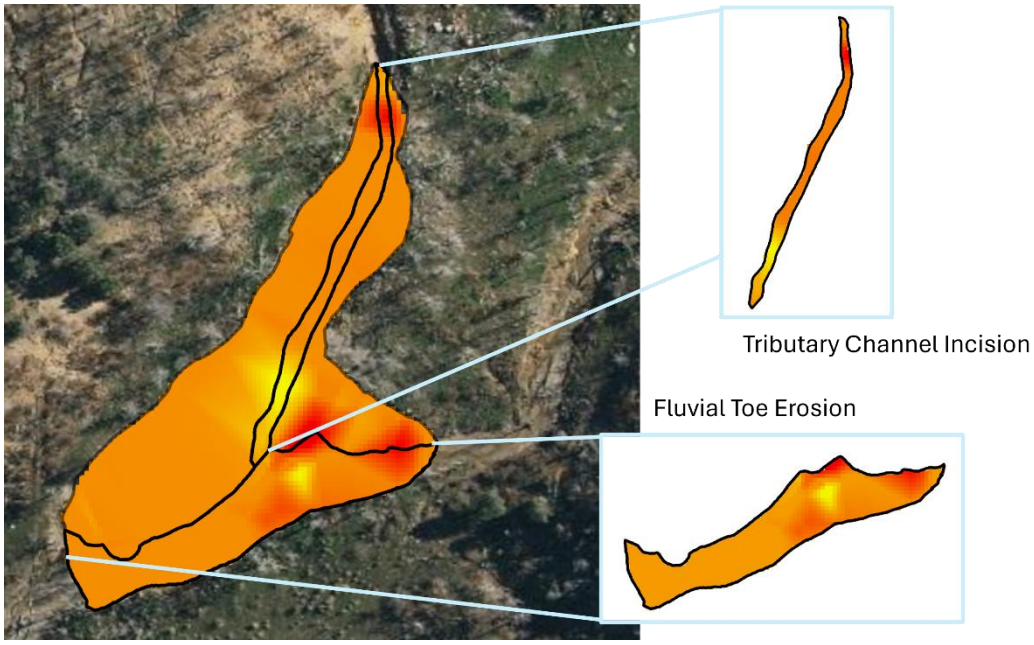

Figure 6. Example of volumetric partitioning by erosional process. The orange raster at left shows the deposit thickness mapped across the entire initial deposit extent, with thickness increasing from yellow to orange to red. The delineated areas in the insets to the right are examples of areas delineated and clipped to calculate the volume of eroded volume from a given image.

This technique was repeated for each year of available imagery for our field sites, editing the area of loss due to each erosional process in each image. We ensured polygons for the two erosional processes did not overlap to avoid double-counting erosion. For years in which there was no visible evidence of erosion, the volume loss was calculated as zero for the two processes. In years in which there was no available imagery, estimates of volume loss were not calculated – effectively time-averaging the volumetric erosion

rates between available image dates. Ultimately, using this approach we developed an empirical dataset of debris flow deposit loss due to toe erosion or tributary channel incision for every deposit in our study.

Surface Deflation

Field observations provided evidence of a likely third erosional process occurring over the debris flow deposits, referred to herein as "surface deflation". Surface deflation refers to the loss of material due to sheetwash or rilling across the debris flow deposit surface, which could preferentially remove fines and erode the deposit surface without any apparent loss of area in plan view. After delineating and calculating the volumes lost to toe erosion or tributary channel incision over time, the remaining uneroded deposit area in each image was used to estimate a potential volume loss to surface deflation. We assumed that surface deflation would occur every year, and without any constraints to suggest otherwise, applied a constant rate to estimate its potential contribution to erosion independent of changes in area or the other two mapped processes. Additionally, in calculating volumetric loss due to surface deflation, we assumed the area of the debris flow deposit remained unchanged between years of available imagery.

Without constraints on potential surface deflation rates, we applied reasonable estimates for a lower and upper bound based on erosion rates from published literature. The selected upper bound was 5 mm per square meter per year, and the selected lower bound was 0.1 mm per square meter per year. Hillslope soil erosion rates following wildfire have been documented with rates ranging from 0.1 to 0.6 mm m^{-2} yr^{-1} for prescribed fires and up to 2 to 12 mm m^{-2} yr^{-1} in high severity fires (Robichaud, 2000; Robichaud and Waldrop, 1994). It is important to note these rates apply specifically to

erosion of fine-grained soil material from hillslopes, while post-wildfire debris flow sediment is coarse, poorly sorted, and unlikely to exhibit hydrophobicity as is typical in post-fire soils (DiBase and Lamb, 2019; Nyman et al., 2020). Therefore, we decided to limit our upper bound to 5 mm m^{-2} yr^{-1} and expect this would still likely represent an extreme case for a debris flow deposit.

Given the field evidence for surface deflation, our estimates of initial deposit volume (V_{int}) needed to include any volume potentially lost due to this process. Therefore, we added the estimated total volume eroded by surface deflation (for both the lower and upper bound) to our estimates of the initial deposit volume at all 58 sites. In cases without any evidence of other erosional processes (i.e., no changes in area), these estimated surface deflation volumes represented the only erosion. Further, not including any estimate for this process could result in underestimated initial volumes for all of our study sites. As a result of using a bounded range of estimated rates for surface deflation, all initial volume estimates are presented with a range; however, the minimum estimated represents the case in which there is no surface deflation (Table 4).

Imagery-based Area-Volume Regression Analysis

To evaluate volumetric change at the 28 sites that were not surveyed in the field, we first used the data from the 30 field sites to determine the relationship between the deposit areas and 3D-reconstructed volumes as measured in the 2023 field surveys. Prior research has indicated there is a power-law relationship between deposit area and volume (e.g., Iverson, 1997; Murphy et al., 2019; Wall et al., 2023) described by Equation 1:

$$V = A^b \quad \text{Eq. 1}$$

Where V represents the deposit volume (m^3), A represents the deposit area (m^2), and *b* is the best-fit exponent. To fit a value for *b,* we first log-transformed Equation 1 to allow for linear regression:

$$log_{10}V = b(log_{10}A) \quad \text{Eq. 2}$$

No additional fitting coefficients were included in the regression (i.e., an intercept of a linear fit) to force the relationship through the origin, such that volumes equal zero when there is no measurable area. However, it is important to note that forcing the intercept through zero results in an artificially inflated R^2, because the R^2 is calculated by comparing the input model to an intercept-only model. The intercept-only model, also known as the null model, tests the null hypothesis that the dependent variable, y, is a function only of the intercept (i.e., it fits better without any predictor variables). When the intercept is removed from the regression, the null model inherently performs worse relative to the input model, and the result is an inflated R^2 that is not representative of the true goodness of fit (McFadden, D. 1974; Grob, J., 2003; Weisberg, S., 2005). Thus, for our regression, we rely on the cross-validated R^2 and the cross-validated the root mean standard error (RSME) to evaluate the performance of the log-transformed area-volume model.

In addition to evaluating this relationship based on the deposit volumes measured during 2023 surveys, we evaluated the relationship between the projected areas of initial deposits (e.g., interpolated across axial channels) and the respective estimates of initial deposit volumes (e.g., including estimates of eroded channel fill and surface deflation). Accordingly, we conducted these regressions using the initial volumes estimated under both surface deflation rates.

Lastly, because our identified sites were cases where a debris flow enters a relatively low slope valley bottom (and thus deposits laterally, much like an alluvial fan; Figure 1), the toe and body of a debris flow deposit can exhibit differences in thickness (Bull, 1977; Blair and McPherson, 2009; Murphy et al., 2019). This observation indicates in order to most accurately estimate volume loss at the toe to the axial river, the best-fit value for *b* should reflect variable thickness throughout the deposit. Therefore, to best estimate volume loss by the identified erosional processes at the 28 remote sites, partitioned volumes were regressed against the partitioned areas at the toe and throughout the body of the deposit (Figure 6). Consequently, regressing the partitioned 3D-reconstructed volumes against the partitioned areas each time step (Figure 6) was crucial to accurately constrain the magnitude of toe erosion by the axial river or tributary channel incision via aerial imagery for the 28 remotely mapped sites.

Error Estimation for Deposit Volumes

The 2023 field survey data of deposit areal extents and corresponding volumes derived from measured deposit thickness represent our highest certainty data available for evaluating the area-volume relationship of deposits. Potential uncertainty in the field data would primarily result from errors in accurately identifying either the deposit perimeter or the contact between the pre-debris flow surface and the deposit. Our field method of documenting the perimeter and thickness in the field has previously been estimated to result in errors of approximately -25% to +30% in deposit volumes (Santi, 2014). The largest sources of error arise from inaccurate estimates of the deposit thickness, especially in cases where present-day debris flows are deposited on historical alluvial fans. While we cannot ensure deposit thicknesses were accurately measured without error, evaluation

of previous imagery for evidence of multiple depositional events and the use of digital maps for reference in the field that showed the extents of deposits as delineated from imagery prior to our field visits helped improve our confidence in the mapping of deposits. Lastly, while RTK-GPS devices are extremely accurate when used correctly, in cases where there was poor satellite visibility or communication between the rover and the base station, we recorded deposit depths by hand to avoid any errors in elevation estimates arising from poor GPS signal. This was a crucial step, as inaccurate estimates of depth propagate into larger errors in volume estimates than inaccuracies in perimeter boundaries (Santi, 2014). This secondary method of recording depths in locations with poor GPS signal proved useful in comparing the average hand-measured thickness against the reconstructed thickness via TINs in ArcGIS in cases of low confidence in the RTK-GPS measured elevations.

To evaluate the degree of error potentially introduced by estimating deposit volumes based on areal extent, specifically with the 28 remotely mapped sites, we compared the volumes predicted by our area-volume regression model against the TIN-modeled volumes (derived from field measured depths) for our 30 field sites. Error estimates were made by comparing the normalized residuals between the 2023 surveyed deposit volume against the estimate from the linear regression model (Eq. 2). Additionally, initial deposit volume estimates for all 30 field sites were evaluated against estimates from published post-fire debris flow volume models (Gartner et al., 2014; Wall et al., 2023). This approach provided one additional reference to assess our initial volume estimates against what might be expected based on these existing empirical models.

Local Morphometrics

Local morphometrics measured for this study focused on the axial river valley bottom and plan view channel and included, but was not limited to, channel confinement, lateral migration distances of the axial river, and the confluence angle (defined as the internal, upstream angle between the debris flow generating tributary and the axial river at their confluence). We also evaluated the influence of the relative lateral position of the pre-deposition axial river in the valley bottom on initial delivery into the river network. Additionally, we evaluated the morphology of the initial deposit, including the deposit splay angle and the projected runout length. Elevation data used to delineate valley bottom margins was sourced from 10-meter Digital Elevation Models (DEMs) retrieved from The National Map (USGS, 2019) for each burn perimeter.

Valley Bottom and Planview Channel Morphology

Using 10-meter DEMs, the valley bottoms were hand-delineated at each site by observing breaks in slope using the Exploratory Analysis tool in ArcGIS. At each site, the valley bottom was delineated 500 meters upstream and downstream from the center of the debris flow deposit. Additionally, channel polygons were delineated by hand over same the 1-km reach using: pre-fire imagery if available, imagery at the time of deposition, and with 2021 imagery which was available at every site in high resolution (30-cm) Hexagon Imagery. To identify and map channel widths, bankfull indicators were identified via imagery, and in many cases, these were observations of point bars and cutbanks outside of the visible water surface at the time of imagery (Harrelson et al., 1994; Figure 7).

Figure 7. Screenshot of a bankfull indicators (point bars and vegetation) in a post-debris flow channel segment. The dashed line and light blue fill represent the visible water surface, and the solid line represents the approximate bankfull width.

A primary variable assessed for this study was channel confinement, which quantifies the available space within the adjacent floodplain for the channel to laterally meander in response to large fluxes of sediment (Benda et al., 2007). After delineating both the valley bottom and channels for each site, their widths were approximated using the Fluvial Link Average Width tool – part of the USUAL Watershed Tools (David et al., 2023). We estimated channel confinement as the ratio of the reach-averaged channel width to the reach-averaged valley bottom width (Benda et al., 2007). In addition to channel confinement, other variables were extracted to describe changes in channel planform geometry from pre-fire to post-fire, including channel width change, the confluence angle, change in channel sinuosity, and any lateral channel migration

following debris flow deposition. The confluence angle was measured manually in ArcGIS, and the channel sinuosity was calculated as the ratio of along-channel length to the straight-line valley length as measured in ArcGIS (Leopold et al., 2000).

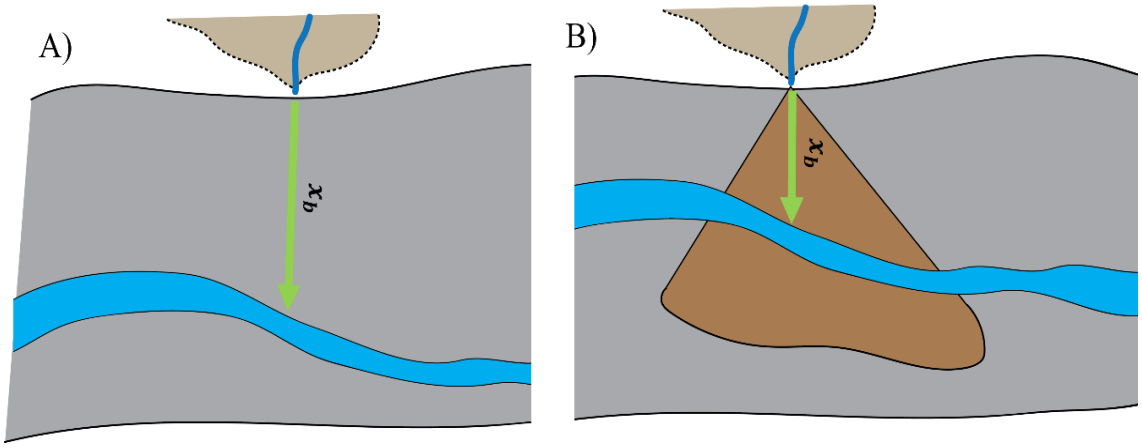

Figure 8. A schematic of the channel distance from the contributing margin, x_b. A) represents the channel location pre-fire, while B) represents the channel location after debris flow deposition, in this case, moving in a negative direction closer to the contributing margin (i.e., a decrease in x_b length).

Lateral migration of the channel was calculated as the difference between the pre-fire versus post-fire orthogonal distance from the intersection of the tributary and valley bottom margin to the closest bank of the axial river, a length defined here as x_b (Figure 8). In addition to evaluating x_b for its importance in predicting debris flow delivery to the axial river at the time of initial deposition, the lateral migration ($\Delta x_b = x_{b,pre} - x_{b,post}$) was also categorized based on the magnitude and direction of movement. First, with respect to interpreting directionality, any sites where the axial river laterally migrated closer to the valley margin and into the deposit body, Δx_b produces a negative value, and sites where the axial river shifted toward the distal valley margin (e.g., impinged against the far valley wall), Δx_b is produces a positive value. Recognizing that background variations in channel migration (i.e., unrelated to post-fire sediment dynamics) may occur, we

categorized any sites that moved less than or equal to 10% of the local valley bottom width as exhibiting minimal migration.

Debris Flow Deposit Runout Length

To evaluate if the location of the debris flow deposition within the valley bottom and relative to the axial river had an influence on volume loss over time, we estimated the runout length of each debris flow deposit. The runout length of debris flows can be defined as the distance from the apex of the deposit (where sediment has entered a valley bottom) to the toe of the deposit where deposition no longer occurs or is significantly reduced (Figure 9). Lab experiments and empirical data describe the runout length as a complex relationship between deposit volume, peak discharge, flow velocity, and deposit rheology (Rickenmann, 1999; Iverson, 1997). Recent flume studies have confirmed many of these relationships and their influence on debris flow runout length; for example, larger deposit volumes, increased flow velocities, and increased water fractions correlate with increased runout length in natural debris flows (de Haas et al., 2015).

Ultimately, the runout length of a debris flow will influence the area of a deposit and its potential for interaction with the axial river (Murphy et al., 2019). The runout lengths were measured using the initial imagery available for each deposit, ideally before it was eroded by the axial river. However, when measuring runout lengths, the deposit had often already been eroded. Additionally, in the case of valley spanning debris flows, sediment deposits would often reach the distal valley margin and be redistributed down-valley. Therefore, measuring the runout length, as defined above, for a debris flow with an unobstructed runout path was often unclear. Consequently, if a deposit had crossed the axial river and been eroded, we would estimate a “projected” runout length based on its

presumed potential extent if uneroded. Additionally, in cases of valley spanning deposits with down-valley redistribution of sediment, we would visually assess the area of sediment redistributed down-valley and estimate a projected potential runout length for the debris flow, assuming it had been allowed to runout unobstructed (Murphy et al., 2019; Rickenmann, 1999; Figure 9).

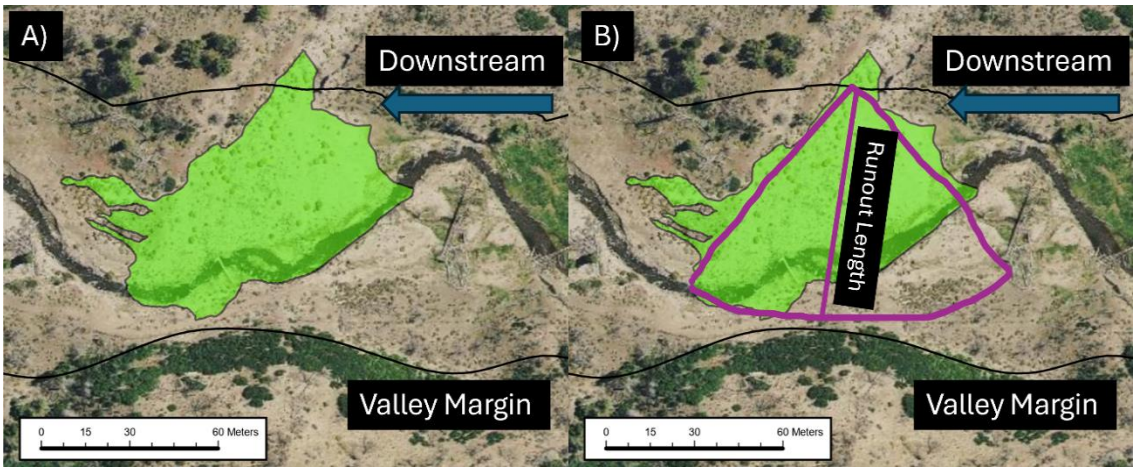

Figure 9. A) Example of the initial delineated debris flow deposit polygon within the valley bottom. B) Example of the assumed geometry (outlined in purple) for an unobstructed fan deposit and its projected runout length, R.

Although this approach involved some subjective user judgment, it allowed us to more representatively relate our measured runout lengths, R, to previously established empirical relationships based on field and flume data.

Watershed Metrics

To evaluate the possible influence of watershed metrics on the relative magnitude of erosion of debris flow deposits, we extracted a suite of variables from within each burn perimeter (Table 1). First, we delineated the watershed, tributary sub-catchments, and river network using a 10-meter DEM and the USUAL Watershed Toolkit in ArcGIS

(David et al., 2023). Tributary sub-catchment characteristics and burn severity metrics were sourced from publicly available data in the StreamCat and MTBS databases (Hill et al., 2015; Eidenshink et al., 2007). Tributary catchment characteristics documented for this study include soil lithology, slope, relief, mean annual temperature, and catchment area. In addition to tributary catchment characteristics, we also extracted local precipitation data, including both the 30-year average annual precipitation from PRISM and the 15-minute rainfall intensities from NOAA PFDS (hdsc.nws.noaa.gov; PRISM.oregonstate.edu).

Regression Analysis

Non-Linear Regression

Non-linear regression models were created using a self-starting algorithm available in the *nls* package in R (Baty et al., 2015). The self-starting algorithm is useful if the initial parameters are not exactly known. To test our hypothesis for question 1 (i.e., that volume loss of a debris flow deposit would fit an exponential decay function), we described the generic relationship as:

$$V_t = 100 - \frac{c}{r}(1 - e^{-rt}) \qquad \text{Eq. 3}$$

Where V_t represents the percentage of initial volume remaining at time *t*, *c* represents the percentage of deposit volume loss within the first year of deposition (V_{int} - V_0), *r* represents a decay coefficient, and *t* represents time in years. For each site, we supplied the self-starting algorithm with the measured value of the initial volume loss, *c*, and let the algorithm fit a value for the decay coefficient, *r.* If the model was unable to

converge, this suggested that rate of the volume loss for that site did not fit this generic exponential decay function.

Simple Linear Regression

Most of the relationships established in this research were modeled with simple linear regression. In some cases, we forced the intercept to zero where we had reasonable evidence to make this assumption. In all evaluated relationships, the raw data was plotted to verify a linear trend existed between the predictor and response variables. In some cases, the relationship was evaluated after log transformation of both the predictor and response variables to ensure the assumptions of linear trends were met. When selecting the best-fit model, we evaluated the R^2 for the linear relationship between models. The R^2 is a measure of how well the variance of the data is described by the model, where a higher value of R^2 indicates a better fitting linear model.

Statistical Analysis

All statistical analyses for the study were performed in R. Many of the datasets were not normally distributed, in which cases they were log-transformed for normality or analyzed with non-parametric statistical tests. Normality was determined by observing the shape of the histogram for the data, evaluating the mean, median, mode and skew of the data, or using the Shapiro-Wilks Normality Test, which tests if the p-value under the null hypothesis is greater than 0.05, in which case there would be evidence to suggest the data are normally distributed (Shapiro and Wilk, 1965).

Statistical tests for significance between binary groups involved a two-sided t-test for normally distributed data and the Wilcoxon Signed Rank Test (Wilcoxon, 1945) for

non-normal data. In cases where groups were non-binary, ANOVA tests were made to establish statistical significance within groups. Covariance between variables was evaluated using correlation plots to avoid multicollinearity when evaluating potential predictor variables. We report summary statistics for various metrics throughout this research. For rate-based metrics, such as percent volume initially lost or decay coefficients, we report the geometric mean over the arithmetic mean. The geometric mean provides a better estimate of the central tendency of smaller datasets when components are not zero and positive.

For evaluations of the exponential decay function and any other non-linear regression analysis, we considered the values of the Akaike Information Criterion (AIC) between various inputs. The AIC is a function of the number of input variables and the maximum likelihood estimate of the model based on the input variables, where a lower value for the AIC suggests a better fitting model. The AIC gives a penalty for added input variables, which helps to avoid overfitting the model (Akaike, 1974). When determining which model fit best, we evaluated the difference in AIC between each model with different input values. The model with the lowest AIC and least number of predictor variables was used to construct the predictive models for this study. To compare the accuracy of a non-linear model against a linear model we used a pseudo R^2 on our predicted results (McFadden, 1974).

Model Validation

Model validation is an important step when constructing predictive models because it helps prevent overfitting. Overfitting occurs when the model can only predict the training dataset and fails to maintain its accuracy when given data outside of the

training data. To avoid overfitting and to validate the accuracy of the models we constructed, we conducted a 5-fold cross validation with 3 repeats on the simple linear regression models in R using the *caret* package (Kuhn, 2008). Because the dataset was relatively small, we did not partition the data into training and test datasets, and instead performed the cross-validation on random subsets of the entire dataset. Cross-validation reports the R^2 of the randomized data, the Root Mean Standard Error (RSME) and provides useful information in validating and understanding how well the constructed models performed at predicting the response variables.

RESULTS

We examined 58 debris flow deposits within seven wildfire perimeters in the state of Utah (Figure 2). Of the 58 study sites, field surveys were conducted at 30 sites in summer 2023 to measure the volume of the deposits, grain size distributions of the deposit surface and axial river channel bed, and the cross-sectional geometry and longitudinal slope of the axial river (Table 3). For each of the 30 field-based volume estimates, we partitioned the volume loss due to different erosional processes. To evaluate changes in volume for the remaining 28 sites we did not survey in the field, we developed a power-law relationship between debris flow deposit volumes and their plan view area. With this dataset, we were able to identify the dominant erosional processes occurring on debris flow deposits, evaluate temporal trends in volume loss of post-wildfire debris flow deposits, determine if erosion of debris flow deposits could be described as an exponential decay function, and investigate the variability in the relative magnitude of volume loss among the 58 study sites.

Table 3. Field metrics collected at each study site within the specified burn perimeter.

Fire, Year (total visited sites)	Volume Estimates	Debris Flow GSD	Channel Bed GSD	Channel Survey*
Clay Springs, 2012 (6)	6	6	4	4
Dollar Ridge, 2018 (4)	4	4	4	4
Pole Creek, 2018 (8)	8	5	4	7
Shingle, 2012 (2)	2	2	2	2
Seeley, 2012 (3)	3	3	4	2
Trail Mountain, 2018 (5)	5	5	4	4
Twitchell Canyon, 2010 (2)	2	2	2	2
Total	**30**	**27**	**24**	**25**

*Counts of channel survey include the number of sites with at least one cross-sectional survey and a longitudinal profile. Refer to Figures D.2 and D.3 in appendices.

The predictive models produced in this study assisted in the development of a conceptual model to describe initial delivery of the debris flow sediment into the axial river, document the dominant erosional processes, and predict the rate of debris flow deposit erosion over time at the decadal scale. We identified a predictive relationship between deposit runout length and axial river position in the valley bottom, x_b (Figure 8), and the resulting initial deposit delivery into the river network. We found that many of the deposits initially delivered to the axial river were dominated by toe erosion, while those deposits that did not reach the axial river were dominated by tributary channel incision or surface deflation. We developed functions that best describe the rate of erosion for sites eroding primarily by toe erosion or surface deflation based on volumetric time-series analysis for all 58 sites.

Debris Flow Deposit Volume Modeling

Field-based 3D Volume Models

Field surveys of debris flow deposit extent and surface elevations were used to estimate the volume of the deposit at the time of 2023 field surveys. Field surveyed volumes ranged from 80 m^3 to 10,000 m^3 with a median of 500 m^3 (n = 30). We used these field data to estimate the volume of debris flow sediment deposited within, or on the other side of, the axial river, as well as any other eroded portions of the deposit that may have been eroded in the time between deposition and the field survey (Figure 10). After accounting for estimates of any potential channel fill volume that had eroded and volume loss by surface deflation, the adjusted initial volume estimates ranged from 110 m^3 to 11,000 m^3 with a median of 520 m^3. Lower reported estimates of the initial debris flow volume assume no surface deflation on the deposit, where the initial volume represents the interpolated deposit volume including channel fill (Figures 10 and 5). Of the 30 field sites, there were a total of six debris flow deposits that did not reach or initially deliver sediment to the axial river (Table 4). For the remaining 24 sites that did initially deliver sediment to the axial river, the volumes that were estimated to have filled the axial river channel (and then be subsequently eroded) contributed to, on average, 9.4 ± 0.5% of the total estimated initial debris flow deposit volume and 51.6 ± 3.3% of the estimated initially eroded volumes ($V_{int} - V_0$) (Table 4).

To assess our initial volume estimates for the post-fire debris flow deposits, we evaluated the initial volume estimates by comparing the field-based initial volume estimates against those predicted by existing post-fire debris flow volume models (Gartner et al., 2014; Wall et al., 2023). Modeled volumes from the Wall et al., (2023)

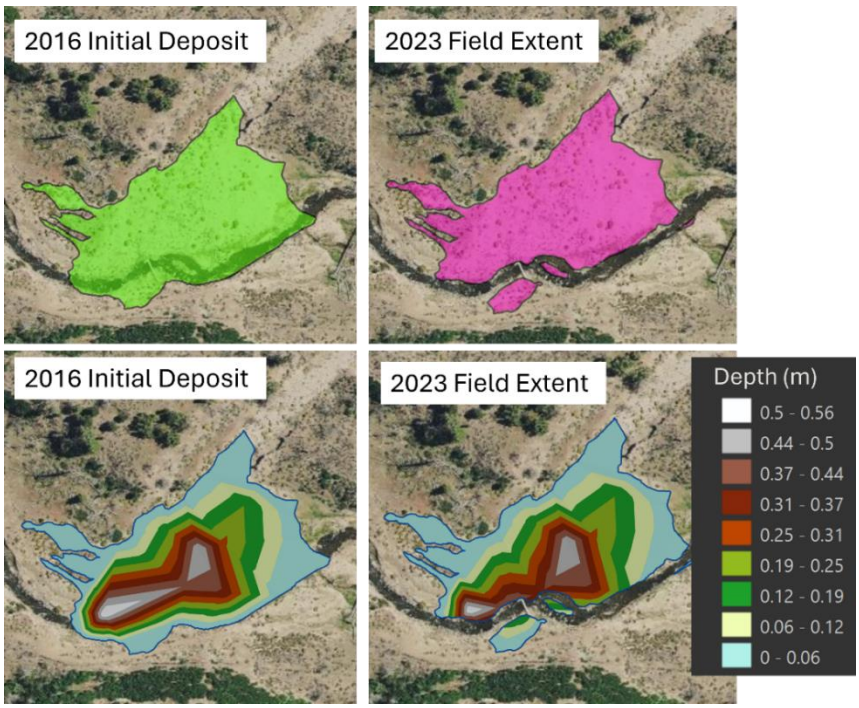

Figure 10. Examples of changes to a debris flow deposit from the initial deposition in 2016 to the field measured extent in 2023. The bottom two panels are the 3D surfaces, in this case representing the relative depth.

model produced a residual standard error of 367.4 and an R^2 of 0.22 for our field-based estimates. The low R^2 with the Wall et al., (2023) model likely resulted from the tendency of the model to underpredict initial volumes greater than ~1000 m^3 (Figure 11). The estimated initial volumes of the 30 field sites compared against the volumes predicted by the Gartner et al., (2014) volume model produced a much larger residual standard error of 9,214 m^3 and a very low R^2 (= 0.002). However, we note that in contrast to the Wall et al., (2023) model, the volumes for the four largest deposits in our study, ranging from 2,000 to 11,000 m^3, were better predicted by the Gartner et al., (2014) model (Figure 11).

While detailed evaluation of these published models was not our intention and beyond the scope of this study, the large residual standard error in the Gartner et al., (2014) model suggests that many of the estimated initial volumes resulting from our 3D-

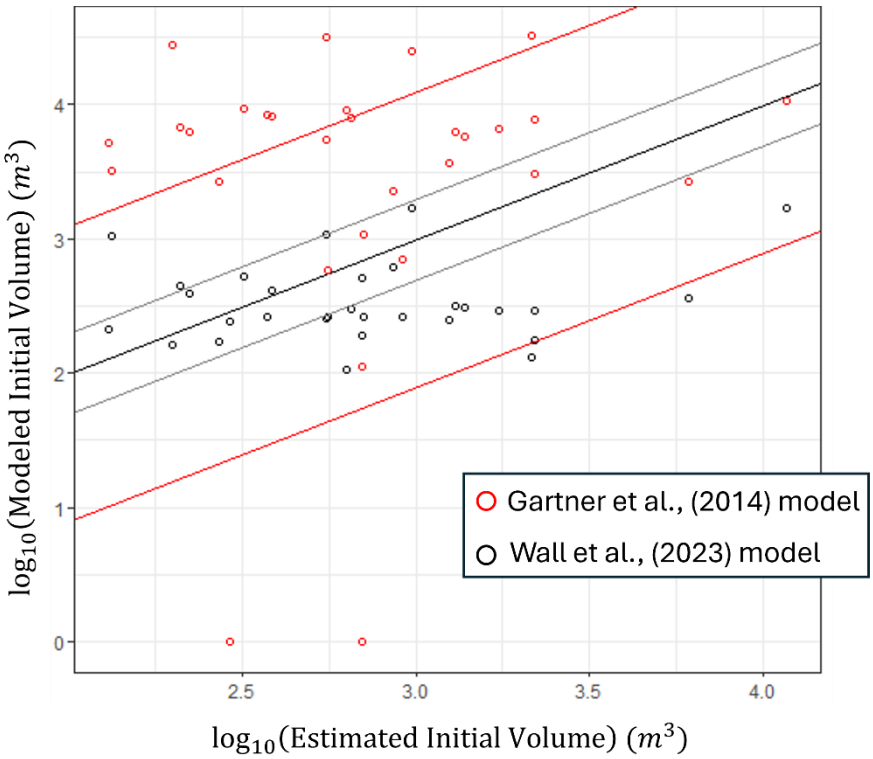

Figure 11. Initial volume estimates from two volume models. The thick black line represents 1:1 agreement where the grey/ red lines are one residual standard error envelope for the corresponding model. Data are plotted in log-log space.

reconstructions are better described by the Wall et al., (2023) model. Additionally, nearly half of the volumes from our field sites (13 of 30) were overpredicted by an order of magnitude with the Gartner et al., (2014) model. Conversely, the Wall et al., (2023) model did not overpredict any volumes by more than an order of magnitude but did underpredict the volumes at three sites by more than an order of magnitude. Additionally, the Gartner et al., (2014) model predicted volumes of zero for two sites due to the natural log expression in the published model, in which case the tributary catchment burned at low severity (Figure 11; Gartner et al., 2014; Gorr et al., 2023).

Table 4. Summary of volumes for the 30 field sites, including the interpolated initial volume, the estimated channel fill volume, estimated volume loss to surface deflation, the total estimated initial volume as the sum of the channel fill volume and volume loss to surface deflation, and the volume measured during field surveys in 2023. All volumes are in m^3.

Site	Interpolated Initial Deposit Volume	Estimated Channel Fill Volume	Estimated Volume loss to Surface Deflation	Estimated Initial Deposit Volume	2023 Measured Volume
CS1	704.8	0.0	5.7 – 284.8	704.8 – 989.6	704.8
CS2	532.6	3.4	2.9 – 143.5	536.0 – 679.5	506.4
CS3	150.3	0.0	1.8 – 89.3	150.3 – 239.6	150.3
CS4	517.9	6.9	1.1 – 54.9	518.6– 579.7	494.7
CS5	602.7	13.4	2.0 – 102.0	616.1 – 718.1	583.5
CS6	109.0	0.0	0.9 – 46.1	109.0 – 155.1	103.0
DR1	519.4	0.0	2.6 – 130.4	519.4 – 649.8	519.4
DR2	166.9	36.7	0.7 – 35.2	203.6 – 238.8	105.7
DR4	1003.5	205.2	1.3 – 65.1	1208.7 – 1273.8	570.6
DR5	1433.0	192.5	5.6 – 279.7	1625.5 – 1905.2	959.8
FC5	1749.2	249.0	5.9 – 295.3	1998.2 – 2293.5	1323.4
FC7	727.8	166.2	3.2 – 160.5	894.0 – 1054.5	597.8
LF1	11542.3	555.8	8.2 – 410.3	12098.1 – 12508.4	10002.7
LF2	5814.4	148.3	6.8 – 341.6	5962.7 – 6304.3	5273.2
PBC1	373.2	60.7	0.5 – 22.8	433.9 – 456.7	126.4
PC2	736.1	142.3	1.3 – 63.1	878.4 – 941.6	400.3
PC3	225.0	44.7	0.8 – 41.9	269.7 – 311.6	217.7
PC4	461.5	64.5	1.2 – 61.5	526.0 – 587.4	278.9
PC5	175.4	28.7	0.2 – 9.0	204.1 – 213.1	112.3
PC6	560.9	103.1	1.2 – 62.4	664.0 – 726.4	360.2
S1	573.6	0.0	3.0 – 148.4	573.6 – 722.0	573.5
S2	210.6	29.9	0.8 – 41.6	240.5 – 282.1	210.8
S3	1121.1	95.4	3.1 – 154.6	1216.5 – 1371.1	748.1
Sh1	1306.5	0.0	3.0 – 149.0	1306.5 – 1455.5	1306.5
Sh2	2146.9	20.1	9.2 – 458.3	2167.0 – 2625.4	1684.0
TM1	2095.6	55.0	1.5 – 73.5	2150.6 – 2224.1	1746.3
TM2	116.0	4.6	0.4 – 18.1	120.6 – 138.6	83.3
TM3	357.2	11.8	0.7 – 33.1	369.0 – 402.1	280.3
TM4	266.1	4.6	0.2 – 10.3	270.7 – 281.0	146.4
TM5	526.2	0.0	0.7 – 34.6	527.5 – 561.6	526.2

Area-Volume Regression

Because there were 28 sites that we could not visit in the field, it was crucial to establish the relationship between deposit volume and area to ensure accurate estimates of volume from remote imagery. We first evaluated the performance of the area-volume linear regression model, described by Eq. 2, with the 2023 field measured data, specifically the total deposit volume against the total deposit area. The log-transformed linear regression of the 2023 field estimated areas versus their volumes performed well with an R^2 of 0.99, a cross-validated R^2 of 0.75, and RSME of 0.28. The best-fit exponent *b* for the power-law function (Eq. 1) regarding the relationship between deposit area and volume in 2023 was 0.81 (Table 5). The mean of the normalized residuals, that is the difference between the measured 2023 volume and modeled 2023 volume, was negligible (-0.03), suggesting the area-volume model performed well on the dataset (n = 30).

To accurately estimate the volume loss after partitioning the deposits into areas lost at the toe and by tributary channel incision through the body (Figure 6), we evaluated the same volume to area relationship on the partitioned polygons. There was a relatively low dataset of field sites with volume loss to tributary channel incision (n = 16), therefore, we assumed the best fit exponent describing volume loss throughout the deposit body in Eq. 1 was $b = 0.81$. This assumption was made on the basis that the deposit body represents a large portion of the deposit total area, and therefore, the exponent that best fit the entire deposit body should similarly apply to these features that tend to cut across the entire deposit (Table 5). The mean of residuals between the measured 2023 tributary channel incised volumes and the modeled tributary channel incision volumes was 0.001, indicating a well-fit model. Residuals at each time step were

very low (< ± 10%), indicating negligible error associated with regressed volumes representing areas lost to tributary channel incision.

We found that the depth of the toe deposit cannot be assumed to be the same as the average depth of the deposit (Figure 1). Specifically, for the 30 field sites, the deposit thickness at the toe was significantly thinner than that of the deposit body (Table 5). The modeled volumes for partitioned polygons at the toe of the deposit were substantially overestimated if we applied the same exponent determined for the entire deposit body (b = 0.81) to their areas (R^2 = 0.51, mean of residuals = -65.9). Therefore, consistent with previous suggestions, the volumes predicted for the toe of the deposit must be evaluated as a separate geometric unit (Murphy et al., 2019) and required a different exponent describing the relationship between volume and area. After regressing the modeled volumes of the partitioned toe polygons against their areas (Figure 6), the best fit value for b to describe the relationship between toe volume and toe area was 0.69 (R^2 = 0.96, cross-validated R^2 = 0.65, RSME = 0.46, and a mean of residuals of -0.06) (Table 5). The area lost at the toe comprised an average of 15% of the total deposit area among the 30 field sites. The average difference between the regressed and 3D reconstructed volumes at the toe of the deposit resulted in an error of ± 10%. The toe volume on average contributed to 12% of the total deposit volume across all 30 field sites, therefore, the ± 10% error in the estimated toe volume with the exponent b = 0.69 represents a small proportion of the total deposit volume.

Lastly, because the initial volume estimates include volume that is ultimately lost via channel fill and surface deflation (and therefore a hypothetically larger deposit thickness at the time of deposition), we evaluated the same relationship on the initial

volume estimates (high, low, and median) against the initial deposit area. We found the best-fit value for *b*, for the high, low, and median initial volume estimate against the initial area to be 0.85. The linear regression using the median initial volume estimates was best-fit with an R^2 of 0.99, a cross-validated R^2 of 0.80, and RSME of 0.21. The mean of normalized residuals for the initial volume estimates was -0.03, indicating a well-performing model.

Measured changes in deposit depth from the time of deposition and partitioned across the deposit were predicted based on their delineated areas using the power-law relationship relating deposit area to volume (Eq. 1). However, applied to the 28 remotely mapped sites, we used variable exponents based on the results above. Specifically, we used an exponent of $b = 0.85$ to estimate the initial deposit volume, an exponent of $b = 0.81$ to estimate volumes lost throughout the body after deposition (i.e., tributary channel incision), and an exponent of $b = 0.69$ to estimate volumes lost at the toe of the deposit (Table 5).

Table 5. Deposit depths and the corresponding value of *b* in Eq. 1 resulting from linear regression of the 30 field sites. The values of *b* were used to estimate volumes for the 28 remotely mapped debris flow deposits and the corresponding locations.

Equation 1:	$V = A^b$		
Deposit Location	**Average Depth (m)**	**Median Depth (m)**	**Value for *b***
Initial Deposit (V_{int})	0.33	0.24	0.85
Deposit Body (V_t, $t \neq Int$)	0.30	0.23	0.81
Deposit Toe	0.23	0.12	0.69

Estimates of Remotely Mapped Deposit Volumes

Evaluation of differences in relative deposit depth, both spatial and temporally, allowed us to identify the relationship between deposit area and deposit volume at the

time of deposition (V_{int}), lost throughout the body by tributary channel incision, and volume loss at the toe by the axial river. The resulting regression-based initial deposit volume estimates ranged from 155 to 3700 m^3 with a median of 922 m^3. There was a total of four sites (of the 28 remotely mapped sites) that did not initially deliver sediment to the axial river, as evident from imagery. For these four sites, we estimated the channel fill volume as zero m^3. Additionally, we estimated the lowest initial volume assuming there was no surface deflation. The estimated channel fill volume for the remaining 24 sites initially delivered to the axial river represented approximately 9 ± 0.5% of the initial deposit volume and 55 ± 5% of the estimated initially delivered volume ($V_{int} - V_0$), similar to the range from our 30 field sites (Table 6).

Estimates of volume loss to toe erosion or tributary channel incision were made on the 28 remotely mapped debris flow deposits with the appropriate value of *b* for the corresponding location of erosion (Table 5). We observed tributary channel incision on seven of the 28 remotely mapped sites, in which case we estimated the volume loss with an exponent $b = 0.81$ in Eq. 1 against the partitioned polygon area at each timestep (Figure 6). The estimated volume of tributary channel incision for the seven sites in which it was identified was between 20 m^3 and 118 m^3, with a median of 51 m^3 and an average of 62 m^3 (Table 8). Toe erosion by the axial river was observed at 24 of the 28 remotely mapped sites and was quantified using the exponent $b = 0.69$ in Eq. 1 against the partitioned areas at each time step (Figure 6; Table 5). The estimated volume loss by toe erosion was between 20 and 295 m^3, with a median of 128 m^3 and an average of 126 m^3 (Table 8).

Table 6. Initial deposit area of the 28 remote debris flow deposits, the estimated initial volume via regression, the estimated channel fill volume, the volume loss to surface deflation, and the total estimated initial volume including the channel fill and surface deflation volume.

Site	Initial Deposit Area (m^2)	Regressed Initial Deposit Volume (m^3)	Estimated Channel Fill Volume (m^3)	Estimated Volume loss to Surface Deflation (m^3)	Estimated Initial Volume (m^3)
DR1A	17614.7	3685.8	373.7	8.1 – 406.6	4059.5 – 4466.2
DR3A	15163.4	3249.9	0.0	7.6 – 379.1	3249.9 – 3629.0
DR4A	9666.1	2226.4	405.3	4.1 – 292.6	2631.7 – 2834.3
DR5A	7267.9	1752.2	87.3	3.2 – 161.4	1839.5 – 2000.9
FC1	5688.5	1426.3	243.4	5.2 – 258.0	1669.3 – 1927.7
FC2	5069.3	1294.7	116.5	4.3 – 214.8	1411.2 – 1626.0
FC3	1613.6	494.9	60.8	1.4 – 71.6	555.8 – 627.3
FC4_11*	2271.1	659.5	79.1	0.7 – 35.5	738.6 – 774.1
FC4_18*	1634.1	500.2	78.3	0.5 – 24.8	578.5 – 603.3
FC5_11*	8337.5	1966.4	464.1	0.6 – 28.7	2044.7 – 2459.2
FC5_14*	7195.7	1737.6	288.4	1.2 – 59.6	2026.0 – 2085.5
FC7_11*	4494.1	1170.1	275.6	1.4 – 70.9	1445.7 – 1516.6
PC7	1424.8	445.8	133.0	0.4 – 18.3	578.7 – 597.1
S4	2087.9	614.5	37.6	1.6 – 77.9	652.1 – 730.1
S5	537.4	196.5	0.0	0.5 – 26.9	196.6 – 223.4
S6	976.6	324.6	32.3	0.5 – 25.2	356.9 – 382.2
SC1A	9919.2	2275.3	75.3	9.8 – 29.5	2350.7 – 2380.1
SC2_11*	406.0	155.3	11.8	0.1 – 4.6	167.1 – 171.8
SC2_14*	701.4	245.8	20.3	0.4 – 17.6	266.1 – 283.8
Sh3	7265.2	1751.7	49.8	4.7 – 236.2	1801.4 – 2037.6
T1	12024.2	2674.5	79.5	8.6 – 430.7	2754.1 – 3184.8
T2	1285.4	408.9	11.9	0.8 – 39.4	420.8 – 460.2
T3	2505.0	716.1	38.0	1.3 – 65.4	754.1 – 819.5
T4	5686.5	1425.8	28.9	4.0 – 201.1	1454.7 – 1655.8
T5	1641.5	502.1	0.0	1.3 – 65.7	502.1 – 567.8
T6	1303.9	413.8	23.6	0.8 – 41.6	437.4 – 479.0
T7	654.4	231.9	16.5	0.3 – 13.7	248.4 – 262.0
T8	3651.2	982.8	0.0	2.9 – 145.6	982.8 – 1128.4

*Site names with an underscore and two digits represent locations with repeat events from the same tributary. The two-digit number represents the year of estimated deposition (e.g. FC4_11 deposited in 2011, and FC4_18 deposited from the same tributary in 2018).

Debris Flow Deposit Erosional Processes

We identified three erosional processes occurring across post-fire debris flow deposits. Observations made by historical imagery provided evidence of two erosional processes resulting in changes to debris flow deposit area, toe erosion and tributary channel incision. We identified 10 of the 58 total sites that were not initially delivered to the axial river, in which case toe erosion due to the axial river was absent over the entire time series. Of the 58 total sites, there was a total of 22 sites in which there was evidence of the development of tributary channels on the deposit surface, independent of whether the deposit was initially delivered to the axial river. Lastly, we identified a third inferred erosional process in the field - surface deflation - which resulted in losses of volume without changes in deposit area.

Toe Erosion and Tributary Channel Incision

Two erosional processes were measurable via changes to the deposit area in time, toe erosion by the axial river and tributary channel incision into the deposit body (Figure 1). Many of the study sites (48 out of 58 total) were observed to erode at the toe of the deposit by the axial river. Estimates of the total volume loss due to toe erosion included estimates of channel fill volume at the time of deposition under the assumption that all channel fill sediment was completely evacuated by the time of field surveys in 2023. We validated this assumption via cross-sectional surveys of the axial channel at 25 of the 30 field sites (Table 3). Of the 25 axial channel cross-sections, 20 were from deposits observed to have initially been delivered to the axial river. The maximum surveyed depth of the axial channels in 2023 were found to be deeper than the estimated pre-fire bankfull channel depths at all 20 sites. While this finding does not confirm our assumption that the

pre-fire channels were completely filled by sediment or completely evacuated within the first year, it does at least help to validate our assumption that *if* the axial channels were completely filled with sediment in cases where debris flows were observed to have runout into and beyond the channel, then this sediment is unlikely remaining in the post-fire channel as of our 2023 field surveys.

Based on this assumption of complete evacuation of channel fill sediment in the first year, we interpret that the volume loss due to toe erosion was highest in the first year of deposition for all sites with initial delivery to the axial river (n = 48). The range of estimated volume loss due to toe erosion (including the evacuated channel fill volume) at all 48 sites was 8 m^3 to 691 m^3, with a median of 196 m^3 and mean of 129 m^3 (Table 7). We additionally evaluated toe erosion within each of seven burn perimeters (Figure 2a; Table 7). This analysis included the absolute volume loss to toe erosion, where the reported uncertainty represents the estimated 10% error in regressed volumes at the toe of the 28 remotely mapped sites (Table 7). The largest average error in this volume was for the Twitchell Canyon Fire, likely because there was a large ratio of remotely mapped sites to field surveyed debris flow deposits (19:2 respectively). The average error in these sites, ± 11.4 m^3, represents less than 5% of the average volume loss at sites within this burn perimeter (Table 7). Similarly, we evaluated the 10% error against the relative volume loss, as the percentage of the initial deposit volume, for all 28 remotely mapped sites within each burn perimeter. The error arising from regressed volume estimates was negligible, representing less than 1% of the initial deposit volumes within each burn perimeter.

Table 7. Summary statistics at sites where toe erosion was present separated by fire. Data represents the amount of volume loss due only to toe erosion by the axial river.

	Absolute Volume (m^3)			Relative Volume (% of V_{int})			
Fire	**Mean**	**Median**	**Range**	**Mean**	**Median**	**Range**	**n**
Clay Springs	49.7 ± 0.0	42.6 ± 0.0	30.1 - 63.9	8.1 ± 0.7	8.3 ± 0.6	4.0 – 11.2	3
Dollar Ridge	371.7 ± 7.3	134.0 ± 6.7	88.8 - 509.1	24.1 ± 1.2	20.0 ± 1.1	2.9 - 25.6	6
Pole Creek	271.0 ± 0.9	96.0 ± 0.0	48.2 - 680.1	27.2 ± 0.9	28.9 ± 1.6	1.0 – 40.5	9
Seeley	223.0 ± 5.8	85.4 ± 0.0	109.6 – 473.7	29.8 ± 1.8	28.0 ± 1.5	11.8 – 31.0	4
Shingle	120.1 ± 5.0	69.5 ± 0.0	89.6 – 150.6	5.8 ± 0.4	5.8 ± 0.4	2.6 - 5.6	2
Trail Mtn.	123.2 ± 0.0	24.6 ± 0.0	7.9 - 435.6	13.5 ± 0.6	11.7 ± 0.2	0.4 – 25.9	4
Twitch.	245.7 ± 11.4	116.8 ± 11.7	15.7 – 690.8	15.1 ± 0.6	23.3 ± 0.9	1.4 – 29.9	20
Total	128.6 ± 12.9	195.8 ±19.6	7.9 – 690.8	13.8 ± 0.2	18.9 ± 4.2	0.4 – 40.5	48

Absolute values are reported with uncertainty due to error in regressed volumes for the remote sites within each burn perimeter. Uncertainty between relative volumes is due to the range of estimated initial deposit volumes, where the median between the high and low estimate is reported. n is the number of sites where toe erosion was present.

Analysis across wildfires indicates that toe erosion can be variable, both temporally and spatially. Two wildfires, the Shingle Fire (2012) and Clay Springs Fire (2012), on average lost less than 10% of the initial deposit volumes from toe erosion, despite their relatively older deposit age within our study. In comparison, sites within the Dollar Ridge Fire (2018), Pole Creek Fire (2018), and Seeley Fire (2012) lost on average > 20% of their initial deposit volumes from toe erosion. Sites within the Seeley Fire lost the greatest amount of volume to toe erosion, representing an average loss of approximately 30% of initial deposit volumes (Table 7).

Unlike toe erosion, tributary channel incision was less common throughout the dataset, as it was observed in only 22 of the 58 total study sites. Tributary channel incision was also responsible for a lower magnitude of erosion with a range of 9 m^3 to 333 m^3, a median of 54 m^3 and a mean of 74 m^3 across all 22 sites (Table 8). Many tributary channels first identified in imagery were generally single threaded, typically

occurred near the center of the debris flow deposit and exhibited very little lateral migration through the debris flow deposit over time. During the 2023 field surveys, we observed tributary channels that were well connected to the axial river at the toe of the deposit, had incised up to a meter deep, and in many cases, had incised below the depth of the debris flow deposit and into the pre-existing valley fill sediments. The only sites in which tributary channel incision was found to be the dominant erosional process were four sites within the Trail Mountain Fire (Figure 2a). These four sites lost a maximum of 33% of their initial volume to tributary channel incision, with a median of 7.5% and mean of 12% (Table 8). Generally, volume loss to tributary channel incision represented on average 6.9 ± 0.5% of the initial deposit volume across all 22 sites in which it was observed to occur. The median of percentage volume loss relative to the initial deposit volume was 5.4 ± 0.3% (Table 8).

Table 8. Summary statistics at sites where tributary channel incision was present separated by fire. Data represents the volume loss due only to tributary channel incision.

	Absolute Volume (m^3)			Relative Volume (% of V_{int})			
Fire	**Mean**	**Median**	**Range**	**Mean**	**Median**	**Range**	**n**
Clay Springs	N/A	N/A	N/A	N/A	N/A	N/A	0
Dollar Ridge	80.8	80.8	44.0 – 117,9	1.4 ± 0.2	8.9 ± 0.5	0.1 – 8.4	2
Pole Creek	91.4	57.1	20.3 – 332.5	5.9 ± 0.1	7.0 ± 0.3	1.0 – 12.6	8
Seeley	70.1	70.1	70.1	1.4 ± 0.1	5.4 ± 0.3	5.1 – 5.7	1
Shingle	142.5	79.7	42.3 – 117.1	5.3 ± 1.2	3.8 ± 1.9	1.6 – 5.7	2
Trail Mtn.	69.7	72.0	9.1 – 125.6	14.8 ± 0.4	10.8 ± 0.5	1.9 – 32.6	4
Twitch.	38.1	1.1	47.9 – 54.0	1.0 ± 0.6	2.3 ± 0.8	0.2 – 12.1	12
Total	74.1	54.4	9.1 – 332.5	6.9 ± 0.5	6.0 ± 0.3	0.1 – 32.6	22

Uncertainty between relative volumes is due to the range of estimated initial deposit volumes, where the median between the high and low estimate is reported. n is the number of sites where tributary channel incision was present.

Surface Deflation

Surface deflation was inferred to be eroding all debris flow deposits, despite not being detectable in our aerial imagery mapping. Of the 30 field sites, we identified six deposits with neither toe erosion by the axial river nor tributary channel incision. Three of these field sites were visited in 2020 during field surveys by Wall et al., (2023). For these sites, we evaluated potential changes in their surface grain size distribution. We found that all but one site (Clay Springs 1) coarsened over time, as evident by changes in the median grain size, D_{50} (Table 9). Furthermore, the D_{50} was also found to have increased at nine of the other nine sites that had previous surface grain size surveys (Wall et al., 2023; Murphy et al., 2019) but did experience toe erosion or tributary incision. While this is a small dataset, this coarsening of the deposit surfaces provides additional evidence to support the inference of surface deflation occurring at these sites. (Table 9).

Table 9. Deposit surface grain size distribution including pre-2023 field surveys and data collected during 2023 field surveys. Grain sizes are reported in the 16th, 50th, and 84th percentile in mm.

		Pre – 2023 Field Survey			**2023 Field Survey**		
Site	**Source**	D_{16}	D_{50}	D_{84}	D_{16}	D_{50}	D_{84}
PC1	Wall et al., (2023)	9.6	18.2	30.3	11.3	28.5	54.9
LF1	Wall et al., (2023)	2.2	21.3	52.4	5.6	32.0	104.8
DR1	Wall et al., (2023)	19.2	32.2	55.8	15.3	41.5	123.5
DR4	Wall et al., (2023)	10.1	19.3	36.2	6.6	16.6	50.9
DR5	Wall et al., (2023)	10.3	29.1	61.6	12.5	47.0	121.4
Sh1*	Wall et al., (2023)	11.3	26.4	50.4	10.7	36.5	85.7
S1*	Wall et al., (2023)	26.4	62.0	119.3	12.4	67.9	147.7
TM1	Wall et al., (2023)	1.3	4.2	48.2	1.6	18.6	62.7
CS1*	Wall et al., (2023)	23.1	50.7	83.7	9.2	31.2	82.7
CS2	Wall et al., (2023)	17	26.4	42.9	6.4	41.6	81.3
FC5	Murphy et al., (2019)	4.7	21.2	81.6	11.2	26.7	75.6
FC7	Murphy et al., (2019)	3.2	13.1	57.4	13.2	35.8	109.0

*Represent the sites in which we did not observe toe erosion by the axial river or tributary channel incision to occur.

The volume loss by surface deflation was found to be variable between sites, not only due to the variable surface deflation rates, but as a function of the deposit area not eroded by the axial river or tributary channel incision. Sites within the Clay Springs Fire represented the largest volume loss due to inferred surface deflation relative to the initial deposit volume across the entire dataset, at 37.3%. Generally, volume loss due to surface deflation represented a small portion of the initial deposit volumes for all 58 sites, with an average of 5.6% ± 5.3%, where the uncertainty largely results from the two applied surface deflation rates (Table 10).

Volume loss due to surface deflation remains the least constrained process identified to be eroding post-fire debris flow deposits. Additionally, although we applied a constant surface deflation rate through time, it is likely that the rate of volume loss to surface deflation diminishes over time as the deposit surface becomes increasingly armored. Therefore, our estimated volume losses due to surface deflation are reported as the average of the lower and upper bounds (Table 10).

Table 10. Summary statistics for absolute and relative volume loss by surface deflation separated by fire. The range of values results from the two surface deflation rates applied, where the lower value is from the use of 0.1 mm m^{-2} yr^{-1} and the upper value is from 5 mm m^{-2} yr^{-1}.

	Absolute Volume (m^3)			Relative Volume (% of V_{int})			
Fire	**Mean**	**Median**	**Range**	**Mean**	**Median**	**Range**	**n**
Clay Springs	57.3 ± 55.1	52.0 ± 50.0	0.9 – 248.8	9.5 ± 9.0	10.8 ± 10.3	0.2 – 37.3	6
Dollar Ridge	104.1 ± 103.1	92.0 ± 90.0	0.7 – 406.6	5.8 ± 5.5	5.1 ± 4.8	0.1 – 20.1	8
Pole Creek	57.4 ± 55.1	31.2 ±30.2	0.4 – 410.3	3.3 ± 3.1	4.2 ± 4.1	0.1 – 13.4	9
Seeley	59.8 ± 58.7	40.5 ± 37.5	0.5 – 154.6	9.4 ± 9	6.0 ± 5.7	0.1 – 20.6	6
Shingle	104.0 ± 98.4	154.2 ± 149.5	3.0 – 458.3	5.5 ± 3.7	7.1 ± 6.7	0.2 – 17.5	3
Trail Mtn.	17.3 ± 16.6	16.9 ± 16.2	0.4 – 73.5	3.6 ± 3.4	3.2 ± 3.1	0.1 – 13.0	5
Twitch.	73.4 ± 72.2	35.2 ± 33.2	0.1 – 491.5	4.5 ± 4.3	4.3 ± 4.1	0.1 – 17.3	21
Total	65.6 ± 59.7	33.0 ± 31.4	0.1 - 491.5	5.6 ± 5.3	5.2 ± 5.1	0.1 – 37.3	58

Total Volume Loss

Our estimation of erosional volumes from the three processes allowed us to evaluate the total volumetric loss in sediment for each site (Table 11). With this data, we identified the dominant erosional process at each site, defined as the process resulting in the largest total volume of erosion since deposition. The largest volumes eroded were found to be independent of the initial estimated volumes, meaning the largest deposits did not necessarily experience the most erosion. Additionally, we did not see evidence that surface deflation was greatest for the oldest deposits, suggesting that volume loss to surface deflation was more heavily influenced by the deposit area (accounting for changes due to toe erosion or tributary incision), rather than the time of exposure (Table 11). In general, toe erosion dominated throughout the dataset, with 36 of the 48 deposits that reached the river eroding predominantly by the axial river. As would be expected, we found surface deflation was the dominant erosional process for sites not reaching the axial river (n = 10), except in the case of two sites within the Trail Mountain Fire, where tributary channel incision dominated.

To understand which erosional processes were responsible for the largest magnitude of volume loss, we evaluated the relative percentage each erosional process contributed to the total volume loss at each site. Six sites did not exhibit toe erosion or tributary incision and thus surface deflation accounted for 100% of estimated erosion. For the remaining 52 sites in which there was a combination of toe erosion, tributary channel incision, and surface deflation, toe erosion was responsible for the largest relative volume loss compared to the total volume eroded. We found toe erosion on average, represented 73.2 ± 12.1% of the total volume loss across all sites in which it occurred (n = 48). The

portion of volume loss to surface deflation is reported as the average value between the upper and lower deflation rate bounds, and the reported uncertainty results from our applied upper and lower bounds. The range of percent volume loss due to surface deflation was large, accounting for 21.5 ± 13.1% when assessed for sites where it was not the only process (n = 52). Lastly, tributary channel incision represented 17.9 ± 3.4% of the total volumetric loss at sites in which it occurred (n =22). Because there is a relatively low sample size for sites in our study where tributary channel incision was observed, these estimates of relative contribution from this process may not accurately represent the true variability that could be expected.

Table 11. Volume loss due to each identified erosional process for all 58 study sites. Other metrics include the type of site (remotely mapped vs field-surveyed) and if the deposit was initially delivered to the axial river (Y = delivered, N = no delivery).

				Volume Loss (m^3)		
Site	**Site Type**	**Initially Delivered**	**Initial Volume Estimate (m^3)**	Toe Erosion	Trib. Channel Incision	Surface Deflation
DR1A	Remote	Y	4267.0 ± 199.2	432.8	110.9	8.1 – 406.6
DR2	Field	Y	221.5 ± 17.2	88.8	0.0	0.7 – 35.2
DR3A	Remote	N	3443.2 ± 185.8	0.0	0.0	7.6 – 379.1
DR4A	Remote	Y	2735.1 ± 99.3	483.0	0.0	4.1 – 202.6
DR5A	Remote	Y	1921.8 ± 79.1	172.2	0.0	3.2 – 161.4
DR1	Field	N	585.9 ± 63.9	0.0	44.0	10.4 – 130.4
DR4	Field	Y	1241.9 ± 31.9	509.1	0.0	9.1 – 65.1
DR5	Field	Y	1768.1 ± 137.0	326.4	0.0	156.6 – 279.7
FC1	Remote	Y	1801.3 ± 126.4	376.0	0.0	5.2 – 258.0
FC2	Remote	Y	1520.7 ± 105.2	177.0	48.4	4.3 – 214.8
FC3	Remote	Y	592.3 ±35.1	102.3	0.0	1.4 – 71.6
FC4_11	Remote	Y	756.7 ± 17.4	127.8	40.3	0.7 – 35.5
FC5_11	Remote	Y	2445.2 ± 14.1	817.9	0.0	0.6 – 28.7
FC7_11	Remote	Y	1481.9 ± 34.7	338.9	0.0	1.4 – 70.9
FC5_14	Remote	Y	2056.4 ± 29.2	350.5	0.0	1.2 – 59.6
FC5	Field	Y	2148.8 ± 144.7	472.1	47.9	5.9 – 295.3
FC4_18	Remote	Y	591.2 ± 12.1	124.1	51.4	0.5 – 24.8
FC7	Field	Y	975.9 ± 78.7	240.3	0.0	3.2 – 160.5
SC1A	Remote	Y	2601.3 ± 240.8	161.3	0.0	9.8 – 491.6

Table 11. (cont.)

SC2_11	Remote	Y	169.5 ± 2.3	24.0	0.0	0.1 – 4.6
SC2_14	Remote	Y	275.1 ± 8.6	46.9	33.1	0.4 – 17.6
T1	Remote	Y	2973.7 ± 211.1	167.3	0.0	8.6 – 430.7
T2	Remote	Y	440.9 ± 19.3	55.4	0.0	0.8 – 39.4
T3	Remote	Y	787.5 ± 32.0	108.4	0.0	1.3 – 65.4
T4	Remote	Y	1557.3 ± 98.6	92.5	0.0	4.0 – 201.1
T5	Remote	Y	535.0 ± 32.2	0.0	0.0	1.3 – 65.7
T6	Remote	Y	458.7 ± 20.4	60.4	0.0	0.8 – 41.6
T7	Remote	Y	225.4 ± 6.7	53.4	0.0	0.3 – 13.7
T8	Remote	N	1057.0 ± 71.4	10.1	0.0	2.9 – 145.6
LF1	Field	Y	12307.3 ± 201.1	680.1	122.2	8.2 – 410.3
LF2	Field	Y	6136.9 ± 167.4	521.3	332.5	6.8 – 341.6
PBC1	Field	Y	445.5 ± 11.2	236.7	0.0	0.5 – 22.8
PC2	Field	Y	910.6 ± 30.9	353.2	110.9	1.3 – 63.1
PC3	Field	Y	291.1 ± 20.5	136.4	7.7	0.8 – 25.1
PC4	Field	Y	557.3 ± 30.1	160.5	54.8	1.2 – 61.5
PC5	Field	Y	208.7 ± 4.4	72.7	23.8	0.2 – 9.0
PC6	Field	Y	695.8 ± 30.6	154.7	59.4	25 – 62.4
PC7	Remote	Y	1002.0 ± 422.8	172.1	19.7	0.4 – 18.3
S1	Field	N	649.3 ± 72.7	0.0	0.0	3.0 – 148.4
S2	Field	Y	261.7 ± 20.4	129.9	0.0	0.8 – 41.6
S3	Field	Y	1295.4 ± 75.7	641.8	70.1	3.1 – 154.6
S4	Remote	Y	691.9 ± 38.2	107.2	0.0	1.6 – 77.9
S5	Remote	N	210.2 ± 13.2	0.0	0.0	0.5 – 26.9
S6	Remote	Y	369.8 ± 12.4	70.9	0.0	0.5 – 25.2
Sh1	Field	N	1382.5 ± 73.0	0.0	0.0	3.0 – 149.0
Sh2	Field	Y	2400.8 ± 224.6	89.6	42.3	9.2 – 458.3
Sh3	Remote	Y	1921.9 ± 115.8	98.1	110.4	4.7 – 236.2
TM1	Field	Y	2188.1 ± 36.0	758.4	125.6	1.5 – 58.8
TM2	Field	Y	129.8 ± 8.9	35.9	9.1	0.4 – 4.3
TM3	Field	Y	385.9 ± 16,2	1.6	55.8	0.7 – 33.1
TM4	Field	Y	275.9 ± 5.1	3.3	88.2	0.2 – 10.3
TM5	Field	N	543.8 ± 16.9	0.0	0.0	0.7 – 34.6
CS1	Field	N	850.0 ± 139.6	0.0	0.0	5.7 – 170.9
CS2	Field	Y	609.2 ± 70.3	63.9	0.0	2.9 – 43.0
CS3	Field	N	195.8 ± 43.7	0.0	0.0	1.8 – 26.8
CS4	Field	Y	552.8 ± 26.9	30.1	0.0	1.1 – 47.2
CS5	Field	Y	668.1 ± 50.0	55.1	0.0	2.0 – 61.2
CS6	Field	N	132.5 ± 22.6	0.0	0.0	0.9 – 37.8

Volumetric Time-Series Analysis

Total volumetric changes (toe erosion + tributary channel incision + surface deflation) were plotted over time for all sites from the time of deposition to the year 2023. We identified similarities in trends across most sites, with the most notable being a steep decrease in volume during the first year after deposition and stabilization in the volume thereafter (Figure 12). The percentage of the initial deposit volume remaining in 2023 was variable between sites, across wildfires, and between different dominant erosional processes (Table 12). For example, deposits with the lowest percent volume remaining in 2023 (i.e., experienced the largest magnitude of erosion) were within the Pole Creek Fire, which was the youngest wildfire in our study (2018). Conversely, sites within the Clay Springs and Shingle Fires exhibited the largest percentage volume remaining in 2023, at 90.5 and 80.5% respectively. This is notable because these represented the oldest deposits in our study, originating from fires both ignited in 2012. This result highlights that the magnitude of erosion across post-fire debris flows is not dependent on the age of exposure. Rather, the total volumetric loss appeared to depend most on the magnitude of erosion occurring in the first year after deposition.

While deposit age may not be a dominant factor influencing the total volumetric loss over time, we found the dominant erosional process drives the relative magnitude of volume loss through time (Table 12). As previously mentioned, sites within the Clay Springs Fire (2012) had the highest percentage volume remaining in 2023, 90.5% of the initial volume (Table 12). Two sites within the Clay Springs Fire were dominated by toe erosion when the lower surface deflation rate was applied, but conversely, surface deflation was found to be dominant when the upper rate was applied (Table 11; Clay

Springs 4 and 5). The same pattern was true for all sites within the Shingle Fire (2012), where all three sites were eroding primarily by surface deflation when the upper rate was applied and the median of volume remaining in 2023 was additionally relatively high, at 86.7% despite the relative age of exposure (Tables 11 and 12). In general, sites inferred to be eroding primarily by surface deflation (n = 20) had the highest percent volume remaining as of 2023, with an average of 86 ± 6.8%. Sites dominated by toe erosion had the lowest percent of volume remaining as of 2023, with an average of 66.7 ± 2.5%. There were only two sites where tributary channel incision dominated, with an average percent volume remaining in 2023 of 66.8%.

Table 12. Total initial volume from all debris flows, the total estimated eroded, (where uncertainty arises from surface deflation rates), median percent remaining in 2023, and the number of sites with each dominating erosional process for each wildfire.

				Dominant Erosional Process (number of sites)		
Fire, Year	**Total Initial Deposit Volume (m^3)**	**Total Eroded Volume (m^3)**	**Median 2023 Volume Remaining (%)**	Toe Erosion	Trib. Channel Incision	Surface Defltn.
Clay Springs, 2012	3008.5 ± 353.1	227.8 ± 72.7	90.5 ± 0	1	0	5
Dollar Ridge, 2018	15621.2 ± 1376.7	3094.0 ± 727.0	71.9 ± 6.0	6	0	2
Pole Creek, 2018	22132.3 ± 1341.8	3656.2 ± 484.9	55.0 ± 0	9	0	0
Seeley, 2012	3414.6 ± 296.3	639.9 ± 159.9	71.7 ± 6.2	3	0	3
Shingle, 2012	5589.4 ± 529.1	694.6 ± 340.3	80.5 ± 4.5	0	0	3
Trail Mtn., 2018	3523.5 ± 83.1	810.5 ± 51.1	73.8 ± 0	2	2	1
Twitchell, 2010	24364.5 ± 2458.5	5532.5 ± 1341.0	71.5 ± 5.3	15	0	6
			Total	36	2	20

Exponential Decay Function Best-fit Values

Despite the observed variations in volume loss, the general trend in the erosion time-series followed a common pattern. Specifically, the percentage of volume remaining through time declined rapidly and then tended to diminish and stabilize over time (Figure 12). We therefore tested the hypothesis that rate of volume loss of post-wildfire debris flow deposits could be explained with an exponential decay function. While volume loss due to surface deflation was applied as a constant rate through time, we nonetheless included the sites dominated by surface deflation in the exponential decay analysis. The goal of this analysis was to determine if the overall pattern of erosion across all debris flow deposits could be described as an exponential decay function (Eq. 3). It was additionally hypothesized that variations in the decay rate, *r,* should reflect the variations in dominant erosional processes between sites.

In total, all but one of the 58 sites could be fit by the exponential decay model. The single exception - Fish Creek 5, 2011 from the Twitchell Canyon Fire – represented a location that experienced multiple repeat debris flows over the study period (Table 2), limiting the data available for adequately assessing or attempting to fit any type of temporal trend for the site deposited in 2011. For the remaining 57 sites, the best-fit value for the decay rate, *r*, in Eq. 3 was evaluated against the percentage volume remaining through time. Because there was a low and high estimate of volume remaining due to the two surface deflation rates, we evaluated the median percentage remaining through time (Figure 13). The geometric mean of the best-fit *r* across all sites was 0.42, with a median value of 0.59 (Table 13). For sites dominated by surface deflation, the geometric mean of

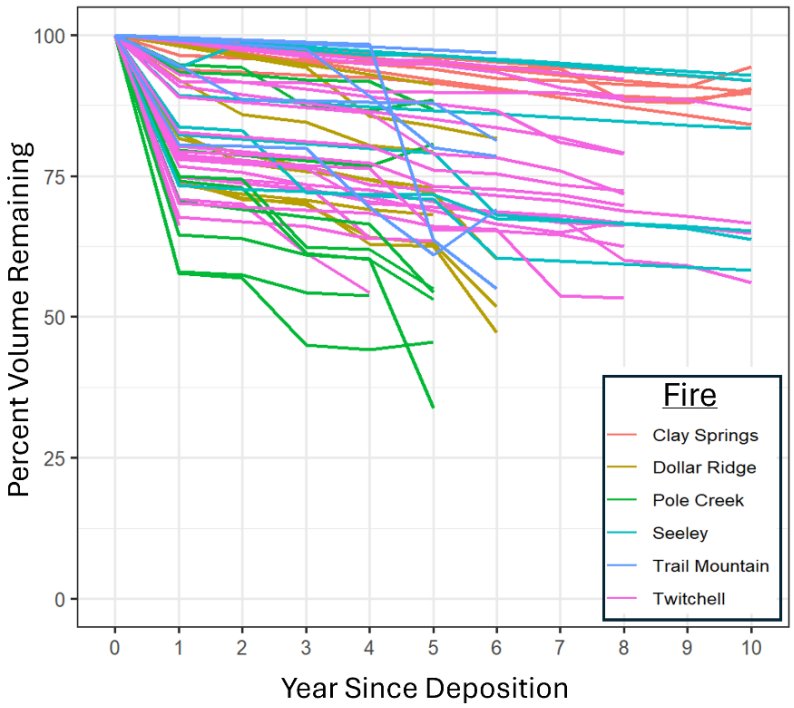

Figure 12. Volumetric time-series of all 58 sites separated by color, where the color corresponds to the appropriate generating fire. The percentage of initial volume remaining is plotted on the y-axis, while the year since observed deposition is plotted on the x-axis.

r was much lower, at 0.22, and with a median of 0.30 (n = 20). Finally, sites dominated by fluvial toe erosion (n = 35) had a much steeper decay rate, and the geometric mean of *r* was 0.60, with a median of 0.65 (Table 13). We do not report best-fit values for *r* for sites dominated by tributary channel incision due to the small sample size (n = 2). There was statistical significance in the value for *r* between dominant erosional groups evident by a p-value significantly less than 0.001 via a two-sided t-test.

Lastly, we evaluated the intercept, *c,* in Eq. 3, which represented the volume initially lost after deposition ($V_{int} - V_0$). The median percentage initially lost for all 58 sites was 17.6% centered around a geometric mean of 9.8% (Table 14). The geometric mean was lower for sites dominated by surface deflation than sites dominated by toe erosion, 2.7% versus 19.4% respectively (Table 14). Additionally, there was a larger

Table 13. Summary statistics for volume loss rate *r* in Eq. 3 for all 55 sites separated by their dominant erosional process.

Dominant Erosional Process	Geo. Mean *r*	Range *r*	Med. *r*	Std Dev. *r*	n
Toe Erosion	0.60	0.26 – 0.87	0.65	0.15	35
Surface Deflation	0.22	0.01 – 0.73	0.30	0.24	20
Total	0.42	0.01 – 0.87	0.59	0.23	55

standard deviation in the initial volume loss by sites dominated by toe erosion, while the surface deflation values for *c* were more evenly distributed around the geometric mean (9.4% and 5.1% respectively). The large range and variability in the intercept, *c,* across all sites is likely a function of initial deposit delivery into the axial river and the presence or absence of tributary channel incision on the deposit surface within the first year of deposition (Table 14). In cases where sites were only eroding by surface deflation, the initial percentage volume loss, *c* is a function only of the available deposit area and the applied surface deflation rate.

Table 14. Summary statistics for the intercept *c* in Eq. 3 for all 58 sites separated by their dominant erosional process. % represents the percent of initial volume (the average between high and low surface deflation rates).

Dominant Erosional Process	Geo. Mean c (%)	Range c (%)	Med. c (%)	Std Dev. c (%)	n
Toe Erosion	19.4	3.6 - 42.3	23.3	9.4	36
Surface Deflation	2.7	0.5 – 21.2	2.2	5.1	20
Total	9.7	0.5 – 42.3	17.6	11.8	58

Evaluation of Exponential Decay Erosion Model

To evaluate the efficacy of the exponential decay model, we evaluated the predicted volume at time *t* using Eq. 3 against the observed volume (in this case, regressed volumes for the 28 remote sites and 3D reconstructed volumes for the 30 field

sites) at time *t*. In each case, we supplied the model with the measured value of *c* at each site. Predictive models for the intercept *c* are discussed in further detail in the next section. Respective to each erosional process, modeled volumes for sites eroding primarily by toe erosion and a supplied *r* of 0.65 (Table 13) explained the variability well with an R^2 of 0.85, cross-validated R^2 of 0.60, and a mean of residuals of 0.0007. The R^2 was relatively lower for sites eroding primarily by surface deflation (where $r = 0.30$; Table 13) at 0.78, cross-validated R^2 of 0.60, and a mean of residuals of 0.0003. Overall, the exponential decay model performed worse on sites dominated by surface deflation, with many of the modeled volumes overpredicting erosion. This was especially apparent in deposits with a lower percentage of the volume remaining; in some cases, the modeled remaining volumes were half of the observed (Figure 13).

Therefore, the exponential decay function, described by Eq. 3, is most appropriate for sites eroding primarily by toe erosion via the axial river as opposed to those primarily eroding by surface deflation. Instead, estimating volume loss by surface deflation is best estimated by applying a constant rate over the deposit area. This result is to be expected, as the applied surface deflation rates were constant through time. Despite poor performance of the exponential decay function for sites dominated by surface deflation ($r = 0.30$), convergence on a solution for *r* in Eq. 3 indicates that total deposit erosion was still reasonably well described using an exponential decay function despite the differences in dominant erosional process.

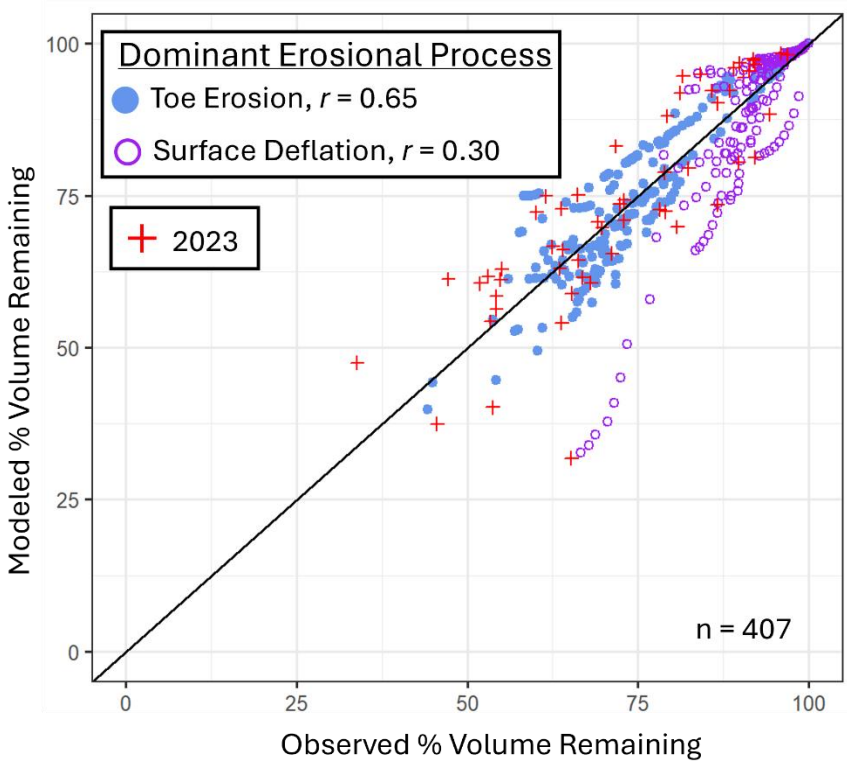

Figure 13. Modeled volumes using Eq. 3 with the relevant best-fit value for *r* based on the dominant erosional process plotted against the observed volumes in the time series. The thick black line represents a 1:1 fit.

Influence of Morphological Metrics

The estimated volumes eroded and remaining through time indicate that the dominant erosional process influences the magnitude of sediment lost between sites. However, other factors likely influence erosion of debris flow deposits, including valley bottom morphology and axial channel lateral migration rate. We evaluated hydrologic, morphometric, and sedimentological characteristics at each site that may best explain or predict variability in the initial volume loss, *c,* and the best-fit decay rate, *r,* in Eq. 3.

Initial Deposit Delivery into the Axial River

Toe erosion results in the largest magnitude of sediment loss among the three identified erosional processes (Tables 8 and 11). Therefore, initial delivery of the deposit

into the axial river is a significant contributor to the relative magnitude in volume loss of post-wildfire debris flow deposits. We observed that the 10 sites that did not initially deliver to the axial river had a total loss of toe volume due to erosion by the axial river of zero. Conversely, for the 48 sites that were initially delivered to the axial river, we found the initial volume loss was highest at the time of deposition due to the eroded channel fill. We evaluated this assumption that initial delivery is a significant contributor to overall volume loss and found a p-value of 0.01 between groups (initially delivered or not initially delivered).

Prior initial debris flow delivery models presented by Murphy et al., (2019) did not account for the river position within the valley bottom. Specifically, they assumed that if there was available space in the valley bottom for lateral river migration, then the axial river would always be pushed towards the distal valley wall by the deposit. However, we did not observe evidence to support this type of river lateral migration associated with the initial debris flow deposition. In fact, there was no statistical significance in lateral river migration from its pre-fire to post-fire location between groups of delivery. In total, less than 25% of the entire dataset had evidence of lateral migration greater than 10% of the valley bottom width after debris flow deposition in either direction (Figure 8). Nonetheless, we evaluated the ability of the Murphy et al., (2019) delivery model to explain our dataset and found it predicted false negatives (i.e., no initial delivery) on over half of our dataset. This error arises because the axial river position is not considered in their delivery model. Highlighting the need to include this factor, we found the river position before debris flow deposition was significant between delivery groups with a p-value of 0.03.

Not only is the position of the axial river in the valley bottom an important consideration for initial delivery models, but the runout length of a deposit within the valley bottom must also be considered. We evaluated the relationship between the initial deposit volume and the projected runout length (Figure 9). Based on a cube root scaling with initial volume presented by Rickenmann (1999), we found a fitting coefficient of 6.6 for predicting the runout length ($R^2 = 0.88$, cross-validated $R^2 = 0.73$):

$$R = 6.6V^{1/3} \quad \text{Eq. 4}$$

Where R represents the projected runout length (Figure 9), or the radius of an unobstructed conical wedge (in meters), and V represents the initial deposit volume (m^3).

We evaluated the relationship between runout length and x_b in initial deposit delivery by the ratio of lengths (R / x_b), defined here as the Debris Flow Delivery Potential ratio (DDP). In cases where the runout length is longer than the distance that the axial river is from the contributing margin, the debris flow deposit is sufficiently long enough to deliver sediment into the river network. Therefore, initial delivery of the debris flow deposit into the axial river is driven by the combination of the measured runout length and the distance to the river (x_b) before debris flow deposition (Figures 8 and 9). Our dataset validated this theory, in that all the sites that were initially delivered to the axial river had a DDP greater than or equal to 1, and the confusion matrix produced 100% accuracy (Figure 14).

Lastly, it should be noted that the fitting coefficient, 6.6, in the proposed runout length model (Eq. 4), is a function of reconstructed initial volumes from empirically derived field data. Modeled initial volume estimates resulting from the Gartner et al.,

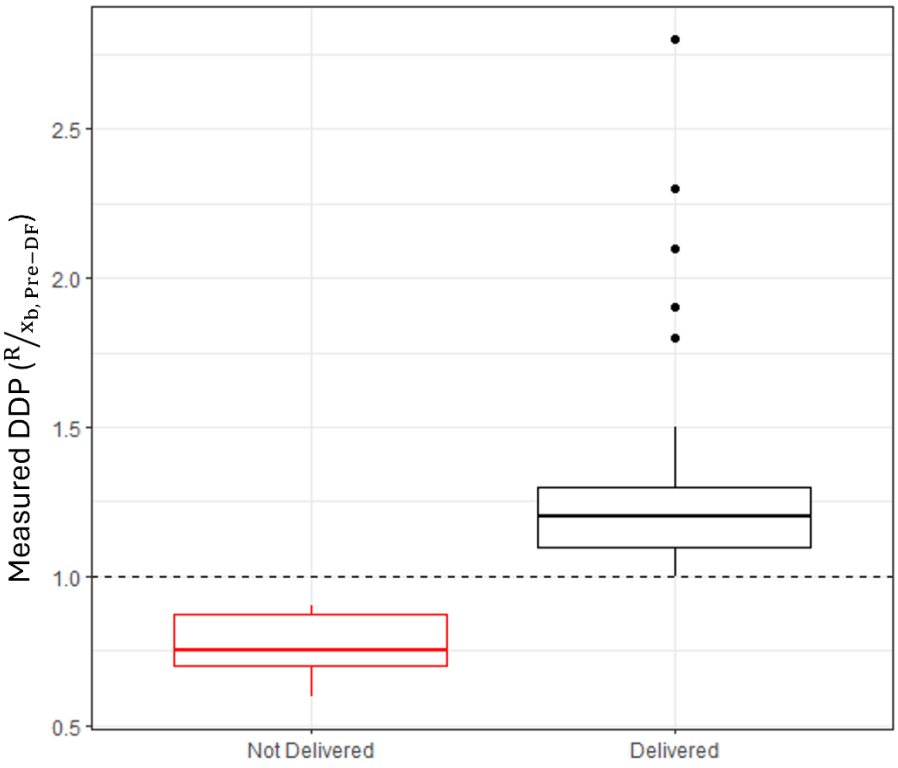

Figure 14. Debris Flow Delivery Potential (DDP) from the measured runout length and x_b. The horizontal dashed line represents a 1:1 ratio. The groups correspond to if the deposit was initially delivered to the axial river network.

(2014) or Wall et al., (2023) volume prediction models likely require a different fitting coefficient. We found that the best fitting coefficient for the initial volumes predicted for each model in our dataset were 7.5 ($R^2 = 0.70$, cross-validated $R^2 = 0.40$) for the initial volumes estimated using the Gartner et al., (2014) model and 2.8 ($R^2 = 0.69$, cross-validated $R^2 = 0.51$) for the Wall et al., (2023) estimated initial volumes.

Relative Magnitude of Volume Loss

The dominant erosional process was found to heavily influence the initial volume loss at each debris flow site. This was especially true for sites initially delivered to the axial river due to the estimated channel fill volume loss within the first year. The initial percentage volume loss ($V_{int} - V_0$), *c*, was lowest for sites that were inferred to be

dominated by surface deflation and inversely highest for sites that were dominated by toe erosion. There was statistical significance in the dominant process explained by the measured DDP (p-value = 0.003), where sites not initially delivered to the axial river were dominated by surface deflation and had a lower initial volume loss, *c*.

Because we identified the DDP as a significant predictor in initial deposit delivery into the axial river (and thus higher relative magnitude volume loss to toe erosion), we evaluated the relationship of the measured DDP and the initial percent volume loss, *c*, in Eq. 3. In our dataset, we found as the DDP increases, initial volume loss steeply increases and asymptotes at ~45% when the DDP is greater than 1 (Figure 15). Hypothetically, the upper bound of initial volume loss should exist at some percentage below 100%, in which case the deposit would be completely evacuated as channel fill in the first year. However, this scenario is unlikely, as it describes a case in which the river comprises the entire valley bottom width, which is rare in natural settings. Additionally, because the initial volume loss is heavily dependent on the estimated channel fill volume, which was estimated as a function of modeled bankfull depths from regional curves (Bieger et al., 2015; Figure 5), we evaluated the effect of bankfull depth against the initial volume loss and measured DDP (Figure 15).

We found the estimated channel fill volume represented 50 to 55% of the initial volume of sediment delivered (Tables 4 and 6), and therefore, estimates of initial volume loss may be most sensitive to uncertainties surrounding the bankfull depth estimated from regional curves (Bieger et al., 2015). This is most obvious at high values for the DDP, in which the initial debris flow deposit was delivered to the axial river, but the channel fill

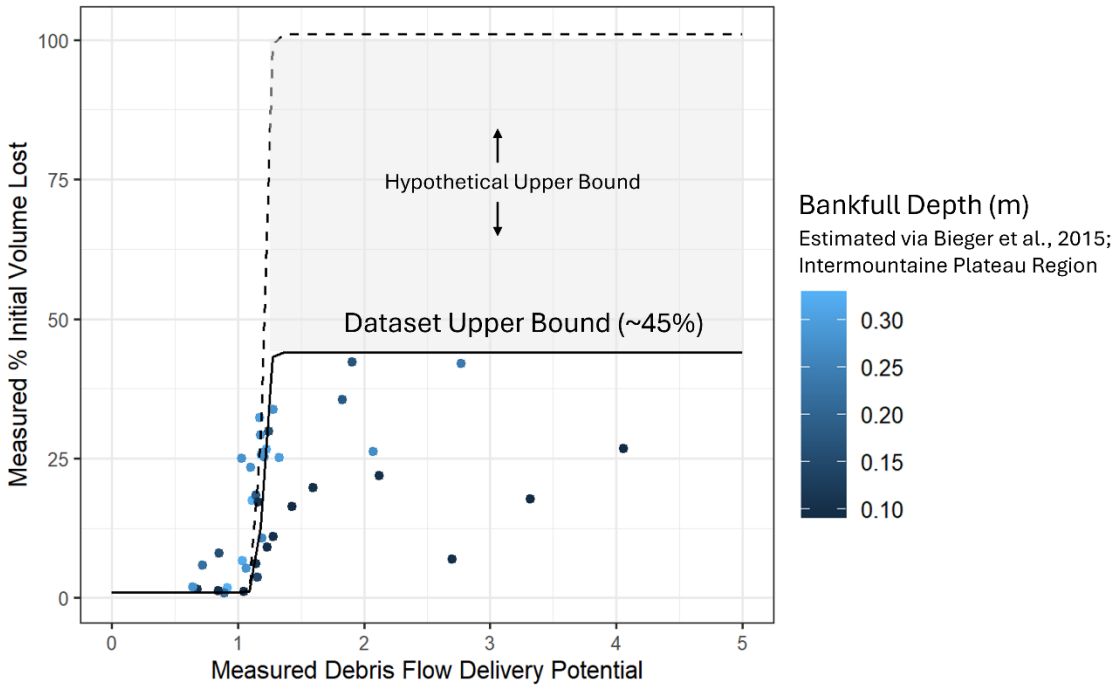

Figure 15. The relationship of measured DDP to the measured initial volume loss at the time of deposition for all 58 sites. The black line represents the upper bound identified in the dataset. The dashed line and grey rectangle represent the hypothetical upper bound. The color of the dots represents the estimated bankfull depth included in the channel fill volume estimate (Bieger et al., 2015).

volume was relatively small compared to the initial deposit volumes (Figures 15 and 5; Tables 4 and 6).

In addition to examining the variability in initial volume loss, *c* in Eq.3, we evaluated factors that may influence the decay coefficient *r.* Our analysis of total volumetric loss indicated that sites eroding primarily by toe erosion can be accurately described using an exponential decay model, where the median value for *r,* 0.65, in Eq. 3 predicted volume loss through time (Table 13; Figure 13). We found the measured initial volume loss, *c,* and the measured DDP were the most significant predictors in the decay rate *r* (correlation coefficient of 0.68 and 0.50 respectively). This further validates the suggestion that initial deposit delivery is one the most important predictors for

constraining the rate of erosion for post-wildfire debris flows; debris flows that reach and initially deposit sediment into the axial river will experience the largest magnitude of volume loss through time, and generally exhibit steeper decay rates.

Despite values for *r* being most dependent on initial volume loss, *c*, the range of values for *r* was relatively large in the toe erosion dominated dataset, between 0.26 and 0.87 (Table 13). Therefore, we evaluated differences in the *r* based on various hydrologic, morphometric, and sedimentological metrics for the toe erosion dominated sites to understand if the range of values was predictable. First, we evaluated data collected from cross-sectional surveys of the axial channel at 25 of the visited sites (Table 3). Data includes estimates of the cross-sectional geometry of the channel (i.e., cross-sectional area, and hydraulic radius) at its estimated maximum depth before overflowing into the floodplain or onto the adjacent debris flow deposit, as well as the channel slope at each cross-section. With this data, we evaluated metrics informing river competency, specifically the estimated shear stress, total, and unit stream power (Shields, 1936; Bagnold, 1966).

In the field, we observed many channel beds that were well armored as well as axial channel cross-sections that were composed of unstable banks without a clear bankfull elevation. In addition, the slope observed from the longitudinal profile at each site in which we surveyed the axial channel averaged 0.04 (4%) and was centered around the same median of 4%. Steep slopes through the debris flow deposit reaches resulted in large values for stream power and boundary shear stress, suggesting competent reaches at high flows (Bagnold, 1966; Shields, 1936). All but two axial channels were observed to be incised into previous valley fill, suggesting the axial river was disconnected from the

floodplain or debris flow deposit. This observation was validated by the axial channel width to depth ratios, where in all cases observed to be disconnected from the adjacent debris flow deposit exhibited width to depth ratios less than 20. Low width to depth ratios are indicative of a channel that is entrenched or incised, whereas high ratios are indicative of aggrading reaches (Millar and Benda, 2000). In cases in which the axial river was not observed to be incised or disconnected to the adjacent floodplain or deposit, width to depth ratios were much higher at the relevant cross-section, ranging from 24- 41 (Figure D.1). Despite these observations, we did not find any statistical significance between width to depth ratios in the axial river in predicting the value for *r* for sites initially delivered into the axial river.

While the pattern of steep, incised, and disconnected channels was common across surveyed cross-sections, the grain size distribution between the channel bed and debris flow surface was variable and significant between the identified dominant erosional process. Specifically, we found that the channel bed was much coarser or similar in distribution to the debris flow deposit surface for sites identified to erode primarily by toe erosion. The opposite was true for sites eroding primarily by surface deflation, where grain size distributions were evident of a channel bed that was significantly finer than the debris flow deposit surface (Figure 16). Despite these observations, we did not find any statistically significant predictor variables between channel depth, slope, unit and total stream power, estimated total shear stress, or hydraulic radius in describing variance between values of *r*.

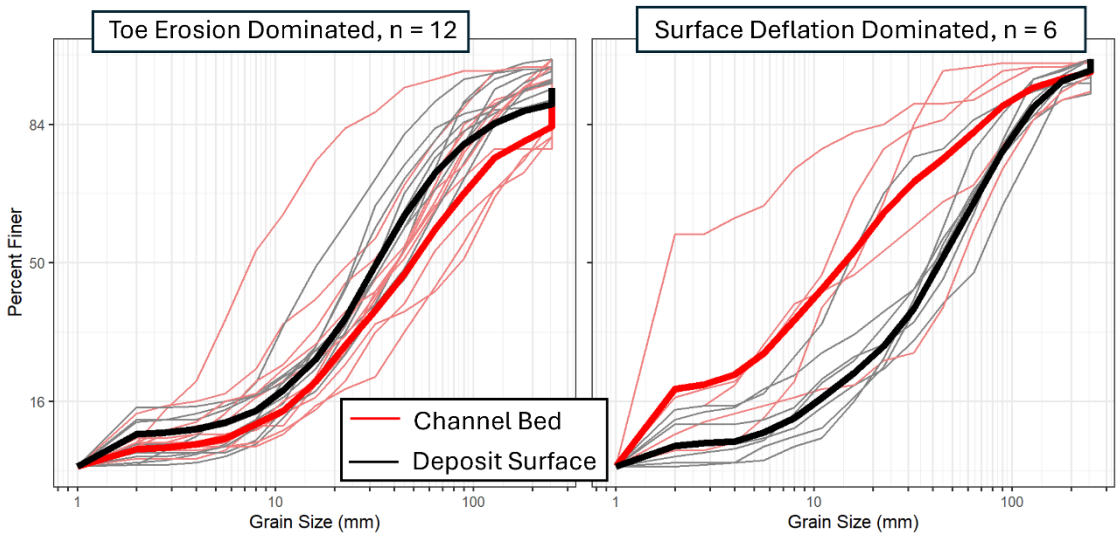

Figure 16. Grain size distribution data collected from 2023 field surveys of the channel bed and deposit surface. The plots are separated by the dominant erosional process, where the red line represents the distribution of the channel bed, and the black line represents the distribution of the debris flow deposit surface. Thick lines represent the aggregate dataset for each plot.

We further evaluated geospatially measured morphological metrics including the confluence angle, the estimated river slope from 10-meter DEMS, the 1-km reach averaged channel confinement, 1-km reach averaged channel sinuosity, and the lateral channel migration. Across the 57 sites, we did not find any significant predictor variables related to morphological metrics that could explain the variability in *r* values.

SUMMARY AND DISCUSSION

The volumetric analysis of post-wildfire debris flow deposits presented here is aimed at understanding the rate at which sediment is eroded from deposits after wildfire. Field survey data detailing the elevation of the surfaces of post-wildfire debris flow deposits was used to reconstruct the initial deposit volume as well as model the relationship between deposit area and volume for sites that were not visited in the field.

We found deposit initial volume estimates for the 30 field sites were reasonable for volumes of post-wildfire debris flows in Utah, specifically with the Wall et al., (2023) volume model (Figure 11). However, many initial volumes were underpredicted by Wall et al., (2023) model, likely because the authors did not consider “missing” channel fill or volume loss to surface deflation in their estimates of initial deposit volumes, which would result in a systematic underestimate of deposit volumes (Wall et al., 2023). Despite discrepancies in published volume prediction models, we suggest the results of the initial volume estimates produced from empirical field data are within a reasonable range of debris flow deposit initial volumes for the Intermountain West and areas outside of the transverse California ranges (Wall et al., 2023). Additionally, our regression of deposit areas versus measured volumes indicates that we can accurately estimate the initial deposit volumes based on their area using the power-law relationship described by Eq. 1 (Table 5).

We documented three erosional processes responsible for reducing sediment volumes from post-wildfire debris flow deposits. Two processes were observed via aerial imagery and resulted in losses to the deposit areal extent: toe erosion by the axial river and tributary channel incision into the surface of the deposit. Additionally, we observed field evidence of a third erosional process, defined here as surface deflation, which is a result of sheetwash erosion and runoff processes occurring over the debris flow deposit surface. The occurrence of surface deflation was further supported by field data suggesting a coarsening of the surface sediment over time (Table 9).

Sites dominated by toe erosion had the largest magnitude of volume loss through time compared to those that were dominated by tributary channel incision. Furthermore,

toe erosion dominated sites that were initially delivered to the axial river. We found initial deposit delivery to be a function of the runout length and the distance the axial river is from the contributing margin (Figure 8 and 9). Notably, we documented little to no lateral migration by the axial river after deposition into the valley bottom. This observation indicates the position of the river in the valley bottom must be considered in initial delivery models. With the observation that initial delivery not only is a function of the deposit runout length but is additionally a function of the river position within the valley bottom, we evaluated morphological metrics influencing x_b, specifically the 1-km reach-averaged channel confinement. As channel confinement increases, the distance of the axial river from the contributing margin approaches a single value. The dataset in this study was relatively small (n = 18) due to the temporal and spatial limitations in pre-fire imagery to build a predictive model. However, the concept is logical: as the valley width narrows, the space available for the axial river to occupy becomes increasingly limited. Thus, more confined reaches have a higher likelihood of initial debris flow delivery into the axial river. Therefore, the magnitude of deposit volume loss is highest for sites that are initially delivered to the axial river due to toe erosion, and this initial delivery is more probable in highly confined channels or for deposits with a larger initial volume and longer runout length (Eq. 4).

The river position within the valley bottom, x_b, (Figure 8), was found to decrease asymptotically as confinement increased, due to the decreasing space available as the valley bottom narrows. In cases where the debris flow deposit was initially delivered to the axial river, the axial river tended to be much closer to the contributing margin than for sites that were not initially delivered. A similar trend was found in the dominating

erosional process, where sites in less confined reaches were generally dominated by surface deflation, and more confined sites were dominated by toe erosion by the axial river. This is to be expected, as the runout length relative to the distance to the river, was established to be a function of the initial volume and runout length of the deposit, as well as the channel confinement. With these observations, we proposed a new metric, the Debris Flow Delivery Potential (DDP) ratio, that defines the runout length relative to the distance to the axial river (x_b). Using the DDP to evaluate the debris flow delivery to the axial river, we found it accurately predicted initial delivery when the DDP is greater than or equal to 1 (Figure 14).

We further evaluated the effect of DDP on the initial volume loss at the time of deposition for the 58 identified sites. We found that when DDP was less than 1, meaning the deposit was not initially delivered to the axial river, initial volume loss was very low. As DDP increased above 1, the initial volume loss steeply increased and plateaued at ~45% (Figure 15). Due to the uncertainty surrounding the "missing" channel fill volume estimate, outliers in the dataset were possibly due to estimates of the shallow bankfull depths (Figures 15 and 5). Because estimates of channel fill volume can represent ~50% of the initially delivered volume (Tables 4 and 6), estimates of initial volume loss may be most sensitive to uncertainties surrounding the bankfull depth estimated from regional curve, especially at high values for the DDP (Bieger et al., 2015; Figure 15). Therefore, the best model for explaining the volume initially lost to the axial river will likely require a more robust estimate of the channel fill volume, which is limited in current available data. Conceptually, however, it is clear for sites that are initially delivered to the axial river, as evident by DDP >= 1, the initial volume loss, *c*, increases rapidly, likely as a

function of the axial river morphology at the time of deposition and the subsequent channel fill volume. The DDP ratio proved to be a reliable metric for not only predicting whether a debris flow would be delivered (Fig 14) but also the relative magnitude of sediment initially delivered to the axial river (Figure 15). This relationship, therefore, provides a potentially promising approach for predicting the fitting coefficient (c) needed to scale exponential decay curves in Eq. 3.

Despite initial delivery into the axial river, nine of the identified delivered sites were not dominated by toe erosion but appear to be dominated by surface deflation. Discrepancies in this pattern are likely due to local variations in channel morphology. For example, one site, S2 within the Seeley Fire, was initially delivered to the axial river, but the erosion was dominated by surface deflation, not toe erosion. In this case, the axial river was observed to be dammed by large woody debris, and the grain size distribution of the channel bed was dominated by fine sand. While toe erosion tends to dominate in sites delivered to the axial river, local geomorphic controls may have large impacts on the hydrologic efficiency in transporting the supplied debris flow sediment. Therefore, local sediment bottlenecks may indicate hydrologically inefficient reaches, where the axial river may be unable to erode the debris flow sediment, and the channel bed instead is aggrading at the debris flow deposit (Arditti et al., 2023).

A similar pattern of toe erosion by the axial river not dominating despite initial delivery was observed at two sites within the Clay Springs Fire. Notably, the Clay Springs Fire burned in primarily intermittently flowing watersheds (Table 1). At these sites, there was no evidence of local geomorphic controls, such as wood jams, but instead the absence of competent flows. We additionally saw a relatively low absolute volume

loss in sites within the Clay Springs burn perimeter, indicating that the absence of competent flows in the axial river influences the overall volume loss at these sites. Not only was Clay Springs an intermittent system, but annual precipitation and runoff were the lowest in our dataset within this burn perimeter (Table 1). Low precipitation and runoff may translate to lower surface deflation rates, implying that most of the sediment supplied from post-wildfire debris flows is stored within the valley bottom, rather than transported downstream. Our observations of sites that are eroding primarily via surface deflation, or more specifically, not dominated by the toe erosion from the axial river, indicate that systems broadly characterized as transport limited are likely to have less debris flow sediment eroded from the supplied deposits. In fact, grain size distributions between the axial channel bed and the debris flow sediment was overall finer than the debris flow surface (Figure 16). It can be inferred that sites that are dominated by surface deflation may be transport limited, in that most of the sediment is stored within the channel and valley bottom due to the absence of competent flows.

On the contrary, grain size distributions between the axial channel bed and the debris flow surfaces show that in all but one case, the channel bed sediment was much coarser or similar to the supplied debris flow sediment for sites that were dominated primarily by toe erosion (Figure 16). It is probable that sites dominated by toe erosion via the axial river are generally capable of removing the fine sediment supplied from the debris flow deposit, and the channel bed becomes armored with time. This is especially true in systems that are not limited in flow and easily transport the fine sediment supplied to them (Dietrich et al., 1989). Field observations were evident of axial channels that were incised, comprised of unstable banks, and disconnected from the adjacent floodplain

or debris flow deposit. Similar patterns were observed in previous research (i.e., Hoffman and Gabet, 2007), where the surveyed channels through the debris flow deposit were entrenched and incised, evident by low width to depth ratios (Millar and Benda, 2000). Additionally, in the 2007 post-fire study by Hoffam and Gabet, the authors determined that coarsening of the median channel grain size downstream of the debris flow deposit was evidence of a channel able to winnow fines and mobilize coarse gravel at high flow. These observations further highlight that the magnitude of sediment eroded from debris flow deposits over time is a complex relationship between flow regime, sediment transport, and reach morphology.

At the sites in which debris flows are eroding by the axial river, debris flows are likely to stabilize quickly, as the axial river lateral migration rates appear to be low in the identified study sites, and thus the axial river is not eroding further into the deposit toe through time. The observation of low migration rates could simply be due to the temporal scale in which we are observing the axial river after debris flow deposition. Additionally, the channel slopes were relatively steep near debris flow deposits, likely because the axial river is increasing slope to meet the increased sediment supply. If the axial channel continues to incise, the unstable banks will collapse into the bed. If the bed material is too coarse, the axial channel may aggrade, decrease its slope, and widen its banks. With the temporal scale of this dataset, it is probable the axial channel has not yet reached equilibrium and is actively incising to increase its slope. Therefore, it will continue to adjust its slope until it reaches equilibrium between the sediment supplied and the sediment transported through the reach (Hoffman and Gabet, 2007). More data is needed to understand how the axial channel adjusts its morphology to an increased sediment

supply, and additionally, the temporal scale in which this occurs. Arguably, the most important factor missing in understanding channel response to post-wildfire debris flow deposits is the channel response within the first year of deposition. In this study, we assumed the channel fill is immediately excavated within the first year, however, more information within the first year of deposition is crucial to understanding the rate at which the axial channel equilibrates and thus stabilizes at the debris flow toe. In locations lateral migration rates are higher, decay rates may be steeper as the axial river meanders throughout and erodes a larger portion of the debris flow deposit.

Despite variability in the dominant erosional process between sites, we found the magnitude of volume loss over time could be described with an exponential decay function. While the general shape of the volume loss through time for sites dominated by surface deflation converged on a solution for r in Eq. 3, we found the model performed relatively poorly for these sites (Figure 13). Therefore, a better estimate of volume loss due to surface deflation is found by applying the surface deflation rate over the deposit area rather than attempting to fit it to an exponential decay function with a low decay rate. In many cases, the sites in which surface deflation was the dominant erosional process, the area did not change significantly through time, and thus the volume loss by surface deflation is a simple function of a rate applied to a constant area. However, because we had no empirical measurements of surface deflation, we were limited to simply estimating a plausible range of surface deflation rates and have no insights into whether surface deflation rate is actually constant or variable through time.

For this analysis, we applied both a high and low constant surface deflation rate over the remaining area, but it is likely that the surface deflation rate varies in time,

decreasing as the deposit surface coarsens and becomes armored and/or vegetated. As a deposit becomes more stable through time, we would expect to see the rate of volume loss due to surface deflation decrease. More data is needed to accurately constrain the rate at which surface deflation contributes to overall volumetric loss through time. Further constraining surface deflation rates likely requires knowledge of the local precipitation, debris flow and tributary catchment slope, and local ecological succession following wildfire (i.e., vegetation regrowth). Future work should be centered around larger temporal datasets of depth and volumetric change due to each of the identified erosional processes. Specifically, surface deflation rates could be obtained via terrestrial lidar scanning and/or frequent depth measurements at sites that are deposited on hillslopes or not initially delivered to the axial river, in which the only erosional process occurring on the deposit is surface deflation.

While the exponential decay function described by Eq. 3 was not appropriate for predicting the volume remaining through time for sites primarily eroding by surface deflation, we found it performed well on the dataset in which sites were dominated by toe erosion (Figure 13). However, we were unable to find any statistically significant predictor variables in explaining variability in the decay rate, r, for the 35 sites primarily eroding by toe erosion by the axial river. Overall, observations of the volumetric time series analysis for these sites, as well as the median value for r (0.65), make it clear that sites dominated by toe erosion stabilize much more quickly. Stabilization of these sites likely results due to variability in the axial river flow magnitude and its ability to armor its bed through time. It is possible that variation between decay rates in sites dominated by fluvial erosion is driven by bank stability and channel widening as the axial channel

rebuilds its banks, and the channel cross-sections collected in 2023 did not capture the dynamic axial channels in time after deposition. Future work should focus on understanding channel evolution following the input of debris flow sediment, specifically how the channel evolves immediately after deposition and each year following. It is possible that decay rates could be improved with a better understanding of changes to flow regime, channel geometry, axial channel lateral migration rates, and/or bank stability by the axial river through time. Within the context of available temporal data of debris flow volume loss through time, we conclude that generally, sites initially delivered to the axial river (as predicted by the DDP), can be best predicted with a decay rate, $r = 0.65$ in Eq. 3 (Figure 13).

The common predictor variable in all presented processes is channel confinement. We find that the processes that dominate at the time of deposition set the stage for erosion on the decadal scale. For example, the DDP is a function of the river position relative to the contributing margin (x_b), which we found to be related to channel confinement. Post-wildfire sediment sourced from debris flows is more likely to be delivered into the river network in confined valley settings. Additionally, in confined reaches, toe erosion dominates erosion of debris flow deposits over time. This is evident at the burn perimeter scale; for example, in the Seeley Fire, half of the identified study sites were dominated by toe erosion, while the other half were dominated by surface deflation. Notably, the three sites that were dominated by surface deflation and the three sites dominated by toe erosion were in separate watersheds (Table 1). The three sites driven by surface deflation had confinement values from 0.01 to 0.12 (relatively unconfined), while the sites driven

by toe erosion had confinement values from 0.36 to 0.42 (partly confined) (Benda et al., 2007).

To estimate the rate of erosion of post-wildfire debris flow deposits on the decadal scale, it is essential to first understand the factors influencing initial deposit delivery into the axial river. We present a conceptual model that first starts at estimated debris flow deposit initial volume, which determines the runout length (Rickenmann, 1999; Murphy et al., 2019; Eq. 4). Predictions of initial deposit volume are generally based on short-duration rainfall intensities and burn severity characteristics in the debris flow generating catchment (Gartner et al., 2014; Wall et al., 2023). Secondly, we find that channel confinement is an important predictor for the resulting value for $x_{b,}$ that is the distance that the axial river is from the contributing margin (Figure 8). Estimates of the axial river position and the runout length inform the DDP ratio, which is a useful metric to estimate not only initial deposit delivery into an axial river, but also the initial percentage volume loss, *c* (Figure 16). Sites initially delivered to the axial river, especially in systems with frequent competent flows, are likely to erode primarily by toe erosion. For these cases, the rate of volume remaining through time can be fit with an exponential decay function, Eq. 3, where $r = 0.65$ for the available data. For cases in which the debris flow deposit is not initially delivered to the axial river, either due to a small deposit runout length or an unconfined valley, surface deflation is likely to dominate across the deposit.

Lastly, we were unable to constrain the factors driving variability in the volume loss primarily due to tributary channel incision with the available data (n = 2). This is a crucial process to understand, as we observed that in some cases erosion by the tributary channel can exceed the depth of the deposited debris flow, and may represent a

substantial volume of sediment delivered to the axial river. In our dataset, the volumes loss to tributary channel incision were relatively low, with one exception of a site with a 33% volume loss due to tributary channel incision. Erosion due to tributary channel incision may not be significant in large debris flow deposits, especially compared to the volume eroded at the toe by the axial river. However, at smaller debris flow deposits, tributary channel incision may represent a large portion of the overall volume loss.

CONCLUSION

We evaluated volumetric change for 58 unique post-wildfire debris flow deposits resulting from seven different wildfires in the state of Utah (Figure 2). For 30 sites, we estimated deposit volumes based on field surveys, and for the remaining 28 sites not visited in the field, we applied an area-volume relationship developed from our field data. Additionally, we identified three processes responsible for eroding post-wildfire debris flow sediment through time: toe erosion by the axial river, tributary channel incision on the surface, and surface deflation across the deposit surface. The largest magnitude of sediment was lost at sites that initially delivered sediment to the axial river.

We found that the volume eroded from post-wildfire debris flow deposits over time could, at least in the cases of sites initially delivered to the axial river, be reasonably modeled as an exponential function. First, we presented a new metric, the Debris Flow Delivery Potential ratio, to estimate the likelihood of a debris flow being delivered to the axial river. The DDP is the ratio of the runout potential of a debris flow, predictable to the first order by its initial volume and the position of the axial river within the valley bottom, where DDP = $\frac{R}{x_b}$. In general, our findings suggest that more confined reaches are

more likely to deliver sediment into the axial river network, and that sites with a DDP ≥ 1 will have the largest initial volume loss due to the delivery of channel fill sediment within the first year. Estimating the initial volume loss as a function of the DDP closes a significant knowledge gap surrounding the magnitude of sediment delivery within the first year of debris flow deposition. Debris flows deposited into confined systems are likely to deliver larger volumes of sediment within the first year, but the deposits appear to stabilize quickly.

For debris flows that are not eroded primarily by toe erosion, either due to runout lengths not sufficiently long enough to reach the axial river or an absence of competent flows, erosion primarily occurs from surface deflation. For the scope of this study, we estimated volume loss to surface deflation based on a range of constant applied rates of a lower and upper bound (0.1 to 5 mm m^{-2} yr^{-1} respectively). However, it is possible to likely that surface deflation rates decrease with time as the deposit surface stabilizes due to vegetation establishment or armoring of the deposit. Constraints on the rates at which surface deflation removes sediment from post-wildfire debris flows deposits are lacking. Future work should focus on measuring surface deflation rates in different hydrologic and climatological regimes.

Post-wildfire debris flow deposits remain an area of ongoing research due to their ability to alter instream river networks and cause damage to downstream infrastructure and communities. Wildfire prevalence and burn severity is projected to increase in the western US, and watersheds will continue to remain vulnerable to the effects of wildfire (Abazataglou and Williams, 2016; Westerling et al., 2011; Murphy et al., 2018). It remains crucial to continue advancing our understanding and predictive capabilities

related to the risks associated with wildfire and increased sedimentation. The models and observations presented in this research address critical knowledge gaps in understanding the temporal dynamics of post-wildfire debris flow sediment supply to river networks. The findings improve our understanding of post-wildfire geomorphic response and can be applied to improve assessments of watershed vulnerability to increased sedimentation following wildfires that generate debris flows.

REFERENCES

Abatzoglou, J. T., & Williams, A. P. (2016). Impact of anthropogenic climate change on wildfire across western US forests. *Proceedings of the National Academy of Sciences*. 113(42), 11770-11775.

Akaike, H. (1974). A new look at the statistical model identification. *Transactions in Automatic Control.* 19(6), 716-723.

Arditti A., Murphy B. P., Belmont P., Yocom L., Czuba J. (2023). Control on Sediment Connectivity in Fluvial Networks Impacted by Wildfire Across Utah. *All Graduate Theses and Dissertations, Utah State University*. https://doi.org/10.26076/9798-ca73

Baty F., Ritz C., Charles S., Brutsche M., Flandrois J-P., Delignette-Muller M-L. (2015). A toolbox for Nonlinear Regression in R: The Package nlstools. *Journal of Statistics and Software.* 66(5), 1-21.

Beakes M. P., Moore J. W., Hayes S. A., Sogard S. M. (2014). Wildfire and the effects of shifting stream temperature on salmonids. Ecosphere. 5(5). https://doi.org/ 10.1890/ES13-00325.1

Benda L. & Dunne T. (1997). Stochastic forcing of sediment supply to channel networks from landsliding and debris flow. Water Resources Research. 33(12), 2849-2863.

Benda L., Miller D., Bigelow P., Andras K. (2003). Effects of post-wildfire erosion on channel environments, Boise River, Idaho. Forest Ecology and Management. 178(1-2), 105-119.

Benda L., Miller D., Andras K., Bigelow P., Reeves G., Michael D. (2007). NetMap: A New Tool in Support of Watershed Science and Resource Management. Forest Science. 53(2), 206-219. https://doi.org/10.1093/forestscience/53.2.206.

Bieger K., Rathjens H., Allen P. M., Arnold J. G., (2015) Development and Evaluation of Bankfull Hydraulic Geometry Relationships for the Physiographic Regions of the United States. *Journal of American Water Resources Association.* 51(3) ,842-858.

Blair T. C. & McPherson J. G. (2009). Processes and Forms of Alluvial Fans. *Geomorphology of Desert Environments.* 413-467. https://doi.org/10.1007/978-1-4020-5719-9_14.

Boisramé G. B., Brown T. J., Bachelet D. M. (2022). Trends in western USA fire fuels using historical data and modeling. *Fire Ecology*. 18(1), 8. https://doi.org/10.1186/s42408-022-00129-4

Brogan D. J., Nelson P. A., MacDonald L. H. (2019). Spatial and temporal patterns of sediment storage and erosion following a wildfire and extreme flood. *Earth Surface Dynamics*. 7(2), 563-590.

Brown T. C., Hobbins M. T., & Ramirez J. A. (2008). Spatial distribution of water supply in the coterminous United States. *JAWRA Journal of the American Water Resources Association*, 44(6), 1474-1487.

Brown T.C., Mahat V., Ramirez J. A. (2019). Adaptation to Future Water Shortages in the United States Caused by Population Growth and Climate Change. *Earth's Future.* 7(3), 219-234.

Bull, W. B. (1977). The alluvial-fan environment. *Progress in Physical Geography:Earth and Environment.* 1(2). 222-270. https://doi.org/10.117/0309133377001020.

Choate, G. A. (1965). Forests in Utah. *U.S. Forest Service Resource Bulletin INT-4.*

Czuba, J. A. (2018). A Lagrangian framework for exploring complexities of mixed-size sediment transport in gravel-bedded river networks. *Geomorphology*. 321, 146–152. https://doi.org/10.1016/j.geomorph.2018.08.031.

Daneshi A., Brouwer R., Najafinejad A., Panahi M., Zarandian A., Maghsood F. F. (2020). Modelling the impacts of climate and land use change on water security in a semi-forested watershed using InVEST. *Journal of Hydrology.* 593, 125621.

David S. R., Murphy B. P., Czuba J. A., Ahammad M., Belmont P. (2023). USUAL Watershed Tools: A new remote toolkit for hydro-geomorphic delineation. *Environmental Modelling and Software.* 159, 105576.

Dettinger M., Udall B., Georgakakos A. (2015). Western water and climate change. *Ecological Applications.* 25(8), 2069-2093.

Dietrich W. E., Kirchner J. W., Ikeda H., Iseya F. (1989). Sediment supply and the development of the coarse surface layer in gravel-bedded rivers. *Nature*. 340, 215-217.

Eidenshink J., Scwind B., Brewer K., Zhu Z., Quayle B., Howard S. (2007). A Project for Monitoring Trends in Burn Severity. *Fire Ecology Special Issue.* 3(1).

Gartner J.E., Cannon S. H., Santi P. M, Dewolfe V. G., (2008). Empritical models to predict the volumes of debris flows generated by recently burned basins in the western U.S. *Geomorphology*. 96 (3-4), 339-354.

Gartner J. E., Cannon S. H., Santi P. M. (2014). Empirical models for predicting volumes of sediment deposited by debris flows and sediment-laden floods in the transverse ranges of southern California. *Eng Geol* 176, 45–46.

Giles P. T., Whitehouse B. M., & Karymbalis E. (2016). Interactions between alluvial deposits and axial rivers in Yukon, Canada and Alaska, USA. *Geological Society London Special Publications.* 440(1). https://doi.org/10.1144/SP440.3

Gorr A. N., McGuire L. A, Youberg A. (2023). Empirical Models for Postfire Debris-Flow Volume in the Southwest United States. *Journal of Geophysical Research: Earth Surface*.

Graf W. L., Wohl E., Sinha T., Sabo J. L. (2010). Sedimentation and sustainability of western American reservoirs. *Water Resources Research.* 46(12).

Grob, J. (2003). *Linear regression* (Vol. 175). Springer Science & Business Media.

Hallema D. W., Robinne F., Bladon K. D. (2018). Reframing the Challenge of Global Wildfire Threats to Water Supplies. *Earth's Future.* 6(6), 772-776.

Halofsky J. E., Peterson D. L., Ho J. J., Little N. J., Joyce L. A. (2018). Climate change vulnerability and adaptation in the Intermountain Region. *Gen. Tech. Rep. RMRS-GTR-375. Fort Collins, CO: U.S. Department of Agriculture, Forest Service, Rocky Mountain Research Station.* Part 1. Pp. 1-197.

Haas T., Braat L., Leuvan J. R. F. W., Lokhorst I. R., Kleinhans M. G., (2015). Effects of debris flow composition on runout, depositional mechanisms, and deposit morphology in laboratory experiments. *JGR Earth Surface.* 120 (9), 1949- 1972.

Hill R., Weber M., Leibowitz S., Olsen A., Thornbrugh D. (2015) The StreamCatchment (StreamCat) Dataset: A database of watershed metrics for the conterminous United States. JAWRA, 52, 120-128.

Hoffman, D. F., & Gabet, E. J., (2007). Effects of sediment pulses on channel morphology in a gravel-bed river. *Geological Society of America Bulletin* 119(1-2), 116-125. doi:10.113b25982.1

Hohner A. K., Cawley K., Oropeza J., Summers R. S. Rosario-Oritz F. L. (2016). Drinking water treatment response following a Colorado wildfire. *Water Research.* 105, 187-198.

Homer C.H., Fry J.A., and Barnes C.A., (2012). The National Land Cover Database. *U.S. Geological Survey Fact Sheet*. 2012-3020, 4 p.

Iverson, R. M. (1997). The physics of debris flows. *Reviews of Geophysics.* 35 (3), 245-296.

Kenney T., Wilkowske C., Wright S. (2007). Methods for Estimating Magnitude and Frequency of Peak Flows for Natural Streams in Utah. *USGS Scientific Investigations Report 5158*.

Khatri K. B., & Strong, C. (2020). Climate Change, Water Resources, and Potential Adaptation Strategies in Utah. *Utah Department of Natural Resources, Division of Water Resources.* [Available at https://water.utah.gov/wp-content/uploads/2020/09/Final-Report_ClimateChangeUtah_May_2020.pdf].

Kirchner J.W., Finkel R., Riebe C.S., Granger D. E. (2001). Mountain erosion over 10 yr, 10 k.y., and 10 m. y. time scales. *Geology*. 29(7).

Kuhn, M. (2008). Building Predictive Models in R Using the caret Package. *Journal of Statistical Software*, 28(5), 1–26. doi:10.18637/jss.v028.i05

Leeder M. R., & Mack G.H. (2001). Lateral erosion ('toe-cutting') of alluvial fans by axial rivers: implications for basin analysis and architecture. *Journal of the Geological Society, London.* 158, 885-894.

Leopold L. B., Wolman G. M., Miller J. P. (1995). Fluvial Processes in Geomorphology. *Dover Publications.* ISBN:0486685888.

Martin, D. A. (2016). At the nexus of fire, water, and society. *Philosophical Transactions of the Royal Society B: Biological Sciences.* 371(1696), 20150172. https://doi.org/10.1098/rstb.2015.0172

McFadden, D. 1974. Conditional logit analysis of qualitative choice behavior. In: *Frontiers in Economics*, P. Zarembka, eds. New York: Academic Press

Millar, D.J., & Benda, L.E., (2000). Effects of punctuated sediment supply on valley-floor landforms and sediment transport. *Geological Society of America Bulletin.* 112, 1814-1824.

Moody, J. A. & Martin, D. A. (2004) Wildfire Impacts on Reservoir Sedimentation in the Western United States. *Proceedings of the Ninth International Symposium on River Sedimentation.*

Moody, J. A. & Martin, D. A. (2009). Synthesis of sediment yields after wildland fire in different rainfall regimes in the western United States. *International Journal of Wildfire*. 18(1), 96-115.

MTBS Data Access: Fire Level Remote Data. (2017, July - last revised). MTBS Project (USDA Forest Service/U.S. Geological Survey). Available online: http://mtbs.gov/direct-download

Murphy B. P., Czuba J. A., & Belmont P. (2019). Post-wildfire sediment cascades: A modeling framework linking debris flow generation and network-scale sediment routing. *Earth Surface Processes and Landforms.* 44(11), 2126-2140.

Murphy B. P., Yocom L. L., & Belmont P. (2018). Beyond the 1984 Perspective: Narrow Focus on Modern Wildfire Trends Underestimates Future Risks to Water Security. *Earth's Future.* 6(11), 1492-1497.

Nyman P., Box W., Stout J., Sheridan G., Keesstra S., Lane,P., Langhans C. (2020) Debris-flow-dominated sediment transport through a channel network after wildfire. *Earth Surface Processes and Landforms.* 45, 1155-1167.

Overpack, J. T. & Udall, B. (2020). Climate change and the aridification of North America. *Proceedings of the National Academy of Sciences.* 117(22), 11856-11858. https://www.doi.org/10.1073/pnas.2006323117

PRISM Climate Group, Oregon State University, https://prism.oregonstate.edu

Radeloff V. C., Helmers D. P., Kramer H. A., Mockrin M. H., Alexandre P. M., Bar-Massada A., Butsic V., Hawbaker T. J., Martinuzzi S., Syphard A. D., Stewart S. I. (2018). Rapid growth of the US wildland-urban interface raises wildfire risk. *Proceedings of the National Academy of Sciences.* 155(13), 3314-3319. https://doi.org/10.1073.pnas.1718850155.

Reale J. K., Van Horn D. J., Condon K. E., Dahm C. N. (2015). The effects of catastrophic wildfire on water quality along a river continuum. *Freshwater Science*. 34(4), 1426-1442.

Reneau S. L., Katzman D., Kuyumjian G. A., Lavine A., Malmon D. V. (2007) Sediment delivery after wildfire. *Geology*. 35(2), 151- 154. https://doi.org/10.1130/G23288A.1

Rengers F. K., Bower S., Knapp A., Kean J. W., vonLembke D. W., Thomas M. A., Kostelnik J., Barnhart K. R., Bethel M., Gartner J. E., Hille M., Staley D. M.,

Anderson J. K., Roberts E. K., DeLong S. B., Lane B., Ridgway P., Murphy B. P. (2024). Evaluating post-wildfire debris-flow rainfall thresholds and volume models at the 2020 Grizzly Creek Fire in Glenwood Canyon, Colorado, USA. *Natural Hazards and Earth System Sciences.* 24 (6). 2093-2114.

Rhoades C. C., Entwistle D., Butler D. (2011). The influence of wildfire extent and severity on streamwater chemistry, sediment and temperature following the Hayman Fire, Colorado. *International Journal of Wildland Fire.* 20(3), 430.

Rickenmann, D. (1999). Empirical relationships for debris flows. *Natural Hazards.* 19, 47-77.

Riley K. (2012). A 14,000 Year Record of Wildfire and Alluvial Fan Deposition Reveals Relationships Among Fire, Climate, Vegetation, and Sediment Yields in the Middle Fork Salmon River, Idaho. *Boise State University: Boise, ID.*

Robichaud, P. (2000). Fire effects on infiltration rates after prescribed fire in Northern Rocky Mountain forests, USA. *Journal of Hydrology.* 231-232, 220-229.

Robichaud P. & Waldrop T. A. (1994). A comparison of surface runoff and sediment yields from a low- and high-severity site preparation burns. *Water Resources Bulletin.* 30 (1): 27-34.

Rowlingson, B. & Diggle, P. 1993 Splancs: spatial point pattern analysis code in S-Plus. *Computers and Geosciences*, 19, 627-655.

Rust A. J., Randall J., Todd A. S., Hogue T. S. (2019). Wildfire impacts on water quality, macroinvertebrate, and trout populations in the Upper Rio Grande. *Forest Ecology and Management.* 453, 117636.

Sanders A. M., Coble A. A., Swarz A. G., River M., James P., Warren D. R. (2022). Heat and smoke from wildfires influence water temperature and dissolved oxygen levels in headwater streams. *Freshwater Science.* 41(4), 665-679.

Santi P. M. (2014). Precision and Accuracy in Debris-Flow Volume Measurement. *Environmental & Engineering Geoscience.* 20(4), 349-359.

Shapiro S.S & Wilk M.B. (1965). An analysis of variance test for normality (complete samples). *Biometrika.* 52(3-4), 591-611. https://doi.org/10.1093/biomet/52.3-4.591.

Shields, A. (1936). Application of similarity principles and turbulence research to bed-load movement (translated version). *Caltech Library.*

Staley D. M., Negri J. A., Kean J. W., Laber J. L., Tillery A. C., Youberg A. M. (2017). Prediction of spatially explicit rainfall intensity±duration thresholds for post-fire

debris-flow generation in the western United States. *Geomorphology*. 278, 149-162.

Stringer L. C., Mirzabaev A., Benjaminsen T. A., Harris R. M. B., Jafari M., Lissner T. K., Stevens N., Tirado-von der Phalen C. (2021). Climate change impacts on water security in global drylands. One Earth. 4(6), 851-864.

U.S. Environmental Protection Agency (EPA) (2016). What climate change means for Utah (Report 430-F-16-046) [Available at https://19january2017snapshot.epa.gov/sites/production/files/201609/documents/climate-change-ut.pdf].

U.S. Global Change Research Program (USGCRP) (2018) Fourth National Climate Assessment, Washington DC. Chapter 2, 1-470. https://nca2018.globalchange.gov/chapter/2

U.S. Geological Survey (USGS) (2018). USGS Digital Elevation Model (DEM). https://apps.nationalmap.gov/services/.

U.S. Geological Survey (USGS) (2019). USGS TNM Hydrography (NHD). https://apps.nationalmap.gov/services/.

Utah Division of Water Resources (UDWR) (2021). 2021 Water Resources Plan. [Available at https://water.utah.gov/wp-content/uploads/2022/01/Water-Resources-Plan-Single-Page-Layout.pdf].

Verkaik I., Rieradevall M., Cooper S. D., Melack J. M., Dudley T. T., Prat N. (2013). Fire as a disturbance in mediterranean climate streams. Hydrobiologia. 719(1), 353-382. https://doi.org/10.1007/s10750-013-1463-3

Wall S., Murphy B. P., Belmont P., Yocom L. (2023). Predicting post-fire debris flow grain sizes and depositional volumes in the Intermountain West, United States. *Earth Surface Processes and Landforms*. 48(1), 179-197.

Wilcoxon, F. (1945). Individual Comparisons by Ranking Methods. *Biometrics Bulletin.*1(6), 80-83.

Weisberg, S. (2005). Applied linear regression (Vol. 528). *John Wiley & Sons.*

Westerling A.L., H.G. Hidalgo, D.R. Cayan, & Swetnam T.W. (2006). Warming and earlier spring increase western US forest wildfire activity. *Science*, 313, 940-943.

Wolman, M. G. (1954). A method of sampling coarse river-bed material. *American Geophysical Union.* 35(6), 951.

APPENDICES

Appendix A. Tables of all debris flow study sites and their examined remote metrics for modeling.

Table A.1. Debris flow study locations.

Site	DF ID	Fire, Year	DF Year	Long, Lat
Clay Springs 1	CS1	Clay Springs, 2012	2014	112.1649973°W 39.3565499°N
Clay Springs 2	CS2	Clay Springs, 2012	2014	112.1503388°W 39.3334051°N
Clay Springs 3	CS3	Clay Springs, 2012	2014	112.1571626°W 39.3293255°N
Clay Springs 4	CS4	Clay Springs, 2012	2014	112.2415526°W 39.4431215°N
Clay Springs 5	CS5	Clay Springs, 2012	2014	112.1580823°W 39.3534267°N
Clay Springs 6	CS6	Clay Springs, 2012	2014	112.2169795°W 39.4727540°N
Dollar Ridge 1A	DR1A	Dollar Ridge, 2018	2018	110.7842434°W 40.1218549°N
Dollar Ridge 1	DR1	Dollar Ridge, 2018	2018	110.7443828°W 40.1209189°N
Dollar Ridge 2	DR2	Dollar Ridge, 2018	2018	110.7461940°W 40.1087163°N
Dollar Ridge 3	DR3A	Dollar Ridge, 2018	2018	110.7712533°W 40.1235432°N
Dollar Ridge 4	DR4	Dollar Ridge, 2018	2018	110.7907944°W 40.1207009°N
Dollar Ridge 4A	DR4A	Dollar Ridge, 2018	2018	110.8042790°W 40.1158957°N
Dollar Ridge 5	DR5	Dollar Ridge, 2018	2018	110.8348254°W 40.1212867°N
Dollar Ridge 5A	DR5A	Dollar Ridge, 2018	2018	110.8477539°W 40.1265143°N
Pole Creek 1	PC1	Pole Creek, 2018	2019	111.5230515°W 39.9418441°N
Pole Creek 2	PC2	Pole Creek, 2018	2019	111.5209323°W 39.9403668°N
Pole Creek 3	PC3	Pole Creek, 2018	2019	111.5194444°W 39.9386945°N
Pole Creek 4	PC4	Pole Creek, 2018	2019	111.5186854°W 39.9379777°N
Pole Creek 5	PC5	Pole Creek, 2018	2019	111.5183522°W 39.9374986°N
Pole Creek 6	PC6	Pole Creek, 2018	2019	111.5170698°W 39.9352345°N
Pole Creek 7	PC7	Pole Creek, 2018	2019	111.3967406°W 39.9919036°N
Lake Fork 1	LF1	Pole Creek, 2018	2019	111.4561384°W 39.9637260°N

Table A.1. (cont.)

Lake Fork 2	LF2	Pole Creek, 2018	2019	111.4145273°W 39.9360224°N
Seeley 1	S1	Seeley, 2012	2012	111.1617234°W 39.5411264°N
Seeley 2	S2	Seeley, 2012	2012	111.1665492°W 39.5477166°N
Seeley 3	S3	Seeley, 2012	2012	111.2038681°W 39.5229984°N
Seeley 4	S4	Seeley, 2012	2012	111.1987539°W 39.5197457°N
Seeley 5	S5	Seeley, 2012	2012	111.1833178°W 39.5701072°N
Seeley 6	S6	Seeley, 2012	2012	111.2096930°W 39.5264368°N
Shingle 1	Sh1	Shingle, 2012	2013	112.6003646°W 37.4308742°N
Shingle 2	Sh2	Shingle, 2012	2013	112.6028607°W 37.4343828°N
Shingle 3	Sh3	Shingle, 2012	2015	112.6050836°W 37.4411075°N
Trail Mountain 1	TM1	Trail Mountain, 2018	2018	111.1566292°W 39.4239114°N
Trail Mountain 2	TM2	Trail Mountain, 2018	2018	111.1703243°W 39.4312605°N
Trail Mountain 3	TM3	Trail Mountain, 2018	2018	111.1730069°W 39.4343738°N
Trail Mountain 4	TM4	Trail Mountain, 2018	2018	111.1767369°W 39.4363717°N
Trail Mountain 5	TM5	Trail Mountain, 2018	2018	111.1820109°W 39.4368392°N
Fish Creek 1	FC1	Twitchell Canyon, 2010	2011	112.4534076°W 38.5014422°N
Fish Creek 2	FC2	Twitchell Canyon, 2010	2011	112.4558859°W 38.5041759°N
Fish Creek 3	FC3	Twitchell Canyon, 2010	2011	112.4560217°W 38.5048043°N
Fish Creek 4 2011	FC4_11	Twitchell Canyon, 2010	2011	112.4588018°W 38.5139838°N
Fish Creek 4 2018	FC4_18	Twitchell Canyon, 2010	2018	112.4588018°W 38.5139838°N
Fish Creek 5 2011	FC5_11	Twitchell Canyon, 2010	2011	112.4566256°W 38.5191456°N
Fish Creek 5 2014	FC5_14	Twitchell Canyon, 2010	2014	112.4566256°W 38.5191456°N
Fish Creek 5 206	FC5	Twitchell Canyon, 2010	2016	112.4566256°W 38.5191456°N
Fish Creek 7 2011	FC7_11	Twitchell Canyon, 2010	2011	112.4489614°W 38.5401822°N

Table A.1. (cont.)

Fish Creek 7 2016	FC7_11	Twitchell Canyon, 2010	2016	112.4489614°W 38.5401822°N
Shingle Creek 1	SC1	Twitchell Canyon, 2010	2011	112.4926236°W 38.5018448°N
Shingle Creek 2 2011	SC2_11	Twitchell Canyon, 2010	2011	112.4880498°W 38.5214910°N
Shingle Creek 2 2014	SC2_14	Twitchell Canyon, 2010	2014	112.4880498°W 38.5214910°N
Twitchell 1	T1	Twitchell Canyon, 2010	2014	112.4954915°W 38.3951018°N
Twitchell 2	T2	Twitchell Canyon, 2010	2014	112.4917565°W 38.3964402°N
Twitchell 3	T3	Twitchell Canyon, 2010	2014	112.4904133°W 38.3974025°N
Twitchell 4	T4	Twitchell Canyon, 2010	2014	112.4888042°W 38.3988940°N
Twitchell 5	T5	Twitchell Canyon, 2010	2014	112.4880136°W 38.3995282°N
Twitchell 6	T6	Twitchell Canyon, 2010	2014	112.4813218°W 38.3997372°N
Twitchell 7	T7	Twitchell Canyon, 2010	2014	112.4760119°W 38.3998529°N
Twitchell 8	T8	Twitchell Canyon, 2010	2014	112.4718159°W 38.3997220°N

Table A.2 Debris flow morphological characteristics measured in ArcGIS.

Site	DF Slope, %	Runout Length Center, m	Runout Length Upstream Edge, m	Runout Length, Downstream Edge, m	Confluence Angle, degrees	Splay Angle, degrees	Initial Area, m^2
CS 1	7.5	105.8	105.1	122.4		35.8	5696.0
CS 2	6.3	69.7	82.7	64.1		25.9	2921.0
CS 3	7.6	92.0	94.7	99.3		19.8	1785.0
CS 4	5.3	37.3	54.2	37.3	59.1	22.3	1193.2
CS 5	5.1	51.4	105	66.3	62.8	22.6	2198.0
CS 6	9.8	31.4	121.8	63.9	33.3	31	922.7
DR 1A	16.3	190.4	92.9	90.5	87.5	56	4509.3
DR 1	5.3	52.8	182.9	166.25	79.9	31	17614.7
DR 2	10.3	39.4	64.1	64.2	83.4	53	1314.5
DR 3A	6.5	156.4	125.3	102.5	114.3	69	15163.4
DR 4	11.1	50.2	51.2	67.9	121.8	112	3181.1
DR 4A	0.1	110.5	129.1	83.3	59.7	88	9666.1
DR 5	3.3	86.6	112	94.1	93.7	89	10556.4
DR 5A	5.2	94.0	87.3	61.1	67.2	96	7267.9
FC 1	5.2	53.2	80.3	52.6	72.6	126	5688.5
FC 2	12.4	66.2	77	107.6	76.9	78	5069.3
FC 3	7.1	36.8	52.9	34.2	108	111	1613.6
FC 4_11	7.9	43.7	53.4	58	76.5	94	2271.1
FC 4_18	7.5	30.6	52.5	55.2	80.6	78	1634.1
FC 5	7.1	91.3	107.2	100.9	80	50	8617.9
FC 5_11	5.7	82.9	105.7	94.5	113.8	83	8337.5

Table A.2. (cont.)

FC5_14	7.5	82.3	112.2	92.5	80	95	7195.7
FC7	0.1	47.1	99.8	58.8	49.5	99	4465.8
FC7_11	7.9	34.9	100.6	93.2	73.2	95	4494.1
LF1	5.4	118.2	219.5	110.8	85.3	127	19546.8
LF2	4.4	111.0	233.3	197	80.9	41	14700.7
PC1	7.0	26.5	48.3	53.1	30.8	81	1319.5
PC2	12.8	22.3	129.5	84.6	95.8	39	3663.3
PC3	16.8	45.7	73.9	56.4	83.8	44	2063.6
PC4	16.5	42.5	82.0	60.6	90.1	50	2976.3
PC5	19.2	26.5	59.0	41	75.7	40	572.3
PC6	10.5	41.9	124.8	111	77.3	48	3325.2
PC7	16.5	24.1	64	61.7	71.7	81	1424.8
S1	4.1	52.5	55.7	50.9	51.1	100	2700.7
S2	11.3	38.1	38.9	30.2	58.7	42	884.5
S3	7.4	58.3	99.5	74.6	71.8	104	4115.3
S4	9.3	39.4	48.5	46.4	70.2	113	2087.9
S5	32.3	32.7	29.2	29	95.4	57	537.4
S6	33.9	28.0	65.2	59.8	90	83	976.6
Sh1	17.9	65.6	98	97.8	55.1	37	2708.6
Sh2	8.5	105.7	207.9	170.2	22.4	53	7265.2
Sh3	7.3	80.8	116.1	155.6	28	35	8952.9
SC1	16.8	97.6	150	124.3	68.6	83	9919.2
SC2_11	0.0	18.3	24.7	14.6	51.3	120	406.0
SC2_14	0.0	22.3	32	19.5	51.3	146	701.4

Table A.2. (cont.)

TM1	8.3	64.9	90.1	58.3	47.7	56	2737.2
TM2	6.4	58.2	80.1	70.7	55.9	15.3	670.2
TM3	19.4	46.6	69.5	63.9	51.1	54.3	1170.3
TM4	13.6	41.4	64.9	53.8	84.2	28.8	384.2
TM5	22.3	52.7	119.3	48.4	71.3	35.4	1153.0
T1	27.4	71.4	188.8	168.3	109.9	77	12024.2
T2	18.3	38.2	43	32.8	74.5	70	1285.4
T3	19.3	60.6	65.3	46.6	81.2	75	2505.0
T4	15.2	58.0	85.8	47.1	81.8	49	5468.1
T5	26.2	34.9	65.7	61.8	77	62	1641.5
T6	22.2	29	56.5	56.3	75.2	51	1303.9
T7	23.9	24.8	17.3	47	100.6	40	654.4
T8	27.9	51.2	91.3	79	65.2	52	3651.2

Table A.3. Valley and river morphology.

Site	Delivery	Valley Bottom Width	Axial River Slope	River Location, Pre, m	River Location, Deposition, m	River Location, Post, m	River Lateral Shift / Valley Width
CS1	0	118.9	0.06				
CS2	1	54.6	0.04				
CS3	0	183.8	0.08				
CS4	1	71.1	0.07	46.0	46.0	46.0	0.00
CS5	1	52.1	0.14	44.9	47.1	47.3	0.05
CS6	1	79	0.04	28.2	25.3	26.7	-0.02
DR1	0	132.8	0.02	82.3	87	85.6	0.02
DR1A	1	199.2	0.01	170.5	167.5	170.5	0.00
DR2	1	51	0.02	19	39.3	41.6	0.44
DR3A	0	207	0.01	170.7	170.5	167.7	-0.01
DR4	1	59.8	0.01	42.4	42	38.2	-0.07
DR4A	1	120.8	0.01	89.8	90.6	88.1	-0.01
DR5	1	98.3	0.01	75.8	70.8	71.8	-0.04
DR5A	1	138.4	0.01	110.3	84.8	65.1	-0.33
FC1	1	55.8	0.03	44	42.3	41	-0.05
FC2	1	70.5	0.05		68.3	63.2	0.90
FC3	1	42.4	0.05		21.6	21.6	0.51
FC4_11	1	47	0.03	42.4	25.9	25.9	-0.35
FC4_18	1	47	0.04	25.9	31.9	31.9	0.13
FC5	1	91.3	0.04	82.8	85.8	85.8	0.03
FC5_11	1	91.3	0.04	64.6	68.4	79.8	0.17
FC5_14	1	91.3	0.04	68.4	79.8	82.8	0.16
FC7	1	84.6	0.04	35.5	41.1	60.4	0.29
FC7_11	1	84.6	0.04	29.7	35.5	41.1	0.13
LF1	1	136.5	0.03	113.8	113.8	114.4	0.00
LF2	1	117.6	0.03	103.8	90	97.2	-0.06
PC1	1	25.6	0.08	14.5	9.5	16	0.06
PC2	1	26.3	0.08	11.7	2	6.8	-0.19
PC3	1	62.9	0.08		27.4	27.8	0.44
PC4	1	43.9	0.08		17.7	21.4	0.49
PC5	1	33.5	0.08		22	25.8	0.77
PC6	1	41.9	0.08		34.2	31.2	0.74
PC7	1	30	0.01	8.7	2.3	1	-0.21
S1	0	97.1	0.02	72.5	66.6	67.1	-0.06
S2	1	64.1	0.02	31.9	33.4	34.4	0.04
S3	1	40.7	0.02	40.7	40.7	40.7	0.00
S4	1	27.3	0.02	11.8	12.6	7.4	-0.16

Table A.3. (cont.)

S5	0	128.5	0.02	36.6	35	34.3	-0.02
S6	1	32.8	0.02	6.9	3.6	3.2	-0.11
SC1A	1	133.9	0.04		88.6	84.8	0.63
SC2_11	1	68.1	0.05		17.9	12.7	0.19
SC2_14	1	68.1	0.05	17.9	20.8	12.7	-0.08
Sh1	0	37.3	0.05		106.5	106.5	0.35
Sh2	1	126.4	0.05		95.9	89.5	0.71
Sh3	1	94.4	0.05		82	82	0.87
T1	1	71.4	0.07	57.8	64.2	57.8	0.00
T2	1	44.8	0.07	29.8	35.8	28.4	-0.03
T3	1	63.6	0.07	38	52.2	42.6	0.07
T4	1	58	0.07	21.5	53.1	36.5	0.26
T5	1	61.8	0.07	33.3	28.5	40.4	0.11
T6	1	57.4	0.07	25	24.3	22.6	-0.04
T7	1	49.3	0.07	11.7	18.3	9.1	-0.05
T8	0	68.5	0.07	60.4	59.6	59.6	-0.01
TM1	1	69	0.07		38.3	38.3	0.56
TM2	1	67.5	0.07		54.6	54.6	0.81
TM3	1	54.1	0.07		41.1	41.1	0.76
TM4	1	46.8	0.07		39.1	39.1	0.84
TM5	0	35.8	0.07		6.8	11.7	0.33

Table A.4. Axial river plan view metrics through time.

Site	Pre-Confinement	Dep.-Confine.	Post-Confine.	Pre-Avg Riv Width, m	Dep.-Avg Riv Width, m	Post-Avg Riv Width, m	Pre-Sinuosity	Dep-Sinuosity	Post-Sinuosity
CS1									
CS2	0.15	0.2	0.13	5.2	7	4.4	1.13	1.07	1.1
CS3									
CS4	0.05	0.14	0.11	2.4	6.95	5.25	1.16	1.14	1.14
CS5	0.06	0.05	0.04	4.3	3.3	2.9	1.14	1.16	1.15
CS6	0.16	0.25	0.21	6.5	10.25	8.4	1.24	1.22	1.23
DR1	0.05	0.04	0.04	7.07	5.65	6.79	1.63	1.61	1.59
DR1A	0.04	0.05	0.05	7.41	8.65	8.45	1.16	1.12	1.11
DR2	0.12	0.13	0.16	5.62	6.35	7.58	1.3	1.23	1.25
DR3A	0.03	0.05	0.04	7.23	10.3	8.96	1.1	1.1	1.1
DR4	0.11	0.13	0.13	9.15	10.8	10.85	1.75	1.75	1.71
DR4A	0.06	0.08	0.08	7.55	11.55	10.67	1.33	1.42	1.45
DR5	0.09	0.08	0.08	8.58	7.25	7.77	1.65	1.6	1.89
DR5A	0.04	0.07	0.04	7.57	12.8	7.64	1.59	1.59	1.45
FC1	0.15	0.16	0.19	4.91	5.16	6.31	1.17	1.3	1.29
FC2		0.21	0.22		5.97	6.27		1.28	1.46
FC3		0.21	0.23		5.82	6.22		1.32	1.35
FC4_11	0.14	0.18		6.01	7.78		1.27	1.22	
FC4_18	0.16	0.16	0.12	6.86	6.9	5.23	1.23	1.23	1.24
FC5	0.23	0.09	0.09	15.12	5.85	5.85	1.14	1.18	1.18
FC5_11	0.08	0.2		5.31	13.4		1.23	1.11	
FC5_14	0.23	0.23		15.12	15.12		1.14	1.14	
FC7	0.09	0.1	0.1	7.75	8.23	8.23	1.29	1.24	1.24
FC7_11	0.07	0.07		5.92	6.31		1.24	1.3	
LF1	0.04	0.05	0.03	3.91	5.5	3.04	1.26	1.26	1.26
LF2	0.06	0.06	0.04	4.49	5.05	3.41	1.28	1.22	1.17
PBC1	0.1	0.33	0.13	1.93	6.15	2.41	1.5	1.4	1.51
PC2		0.32	0.1		7.05	2.16		1.28	1.9
PC3		0.24	0.1		6.7	2.74		1.11	1.15
PC4		0.19	0.1		6.65	3.34		1.08	1.12
PC5		0.22	0.11		6.65	3.31		1.08	1.12

Table A.4. (cont.)

PC6		0.19	0.12		6.3	3.99		1.08	1.07
PC7	0.15	0.22	0.18	5.06	7.5	6.22	1.06	1.04	1.04
S1	0.1	0.12	0.09	6.96	7.85	6.38	1.34	1.33	1.4
S2	0.1	0.13	0.12	6.6	8.05	7.6	1.38	1.22	1.19
S3	0.32	0.36	0.3	10.71	11.95	9.88	1.14	1.13	1.11
S4	0.34	0.38	0.35	10.2	11.45	10.72	1.07	1.07	1.07
S5	0.08	0.09	0.08	6.94	8.25	7.43	1.26	1.28	1.29
S6	0.37	0.42	0.38	9.63	10.9	9.89	1.16	1.17	1.17
SC1A		0.06	0.04		4.59	2.86		1.11	1.14
SC2_11		0.11			3.52			1.13	
SC2_14	0.11	0.15	0.15	3.52	4.67	4.7	1.13	1.14	1.15
Sh1		0.07	0.06		3.71	3.1		1.16	1.14
Sh2		0.04	0.04		3.02	3.02		1.2	1.36
Sh3		0.08	0.04		5.35	2.67		1.13	1.18
T1	0.09	0.08	0.07	5.15	4.85	3.79	1.14	1.18	1.17
T2	0.1	0.1	0.08	4.59	4.85	3.69	1.1	1.12	1.17
T3	0.08	0.11	0.08	4.12	5.5	3.64	1.11	1.13	1.18
T4	0.1	0.11	0.07	4.55	5.4	3.51	1.15	1.17	1.21
T5	0.1	0.12	0.08	4.56	5.65	3.84	1.15	1.15	1.22
T6	0.15	0.14	0.12	4.68	4.4	3.7	1.16	1.15	1.13
T7	0.09	0.1	0.08	4.14	4.45	3.86	1.23	1.15	1.2
T8	0.09	0.1	0.07	4.49	5	3.48	1.23	1.23	1.29
TM1		0.11	0.11		4.2	4.19		1.16	1.18
TM2		0.08	0.11		2.85	3.67		1.11	1.08
TM3		0.09	0.11		3.6	4.22		1.12	1.08
TM4		0.09	0.1		3.79	3.89		1.19	1.24
TM5		0.09	0.07		3.15	2.45		1.12	1.16

Table A.5. Recurrence interval estimates for axial river flow (m^3/s) (Kenney et al., 2007).

Site	2yr Flow	5yr Flow	10yr Flow	25yr Flow	50yr Flow	100yr Flow	200yr Flow
CS1	0.2	0.52	0.8	1.22	1.61	2.07	2.64
CS2	0.13	0.34	0.53	0.83	1.1	1.44	1.86
CS3	0.13	0.34	0.53	0.83	1.1	1.44	1.86
CS4	0.33	0.82	1.24	1.88	2.5	3.16	3.99
CS5	0.17	0.44	0.68	1.06	1.42	1.83	2.35
CS6	0.18	0.47	0.73	1.12	1.48	1.91	2.43
DR1	0.74	2.3	2.8	3.4	4.47	6.4	8
DR1A	1.33	4.05	4.8	5.73	7.32	10.44	12.86
DR2	0.7	2.21	2.64	3.26	4.23	6.08	7.59
DR3A	1.37	4.15	4.92	5.88	7.49	10.69	13.17
DR4	1.24	3.78	4.48	5.36	6.84	9.77	12.04
DR4A	1.23	3.72	4.42	5.28	6.75	9.64	11.88
DR5	0.29	0.89	1.07	1.29	1.67	2.41	3
DR5A	0.2	0.66	0.75	0.91	1.18	1.71	2.13
FC1	0.89	2.08	3.06	4.54	6.01	7.36	11.9
FC2	0.9	2.09	3.08	4.56	6.04	7.39	9.19
FC3	0.9	2.09	3.08	4.56	6.04	7.39	9.19
FC4_11	0.93	2.15	3.17	4.7	6.23	7.6	9.45
FC4_18	0.93	2.15	3.17	4.7	6.23	7.6	9.45
FC5	0.95	2.19	3.23	4.78	6.34	7.73	9.6
FC5_11	0.95	2.19	3.23	4.78	6.34	7.73	9.6
FC5_14	0.95	2.19	3.23	4.78	6.34	7.73	9.6
FC7	1.03	2.37	3.49	5.15	6.82	8.3	10.3
FC7_11	1.03	2.37	3.49	5.15	6.82	8.3	10.3
LF1	6.82	16.77	26.23	43.06	58.98	80.94	90.7
LF2	5.56	14.06	22.27	37	51.06	70.08	86.4
PC1	2.8	7.84	13.08	22.82	32.44	44.6	57.45
PC2	2.67	7.55	12.62	22.08	31.43	43.22	55.81
PC3	2.67	7.55	12.62	22.08	31.43	43.22	55.81
PC4	2.67	7.55	12.62	22.08	31.43	43.22	55.81
PC5	2.58	7.33	12.27	21.51	30.67	42.16	54.55
PC6	2.58	7.33	12.27	21.51	30.67	42.16	54.55
PC7	0.71	1.67	2.49	3.71	4.92	6.06	7.58
S1	2.1	5.61	9.06	15.27	21.23	28.87	36.12
S2	2.81	7.22	11.44	19	26.1	35.5	43.7
S3	0.48	1.58	2.82	5.21	7.67	10.45	14.21
S4	0.48	1.58	2.82	5.21	7.67	10.45	14.21
S5	2	5.41	8.76	14.81	20.63	35.18	57.98
S6	0.48	1.58	2.82	5.21	7.67	10.45	14.21

Table A.5. (cont.)

SC1A	0.2	0.52	0.81	1.25	1.67	2.14	2.74
SC2_11	0.33	0.83	1.26	1.92	2.55	3.23	4.09
SC2_14	0.33	0.83	1.26	1.92	2.55	3.23	4.09
Sh1	0.45	1.69	3.41	7.17	11.59	17.89	26.67
Sh2	0.45	1.69	3.41	7.17	11.59	17.89	26.67
Sh3	0.45	1.69	3.41	7.17	11.59	17.89	26.67
T1	0.28	0.72	1.1	1.7	2.2	2.8	3.6
T2	0.27	0.69	1.1	1.6	2.2	2.7	3.5
T3	0.27	0.69	1.1	1.6	2.2	2.7	3.5
T4	0.27	0.69	1.1	1.6	2.2	2.7	3.5
T5	0.26	0.65	1	1.5	2.1	2.6	3.3
T6	0.22	0.58	0.9	1.4	1.8	2.4	3
T7	0.2	0.55	0.86	1.3	1.8	2.3	2.9
T8	0.19	0.51	0.79	1.2	1.6	2.1	2.7
TM1	1.24	3.58	6	10.51	14.94	20.34	26.3
TM2	0.76	2.34	4.05	7.29	10.55	14.36	19.09
TM3	0.76	2.34	4.05	7.29	10.55	14.36	19.09
TM4	0.65	2.05	3.58	6.5	9.46	12.88	17.26
TM5	0.6	1.92	3.37	6.15	8.98	12.22	16.44

Table A.6. Channel fill volume for field sites.

Site	riv_l	riv_w	bfd_IMP	fill
DR2	62	2.19	0.27	36.7
DR1	0	0	0.28	0.0
DR4	106	6.05	0.32	205.2
DR5	153	6.99	0.18	192.5
FC5	173	5.14	0.28	249.0
FC7	114	4.86	0.3	166.2
LF1	353	4.92	0.32	555.8
LF2	182	2.91	0.28	148.3
PBC1	88	3.83	0.18	60.7
PC2	97	8.63	0.17	142.3
PC3	51	5.16	0.17	44.7
PC4	86	4.41	0.17	64.5
PC5	44	3.84	0.17	28.7
PC6	114	5.32	0.17	103.1
S2	35	3.29	0.26	29.9
S1	0	0	0.22	0.0
S3	173	6.13	0.09	95.4
SH1	0	0	0.09	0.0
SH2	148	1.51	0.09	20.1
TM1	98	3.74	0.15	55.0
TM2	24	1.58	0.12	4.6
TM3	39.3	2.5	0.12	11.8
TM4	16.6	2.5	0.11	4.6
TM5	0	2.5	0.1	0.0
CS1	0	0	0.11	0.0
CS2	83	0.41	0.1	3.4
CS3	0	0	0.1	0.0
CS4	170	0.27	0.15	6.9
CS5	66	1.85	0.11	13.4
CS6	0	0	0.11	0.0

Table A.7. Channel fill volume for remote sites.

Site	riv_l	riv_w	bfd_imp	fill
DR1A	7.92	143	0.33	373.7
DR3A	0	0	0.33	0.0
DR4A	8.92	142	0.32	405.3
DR5A	3.87	141	0.16	87.3
FC1	4.77	189	0.27	243.4
FC2	3.96	109	0.27	116.5
FC3	3.52	64	0.27	60.8
FC4_11	3.62	78	0.28	79.1
FC4_18	3.37	83	0.28	78.3
FC5_11	8.5	195	0.28	464.1
FC5_14	5.45	189	0.28	288.4
FC7_11	6.38	144	0.3	275.6
PC7	5.54	100	0.24	133.0
S4	4.06	103	0.09	37.6
S5	0	0	0.22	0.0
S6	5.61	64	0.09	32.3
SC1A	3.22	195	0.12	75.3
SC2_11	1.76	42	0.16	11.8
SC2_14	2.27	56	0.16	20.3
Sh3	2.91	190	0.09	49.8
T1	4.79	166	0.1	79.5
T2	2.77	43	0.1	11.9
T3	3.62	105	0.1	38.0
T4	4.2	68.7	0.1	28.9
T5	0	0	0.1	0.0
T6	3.37	70	0.1	23.6
T7	4.02	41	0.1	16.5
T8	0	0	0.1	0.0

Appendix B. Time Series Data

Table B.1. Field site area.

Site	EstInt	t_0	t_1	t_2	t_3	t_4	t_5	t_6	t_7	t_8	t_9	t_10
DR2	1314.5	1210	1202	1202	1170.2	1170.2	1085.8					
DR1	4509.3	4509.3	4509.3	4509.3	4181.2	4181.2	4181.3					
DR4	3181.1	2534.9	2348.5	2348.5	2030.8	2030.8	1733.3					
DR5	10556.4	9493.7	9412.1	9412.1	9395.5	9395.5	8825.6					
FC5	8617.9	7712.3	7712.3	7509.2	7509.2	7487.4	7164	7164	6809			
FC7	4465.8	4148.1	4148.1	4148.1	4148.1	3915.3	3896.2	3896.2	3803.2			
LF1	19546.8	17525.6	17525.6	15742.8	15742.8	15529.1						
LF2	14700.7	14174.7	14174.7	13746.2	13746.2	12481.6						
PC1	1319.5	978.8	978.8	947.3	947.3	712.5						
PC2	3663.3	2676.3	2676.3	2428.8	2428.8	2419.3						
PC3	2063.6	1685.2	1685.2	1685.5	1685.2	1635.4						
PC4	2976.3	2591	2591	2389.3	2389.3	2330.5						
PC5	572.3	403.3	403.3	352.7	352.7	283.9						
PC6	3325.2	2569	2569	2540	2540	2258.5						
S1	2700.7	2700.6	2700.6	2700.2	2700.2	2700.2	2700.2	2700.2	2700.2	2700.6	2700.6	2680.7
S2	884.5	770	770	770	770	770	748	748	748	747.8	744.8	737.2
S3	4115.3	3086.8	3086.8	2883.4	2883.4	2883.4	2717.2	2717.2	2717.2	2717.2	2658.8	2564.7
Sh1	2708.6	2708.6	2708.6	2708.6	2708.6	2708.6	2708.6	2708.6	2708.6	2708.6	2708.6	2708.6
Sh2	8952.9	8550.3	8550.3	8550.3	8550.3	8550.3	8550.3	8147.8	8147.8	8023.9	8023.9	8023.9
TM1	2737.2	2737.2	2737.2	2491	2305	2292	2143					
TM2	670.2	631.9	631.9	631.9	583.8	576.3	558					

Table B.1. (cont.)

Site	EstInt	t_0	t_1	t_2	t_3	t_4	t_5	t_6	t_7	t_8	t_9	t_10
TM3	1170.3	1170.3	1170.3	1170.3	1107.3	996.9	996.9					
TM4	384.2	384.2	384.2	384.2	384.2	265.1	265.1					
TM5	1153	1153	1153	1153	1153	1153	1153					
CS1	5696	5696	5696	5696	5696	5696	5696	5696	5696	5696	5696	
CS2	2921	2885.6	2885.6	2885.6	2885.6	2885.6	2885.6	2885.6	2885.6	2823.3	2785.166	
CS3	1785	1785	1785	1785	1785	1785	1785	1785	1785	1785	1785	
CS4	1193.2	1145.7	1145.7	1145.7	1145.7	1130.4	1081.2	1081.2	1039.6	1039.6	1021	
CS5	2198	2065.8	2065.8	2065.8	2065.8	2050.4	2024.4	2024.4	2024.4	2024.4	1985	
CS6	922.7	922.7	922.7	922.7	922.7	922.7	922.7	922.7	922.7	922.7	922.7	

Table B.2. Remote site area.

Site	EstInt	t_0	t_1	t_2	t_3	t_4	t_5	t_6	t_7	t_8	t_9	t_10
DR 1A	17614.7	16481.8	16481.8	16118.9	16118.9	16118.9						
DR 3A	15163.4	15163.4	15163.4	15163.4	15163.4	15163.4						
DR 4A	9666.144	8360.552	8180.645	8180.645	7894.333	7894.333						
DR 5A	7267.863	7267.863	6526.963	6526.963	5980.351	5980.351						
FC1	5688.5	5023.8	5023.8	5023.8	4763.54	4763.54	4763.54	4763.54	4704.27	4704.27	4061.77	4009.6
FC2	5069.307	4106.359	4106.359	4106.359	3830.129	3830.129	3830.129	3830.129	3830.129	3830.129	3828.497	3828.497
FC3	1613.6	1389	1389	1389	1293.397	1293.397	1293.397	1293.397	1293.397	1293.397	1203.182	1186.93
FC4_11	2271.084	1699.315	1699.315	1699.315	1002.658	1002.658						
FC5_11	8337.5	5739.6										
FC7_11	4494.1	3577.025	3577.025	3577.025	3449.152							
FC5_14	7195.7	5955	5955									
FC4_18	1634.113	1322.451	1322.451	1263.62	1048.817							
SC1A	9919.2	9280.1	9280.1	9280.1	8950.8	8950.8	8950.8	8950.8	8809.2	8809.2	8552.1	8480.9
SC2_14	701.4117	488.1458	488.1458	488.1458	488.1458	486.2749	486.2749	299.1024	299.1024			
PC7	1424.8	917.4	917.4	917.4	917.4							
S4	2087.922	1669.967	1669.967	1530.43	1530.43	1530.43	1530.43	1530.43	1530.43	1530.43	1530.43	
S5	537.376	537.376	537.376	537.376	537.376	537.376	537.376	537.376	537.376	537.376	537.376	
S6	976.6	616.7	616.7	520.5	520.5	520.5	455.6	455.6	455.6	455.6	429.8	
Sh3	7265.2	7132.3	7132.3	7132.3	6839.9	6373.2	6373.2	6261.8				
T1	12024.2	11128.5	11128.5	11128.5	11128.5	10691.8	10691.8	10474.4	9774			
T2	1285.411	1166.099	1166.099	1166.099	1166.099	889.812	889.812	811.1143	619.0417			
T3	2504.951	2124.294	2124.294	2124.294	2124.294	1212.548	1212.548	1162.549	985.2791			
T4	5686.5	5468.1	5468.1	5468.1	5468.1	5089.9	5089.9	4219	3956.4			

Table B.2. (cont.)

T5	1641.5	1641.5	1641.5	1641.5	1641.5	1641.5	1641.5	1641.5	1641.5			
T6	1303.9	1067.4	1067.4	1067.4	1067.4	1022.9	1022.9	1021.3	986.1			
T7	654.4	488.8	488.8	488.8	488.8	208.5	208.5	208.5	151.6			
T8	3651.2	3651.2	3651.2	3651.2	3651.2	3651.2	3651.2	3614.8	3604.7			

Table B.3. Field site tributary channel incision volume.

Site	**t_0**	**t_1**	**t_2**	**t_3**	**t_4**	**t_5**	**t_6**	**t_7**	**t_8**	**t_9**	**t_10**
DR2	0	0		0		0					
DR1	0	0		44		0					
DR4	0	0		0		0					
DR5	0	0		0		0					
FC5	20.7		25.4		0	1.8		0			
FC7	0		0		0	0		0			
LF1	96		13.1		13.1						
LF2	0		332.5		0						
PC1	0		0		0						
PC2	61.5		48.9		0.5						
PC3	7.7		0		0						
PC4	0		54.8		0						
PC5	0		23.8		0						
PC6	59.4		0		0						
S1	0		0			0		0	0	0	0
S2	0		0			0			0	0	0
S3	0		0			0				0	70.1
SH1	0		0			0	0				0
SH2	0		42.3			0	0		0		0
TM1	0	125.6	0		0	0					
TM2	0			8.1	1	0					
TM3	0			25.3	30.5	0					
TM4	0			0	88.2	0					
TM5	0			0	0	0					
CS1	0				0	0		0		0	
CS2	0				0	0		0		0	
CS3	0				0	0		0	0	0	
CS4	0				0	0		0		0	
CS5	0				0	0		0		0	
CS6	0				0	0		0		0	

Table B.4. Remote site tributary channel volume.

Site	t_0	t_1	t_2	t_3	t_4	t_5	t_6	t_7	t_8	t_9	t_10
DR1A	0.0	117.6		0.0							
DR3A	0.0	0.0		0.0							
DR4A	0.0	0.0		0.0							
DR5A	0.0	0.0		0.0							
FC1	0.0			0.0				0.0		0.0	0.0
FC2	50.8			0.0				0.0		0.0	0.0
FC3	0.0			0.0				0.0		0.0	0.0
FC4_11	23.2			18.6							
FC5_11	0.0										
FC7_11	0.0			0.0							
FC5_14	0.0										
FC4_18	15.6		38.4	0.0							
SC1A	0.0			0.0				0.0		0.0	0.0
SC2_11	0.0										
SC2_14	20.6				0.0		13.7	0.0			
PC7	7.1		13.2								
S4	0.0		0.0			0.0				0.0	
S5	0.0		0.0			0.0				0.0	
S6	0.0		0.0			0.0				0.0	
Sh3	0.0			0.0	114.3		2.8				
T1	0.0				0.0		0.0	0.0			
T2	0.0				0.0		0.0	0.0			
T3	0.0				0.0		0.0	0.0			
T4	0.0				0.0		0.0	0.0			
T5	0.0				0.0		0.0	0.0			
T6	0.0				0.0		0.0	0.0			
T7	0.0				0.0		0.0	0.0			
T8	0.0				0.0		0.0	0.0			

Table B.5. Field site axial river volume.

Site	t_0	t_1	t_2	t_3	t_4	t_5	t_6	t_7	t_8	t_9	t_10
DR2	14.1	3.1		9		25.9					
DR1	0			0		0					
DR4	98.1	35.9		82.2		87.7					
DR5	64.6	6.9		0		62.4					
FC5	176.9		0.6		21.6	24		0			
FC7	48		0		13.1	7.7		5.3			
LF1	70.1		53.9		0.3						
LF2	128.3		48.3		196.4						
PC1	69.3		8.2		98.5						
PC2	160.9		50		0						
PC3	44.7		0		0						
PC4	65.1		0		30.9						
PC5	21.4		0		22.6						
PC6	24.8		0		26.8						
S1	0		0			0			0	0	0
S2	29.9		0			32.3		0	0	23.2	0
S3	95.4		125.4			119.6				0	37.9
SH1	0		0			0	0				0
SH2	5.6		0			0	23.5		40.4		0
TM1	55	0		0	0	325.6					
TM2	18.5			4.1	8.7	0					
TM3	0			1.6	0	0					
TM4	0			0	3.3	0					
TM5	0			0	0	0					
CS1	0				0	0		0		0	
CS2	14.5				0	0		28.8		17.2	
CS3	0				0	0		0	0	0	
CS4	9.9				2.3	6.2		1.1		3.7	
CS5	23.4				2.3	6.3		0		9.7	
CS6	0				0	0		0		0	

Table B. 6. Remote sites axial river volume.

Site	t_0	t_1	t_2	t_3	t_4	t_5	t_6	t_7	t_8	t_9	t_10
DR1A	128.1	0.0		0.0							
DR3A	0.0	0.0		0.0							
DR4A	141.1	16.3		19.8							
DR5A	0.0	95.5		38.7							
FC1	88.8			26.5				124.3		46.9	8.2
FC2	64.6			40.3				13.8		6.0	7.0
FC3	42.0			35.6				3.4		2.3	0.9
FC4_11	49.1			52.6							
FC5_11	226.7										
FC7_11	110.8			28.2							
FC5_14	135.9										
FC4_18	49.0			45.7							
SC1A	87.5			38.7				25.2		48.6	
SC2_11	19.6										
SC2_14	28.4				5.1		15.9				
PC7	78.4										
S4	64.4					81.6				9.7	
S5	0.0					0.0				0.0	
S6	58.0					17.2				2.0	
Sh3	29.1			37.5	31.0		3.2				
T1	99.7				43.9		14.7	47.0			
T2	27.1				34.9		8.8	18.3			
T3	101.3				38.8		3.7	14.0			
T4	41.1				60.1		76.5	19.5			
T5	0.0				0.0		0.0	0.0			
T6	43.4				21.7		5.9	1.9			
T7	33.9				32.1		1.5	5.7			
T8	0.0				0.0		11.9	3.7			

Table B.7. Field sites low surface deflation rate volumes.

Site	t_0	t_1	t_2	t_3	t_4	t_5	t_6	t_7	t_8	t_9	t_10
DR2	0.1	0.1	0.1	0.1	0.1	0.1					
DR1	1.8	1.8	1.8	1.7	1.7	1.7					
DR4	1.8	1.6	1.6	1.4	1.4	1.2					
DR5	26.6	26.4	26.4	26.3	26.3	24.7					
FC5	0.8	0.8	0.8	0.8	0.7	0.7	0.7	0.7			
FC7	0.4	0.4	0.4	0.4	0.4	0.4	0.4	0.4			
LF1	1.8	1.8	1.6	1.6	1.6						
LF2	1.4	1.4	1.4	1.4	1.2						
PBC1	0.1	0.1	0.1	0.1	0.1						
PC2	0.3	0.3	0.2	0.2	0.2						
PC3	0.2	0.2	0.2	0.2	0.2						
PC4	0.3	0.3	0.2	0.2	0.2						
PC5	0.0	0.0	0.0	0.0	0.0						
PC6	5.1	5.1	5.1	5.1	4.5						
S2	0.1	0.1	0.1	0.1	0.1	0.1	0.1	0.1	0.1	0.1	0.1
S1	0.3	0.3	0.3	0.3	0.3	0.3	0.3	0.3	0.3	0.3	0.3
S3	0.3	0.3	0.3	0.3	0.3	0.3	0.3	0.3	0.3	0.3	0.3
Sh1	0.3	0.3	0.3	0.3	0.3	0.3	0.3	0.3	0.3	0.3	0.3
Sh2	0.9	0.9	0.9	0.9	0.9	0.9	0.8	0.8	0.8	0.8	0.8
TM1	0.3	0.3	0.2	0.2	0.2	0.2					
TM2	0.1	0.1	0.1	0.1	0.1	0.1					
TM3	0.1	0.1	0.1	0.1	0.1	0.1					
TM4	0.3	0.3	0.3	0.3	0.2	0.2					
TM5	0.1	0.1	0.1	0.1	0.1	0.1					
CS1	0.6	0.6	0.6	0.6	0.6	0.6	0.6	0.6	0.6	0.6	
CS2	0.3	0.3	0.3	0.3	0.3	0.3	0.3	0.3	0.3	0.3	
CS3	0.2	0.2	0.2	0.2	0.2	0.2	0.2	0.2	0.2	0.2	
CS4	0.1	0.1	0.1	0.1	0.1	0.1	0.1	0.1	0.1	0.1	
CS5	0.2	0.2	0.2	0.2	0.2	0.2	0.2	0.2	0.2	0.2	
CS6	0.1	0.1	0.1	0.1	0.1	0.1	0.1	0.1	0.1	0.1	

Table B.8. Field sites high surface deflation rate volumes.

Site	t_0	t_1	t_2	t_3	t_4	t_5	t_6	t_7	t_8	t_9	t_10
DR2	5.0	4.9	4.9	4.8	4.8	4.5					
DR1	22.5	22.5	22.5	20.9	20.9	20.9					
DR4	12.7	11.7	11.7	10.2	10.2	8.7					
DR5	47.5	47.1	47.1	47.0	47.0	44.1					
FC5	38.6	38.6	37.5	37.5	37.4	35.8	35.8	34.0			
FC7	20.7	20.7	20.7	20.7	19.6	19.5	19.5	19.0			
LF1	87.6	87.6	78.7	78.7	77.6						
LF2	70.9	70.9	68.7	68.7	62.4						
PC1	4.9	4.9	4.7	4.7	3.6						
PC2	13.4	13.4	12.1	12.1	12.1						
PC3	5.1	5.1	5.1	5.1	4.9						
PC4	13.0	13.0	11.9	11.9	11.7						
PC5	2.0	2.0	1.8	1.8	1.4						
PC6	12.8	12.8	12.7	12.7	11.3						
S2	3.9	3.9	3.9	3.9	3.9	3.7	3.7	3.7	3.7	3.7	3.7
S1	13.5	13.5	13.5	13.5	13.5	13.5	13.5	13.5	13.5	13.5	13.4
S3	15.4	15.4	14.4	14.4	14.4	13.6	13.6	13.6	13.6	13.3	12.8
Sh1	13.5	13.5	13.5	13.5	13.5	13.5	13.5	13.5	13.5	13.5	13.5
Sh2	42.8	42.8	42.8	42.8	42.8	42.8	40.7	40.7	40.1	40.1	40.1
TM1	10.9	10.9	10.0	9.2	9.2	8.6					
TM2	0.8	0.8	0.8	0.7	0.7	0.7					
TM3	5.9	5.9	5.9	5.5	5.0	5.0					
TM4	1.9	1.9	1.9	1.9	1.3	1.3					
TM5	5.8	5.8	5.8	5.8	5.8	5.8					
CS1	17.1	17.1	17.1	17.1	17.1	17.1	17.1	17.1	17.1	17.1	
CS2	4.3	4.3	4.3	4.3	4.3	4.3	4.3	4.3	4.2	4.2	
CS3	2.7	2.7	2.7	2.7	2.7	2.7	2.7	2.7	2.7	2.7	
CS4	4.9	4.9	4.9	4.9	4.9	4.6	4.6	4.5	4.5	4.4	
CS5	6.2	6.2	6.2	6.2	6.2	6.1	6.1	6.1	6.1	6.0	
CS6	4.6	4.6	4.6	4.6	4.6	4.6	4.6	4.6	4.6	4.6	

Table B.9. Remote sites low surface deflation rate volumes

.Site	EstInt	t_0	t_1	t_2	t_3	t_4	t_5	t_6	t_7	t_8	t_9	t_10
DR1A	17614.7	1.6	1.6	1.6	1.6	1.6						
DR3A	15163.4	1.5	1.5	1.5	1.5	1.5						
DR4A	9666.144	0.8	0.8	0.8	0.8	0.8						
DR5A	7267.863	0.7	0.7	0.7	0.6	0.6						
FC1	5688.5	0.5	0.5	0.5	0.5	0.5	0.5	0.5	0.5	0.5	0.4	0.4
FC2	5069.307	0.4	0.4	0.4	0.4	0.4	0.4	0.4	0.4	0.4	0.4	0.4
FC3	1613.6	0.1	0.1	0.1	0.1	0.1	0.1	0.1	0.1	0.1	0.1	0.1
FC4_11	2271.084	0.2	0.2	0.2	0.1	0.1						
FC5_11	8337.5	0.6										
FC7_11	4494.1	0.4	0.4	0.4	0.3							
FC5_14	7195.7	0.6	0.6									
FC4_18	1634.113	0.1	0.1	0.1	0.1							
SC1A	9919.2	0.9	0.9	0.9	0.9	0.9	0.9	0.9	0.9	0.9	0.9	0.8
SC2_11	405.9878	0.0	0.0	0.0								
SC2_14	701.4117	0.0	0.0	0.0	0.0	0.0	0.0	0.0	0.0			
PC7	1424.8	0.1	0.1	0.1	0.1							
S4	2087.922	0.2	0.2	0.2	0.2	0.2	0.2	0.2	0.2	0.2	0.2	
S5	537.376	0.1	0.1	0.1	0.1	0.1	0.1	0.1	0.1	0.1	0.1	
S6	976.6	0.1	0.1	0.1	0.1	0.1	0.0	0.0	0.0	0.0	0.0	
Sh3	7265.2	0.7	0.7	0.7	0.7	0.6	0.6	0.6				
T1	12024.2	1.1	1.1	1.1	1.1	1.1	1.1	1.0	1.0			
T2	1285.411	0.1	0.1	0.1	0.1	0.1	0.1	0.1	0.1			
T3	2504.951	0.2	0.2	0.2	0.2	0.1	0.1	0.1	0.1			
T4	5686.5	0.5	0.5	0.5	0.5	0.5	0.5	0.4	0.4			
T5	1641.5	0.2	0.2	0.2	0.2	0.2	0.2	0.2	0.2			
T6	1303.9	0.1	0.1	0.1	0.1	0.1	0.1	0.1	0.1			
T7	654.4	0.0	0.0	0.0	0.0	0.0	0.0	0.0	0.0			
T8	3651.2	0.4	0.4	0.4	0.4	0.4	0.4	0.4	0.4			

Table B.10. Remote sites high surface deflation rate volumes.

Site	t_0	t_1	t_2	t_3	t_4	t_5	t_6	t_7	t_8	t_9	t_10
DR1A	82.4	82.4	80.6	80.6	80.6						
DR3A	75.8	75.8	75.8	75.8	75.8						
DR4A	41.8	40.9	40.9	39.5	39.5						
DR5A	36.3	32.6	32.6	29.9	29.9						
FC1	25.1	25.1	25.1	23.8	23.8	23.8	23.8	23.5	23.5	20.3	20.0
FC2	20.5	20.5	20.5	19.2	19.2	19.2	19.2	19.2	19.2	19.1	19.1
FC3	6.9	6.9	6.9	6.5	6.5	6.5	6.5	6.5	6.5	6.0	5.9
FC4_11	8.5	8.5	8.5	5.0	5.0						
FC5_11	28.7										
FC7_11	17.9	17.9	17.9	17.2							
FC5_14	29.8	29.8									
FC4_18	6.6	6.6	6.3	5.2							
SC1A	2.8	2.8	2.8	2.7	2.7	2.7	2.7	2.6	2.6	2.6	2.5
SC2_11	1.5	1.5	1.5								
SC2_14	2.4	2.4	2.4	2.4	2.4	2.4	1.5	1.5			
PC7	4.6	4.6	4.6	4.6							
S4	8.3	8.3	7.7	7.7	7.7	7.7	7.7	7.7	7.7	7.7	
S5	2.7	2.7	2.7	2.7	2.7	2.7	2.7	2.7	2.7	2.7	
S6	3.1	3.1	2.6	2.6	2.6	2.3	2.3	2.3	2.3	2.1	
Sh3	35.7	35.7	35.7	34.2	31.9	31.9	31.3				
T1	55.6	55.6	55.6	55.6	53.5	53.5	52.4	48.9			
T2	5.8	5.8	5.8	5.8	4.4	4.4	4.1	3.1			
T3	10.6	10.6	10.6	10.6	6.1	6.1	5.8	4.9			
T4	27.3	27.3	27.3	27.3	25.4	25.4	21.1	19.8			
T5	8.2	8.2	8.2	8.2	8.2	8.2	8.2	8.2			
T6	5.3	5.3	5.3	5.3	5.1	5.1	5.1	4.9			
T7	2.4	2.4	2.4	2.4	1.0	1.0	1.0	0.8			
T8	18.3	18.3	18.3	18.3	18.3	18.3	18.1	18.0			

Table B.11. Field sites median volume remaining.

Site	EstInt	t_0	t_1	t_2	t_3	t_4	t_5	t_6	t_7	t_8	t_9	t_10
DR2	203.7	150.4	144.7	142.2	130.8	128.3	105.7					
DR1	636.7	624.5	612.3	600.2	544.9	533.6	519.4					
DR4	1208.7	898.2	855.6	848.9	760.9	755.1	570.6					
DR5	1596.5	1302.4	1258.8	1222.1	1185.4	1148.8	959.8					
FC5	1998.2	1531.9	1512.3	1467.1	1448.0	1407.3	1364.5	1333.3	1323.4			
FC7	894.0	669.2	658.6	648.1	637.5	614.4	594.0	580.2	597.8			
LF1	11542.3	10775.7	10731.0	10623.9	10583.7	10002.7						
LF2	5962.7	5650.0	5613.8	5198.0	5162.9	5273.2						
PC1	373.2	240.7	238.2	227.6	225.2	126.4						
PC2	878.4	506.9	500.1	395.0	388.8	400.3						
PC3	269.7	214.7	212.1	209.5	206.9	217.7						
PC4	526.0	389.8	383.2	322.3	316.2	278.9						
PC5	204.1	153.0	151.9	127.2	126.3	112.3						
PC6	664.0	467.7	458.7	449.8	440.9	360.2						
S2	296.2	264.3	262.4	260.4	258.4	256.5	254.6	252.7	250.8	248.9	247.0	210.8
S1	627.0	590.2	617.3	612.4	607.5	602.7	597.8	592.9	588.1	583.2	578.4	573.5
S3	1216.5	1017.8	1010.0	877.2	869.9	862.5	736.0	729.0	722.1	715.2	708.4	748.1
Sh1	1363.1	1356.2	1352.8	1347.7	1342.5	1337.4	1332.2	1327.1	1321.9	1316.8	1311.6	1306.5
Sh2	1963.1	1915.6	1893.8	1829.7	1807.9	1786.1	1764.3	1720.0	1699.2	1638.4	1617.9	1684.0
TM1	2150.6	2035.0	1903.8	1898.7	1893.9	1889.2	1746.3					
TM2	120.6	97.1	96.7	96.3	83.7	73.6	83.3					
TM3	357.2	354.2	351.2	348.2	318.5	285.5	280.3					
TM4	266.1	265.0	263.9	262.8	261.6	169.4	146.4					

Table B.11. (cont.)

TM5	543.8	540.1	538.0	535.0	532.1	529.1	526.2					
CS1	793.1	784.3	775.4	766.6	757.8	748.9	740.1	731.3	722.5	713.6	704.8	
CS2	559.7	539.5	537.2	534.9	532.6	530.3	527.9	525.6	494.5	492.3	506.4	
CS3	164.6	163.2	161.7	160.3	158.9	157.4	156.0	154.6	153.2	151.7	150.3	
CS4	524.8	505.5	503.0	500.4	497.9	493.1	484.6	482.2	478.8	476.5	494.7	
CS5	650.1	610.1	606.9	603.7	600.5	595.0	585.6	582.4	579.3	576.2	583.5	
CS6	126.5	124.2	121.8	119.5	117.1	114.8	112.4	110.1	107.7	105.4	103.0	

Table B.12. Remote sites median volume remaining.

Site	**EstInt**	**t_0**	**t_1**	**t_2**	**t_3**	**t_4**	**t_5**	**t_6**	**t_7**	**t_8**	**t_9**	**t_10**
DR1A	2866.6	2366.9	2214.0	2172.9	2131.8	2090.7						
DR3A	2211.2	2172.5	2133.9	2095.2	2056.5	2017.9						
DR4A	1947.7	1429.3	1398.8	1377.9	1346.2	1326.1						
DR5A	1315.1	1209.3	1128.4	1111.8	1057.8	1042.6						
FC1	1252.7	936.3	923.5	910.7	882.4	870.2	858.1	845.9	752.2	740.2	702.1	687.1
FC2	1036.9	816.6	806.1	795.6	760.8	751.1	741.3	731.5	713.4	703.6	690.2	676.3
FC3	429.2	334.5	331.0	327.5	301.3	298.0	294.7	291.4	286.0	282.7	278.3	274.7
FC4_11	563.2	422.4	418.1	413.7	360.2	357.7						
FC5_11	1834.4	1214.2										
FC7_11	1111.4	753.1	744.0	734.8	709.1							
FC5_14	1506.4	1114.1	1099.0									
FC4_18	450.4	318.8	315.4	275.8	244.3							
SC1A	1650	1513.5	1511.7	1509.8	1484.5	1482.7	1480.9	1479.1	1462.4	1460.6	1430.6	1428.9

Table B.12. (cont.)

SC2_11	134	106.3	105.5	104.7								
SC2_14	209.5	146.9	145.6	144.4	143.2	138.4	137.2	112.6	111.9			
PC7	466.4	270.5	268.1	253.0	250.7							
S4	490.3	403.6	399.3	395.4	391.5	387.6	333.9	330.0	326.1	322.2	312.6	
S5	152.8	151.4	150.1	148.7	147.3	147.3	145.9	144.5	143.2	141.8	140.4	
S6	278.8	204.2	202.6	201.3	200.0	199.9	187.8	186.7	185.5	184.3	182.0	
Sh3	1277.2	1187.5	1169.3	1151.1	1109.2	1089.2	1073.0	1052.5				
T1	1916.2	1741.5	1713.1	1684.8	1656.4	1628.9	1601.7	1566.2	1514.0			
T2	319	283.8	280.8	277.9	274.9	251.8	249.6	241.9	228.9			
T3	561.7	450.5	445.1	439.7	434.2	410.8	407.7	402.5	391.8			
T4	1037.9	965.3	951.4	937.4	923.5	910.6	897.6	839.9	818.3			
T5	373.4	369.2	365.0	360.8	356.7	356.5	352.3	348.1	343.9			
T6	334.2	276.6	273.9	271.1	268.4	254.3	251.7	245.4	241.6			
T7	195.4	152.7	151.5	150.2	149.0	128.1	127.5	126.1	122.1			
T8	707.9	698.6	689.3	680.0	670.7	670.3	661.0	642.1	630.2			

Appendix C. Exponential Decay Values

Table C.1. Exponential decay values.

Site	r	c
DR2	0.627336	26.17178
DR1	0.183147	1.912211
DR4	0.580164	25.69175
DR5	0.553267	18.42338
FC5	0.730915	23.33361
FC7	0.760592	25.14392
LF1	0.588627	6.641275
LF2	0.306889	5.24493
PBC1	0.658343	35.49699
PC2	0.713695	42.29617
PC3	0.871556	20.39469
PC4	0.544524	25.89124
PC5	0.551871	25.05919
PC6	0.72293	29.56214
S2	0.638057	10.75743
S1	0.615358	5.820073
S3	0.402865	16.33442
Sh1	0.069294	0.488298
Sh2	0.09422	2.420465
TM1	0.257982	5.3748
TM2	0.579289	19.46168
TM3	0.43491	0.835461
TM4	0.74587	0.418707
TM5	0.102831	0.6735
CS1	0.29362	1.015784
CS2	0.412884	3.611108
CS3	0.29362	0.81472
CS4	0.482861	3.678752
CS5	0.609084	6.157681
CS6	0.29362	1.591147
DR1A	0.59533	17.43219
DR3A	0.306078	1.748674
DR4A	0.798548	26.61601
DR5A	0.287948	8.047529
FC1	0.675516	25.2539
FC2	0.688284	21.2471
FC3	0.665593	22.05385
FC4_11	0.688057	25.00114
FC5_11		33.80805

Table C.1 (cont.)

FC7_11	0.821934	32.2398
FC5_14	0.633275	26.03949
FC4_18	0.606777	29.22051
SC1A	0.7262	8.270105
SC2_11	0.78431	20.66727
SC2_14	0.760094	29.88347
PC7	0.820591	42.00663
S4	0.570507	17.68278
S5	0.029545	0.896799
S6	0.821446	26.76438
Sh3	0.410304	7.022668
T1	0.508224	9.11584
T2	0.470607	11.03101
T3	0.715687	19.79815
T4	0.400839	6.994226
T5	0.042138	1.121003
T6	0.689222	17.23858
T7	0.64617	21.8394
T8	0.007936	1.315237

Appendix D. Field Data

Table D.1. Channel bed GSD, 2023 (mm).

Site	d16_ch	d50_ch	d84_ch
PC1	13.5	36	106.9
PC6	11	41.8	203.7
LF1	17.6	78.2	243
LF2	17.9	59.6	250.2
DR1	3	19.3	117.1
DR2	4	23.9	77
DR4	14.8	86.8	250
DR5	6.5	30.4	99.5
Sh1	8.5	27	72
Sh2	5.6	33.2	99.5
S1	6.8	56	124.8
S2	1.4	2.2	22.6
S3	7.6	41.5	124.5
S6	5.6	43.4	119.6
TM1_Aug	4.9	19.1	58.6
TM1_Oct	7.2	31.3	111.1
TM3	10.6	26.9	84.8
TM4	9	41.8	120.4
TM5	9.5	30.5	86.8
FC5	12.7	38.5	90
FC7	13.4	41.1	112.8
CS2	3.1	7.6	25
CS4	4.1	15.2	61.3
CS5	1.9	11.8	38.5
CS6	6.7	16.4	32

Table D. 2. Debris flow surface GSD of 2023 field survey (mm).

Site	d16	d50	d84
PC1	11.3	28.5	54.9
PC2	2	16.5	85.7
PC6	10.2	32.4	88.1
LF1	5.6	32	104.8
LF2	9.4	25.4	71.4
DR1	15.3	41.5	123.5
DR2	7.6	23.2	48.4
DR4	6.6	16.6	50.9
DR5	12.5	47	121.4
Sh1	10.7	36.5	85.7
Sh2	7.5	24.8	69.2
S1	12.4	67.9	147.7
S2	9.2	38.8	117.9
S3	7	35.8	104.1
S5	9.2	35.4	109
S6	13.2	51.6	128
TM1_Aug	9.5	36.9	98.9
TM1_Oct	1.6	18.6	62.7
TM2	2.2	23.6	66.2
TM3	5	23.6	93.5
TM4	8.6	29.6	77.9
TM5	2.1	19	64
FC5	11.2	26.7	75.6
FC7	13.2	35.8	109
CS1	9.2	31.2	82.7
CS2	6.4	41.6	81.3
CS3	9.4	34.4	66.6
CS4	4.5	40.9	107.3
CS5	8.6	49.8	100.1
CS6	16	38.7	82.8

Table D.3.1. Debris flow GSD from previous work. (2020 field survey).

Site	Source	d16 (mm)	d50 (mm)	d84 (mm)
PC1	Wall et al., 2023	9.6	18.2	30.3
LF1	Wall et al., 2023	2.2	21.3	52.4
DR1	Wall et al., 2023	19.2	32.2	55.8
DR4	Wall et al., 2023	10.1	19.3	36.2
DR5	Wall et al., 2023	10.3	29.1	61.6
Sh1	Wall et al., 2023	11.3	26.4	50.4
S1	Wall et al., 2023	26.4	62	119.3
TM1	Wall et al., 2023	1.3	4.2	48.2
CS1	Wall et al., 2023	23.1	50.7	83.7
CS2	Wall et al., 2023	17	26.4	42.9

Table D.3.2 Debris flow GSD from previous work (2017 field survey).

Site	Size bin (mm)	perc_finer	Source	Interpolated Values	Size (mm)
FC5_16	>180	100.0	Murphy et al., 2019	D16	4.7
	96	88.8		D50	21.2
	43.2	71.2		D84	81.6
	15.2	44.2			
	5	16.7			
	2	10.4			
FC7_16	>180	100	Murphy et al., 2019	D16	3.2
	64-128	100		D50	13.1
	22.4-64	74		D84	57.4
	8-22.4	37			
	2.0-8.0	11			
	<2	0			

Table D. 4 Channel hydrologic data.

Site	Width	Dep	Area	Wet. Perm	Hyd. R	Slope	n	Qbf	Str. Pwr	Unit Str.Pwr	tau_o	tau_c
TM1	9.6	0.32	4.46	10.14	0.44	0.006	0.03	6.6	381.0	39.7	25.4	24.0
TM3	1.7	0.46	0.85	2.68	0.32	0.054	0.035	2.6	1394.8	819.8	169.9	
TM4	4.33	0.51	1.99	4.8	0.41	0.075	0.05	6.1	4484.7	1034.6	303.5	
TM5	2.87	0.63	1.86	3.83	0.49	0.076	0.05	6.3	4705.9	1640.9	364.2	
CS2	6.51	0.5	3.05	7.03	0.43	0.044	0.03	12.2	5194.1	798.1	183.7	27.0
CS4	7.65	1.13	7.97	8.97	0.43	0.029	0.035	22.3	6349.5	830.1	122.7	26.6
Sh1	7.65	1.13	7.97	8.97	0.43	0.029	0.035	22.3	6349.5	830.1	122.7	9.9
Sh2	3.06	0.45	1.27	3.73	0.34	0.038	0.045	2.7	1016.1	331.9	127.9	7.7
FC5	9.8	1.08	10.76	11.98	0.9	0.002	0.04	11.9	266.6	27.2	20.1	17.4
FC7	17.04	0.95	14.86	18.16	0.82	0.010	0.045	29.6	3042.7	178.5	84.4	23.3
SH1	7.56	1.66	11.75	10.08	1.17	0.035	0.04	61.3	21267.6	2813.5	406.6	23.7
SH2	12.24	0.72	8.78	13.19	0.67	0.039	0.035	37.9	14548.3	1188.8	257.6	16.1
S1	11.8	0.31	4.29	11.89	0.36	0.017	0.04	7.2	1228.6	104.1	61.6	44.1
S2	13.2	0.54	5.7	13.92	0.41	0.020	0.08	5.6	1088.6	82.5	80.4	25.2
DR1	3.04	0.42	1.33	3.79	0.35	0.010	0.04	1.7	167.0	54.9	35.0	27.0
DR2	13.55	1.18	16.02	14.91	1.07	0.013	0.05	38.9	5117.1	377.7	140.8	15.5
DR4	20.58	0.51	11.76	20.99	0.56	0.009	0.07	10.8	937.0	45.5	48.8	12.5
DR5	20.32	1.04	21.78	21.34	1.02	0.012	0.05	49.1	5948.0	292.7	123.7	30.6
PBC1	10.7	1.04	11.95	13.02	0.92	0.050	0.05	50.3	24431.0	2282.4	447.4	11.8
PC2	12.05	1.53	17.64	14.72	1.2	0.048	0.04	108.6	50672.5	4204.4	560.6	10.7
PC3	2.76	0.43	1.34	3.5	0.38	0.036	0.04	3.3	1170.5	423.5	133.1	
PC4	1.85	0.45	0.89	2.59	0.35	0.036	0.04	2.1	727.3	393.8	122.6	
PC5	3.03	0.26	1.01	3.33	0.3	0.058	0.04	2.7	1555.9	513.9	171.3	

Table D.4. (cont.)

PC 6	4.51	5.31	30.13	17.4	1.73	0.071	0.05	230.8	15972 9.3	35452.1	119 8.3	21.1
LF 1	7.54	2.43	20.61	11.91	1.73	0.023	0.04	111.4	24571.9	3260.0	382.0	13.8

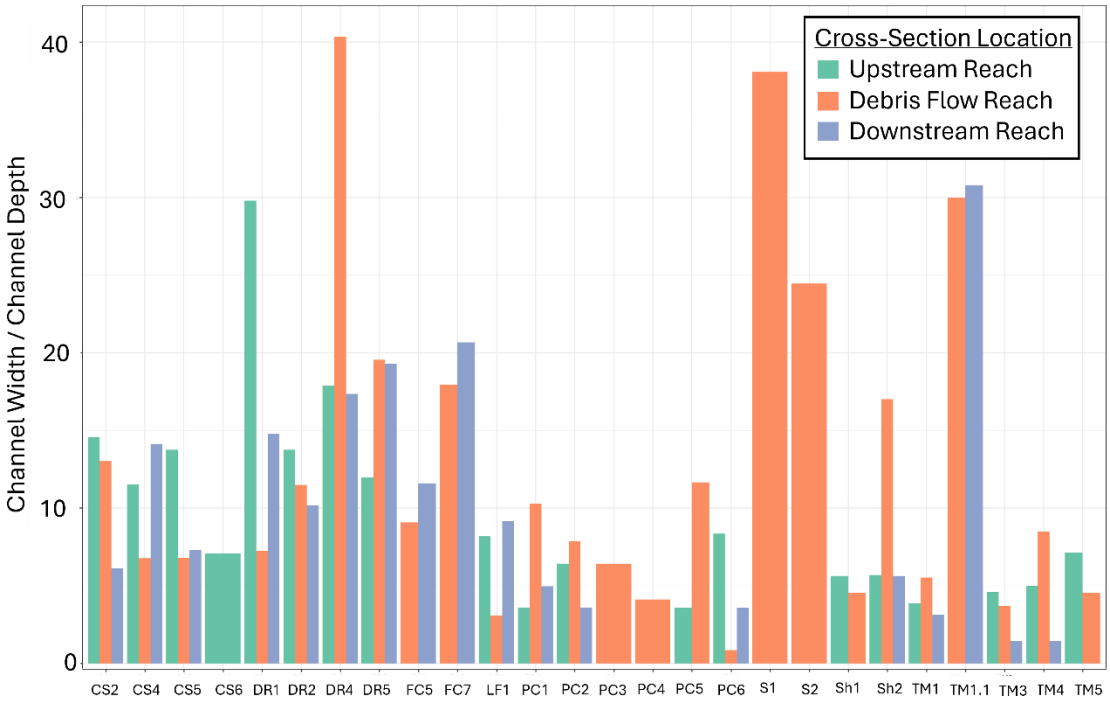

Figure D.1. Axial channel width to depth ratios at field surveyed sites at the identified locations.

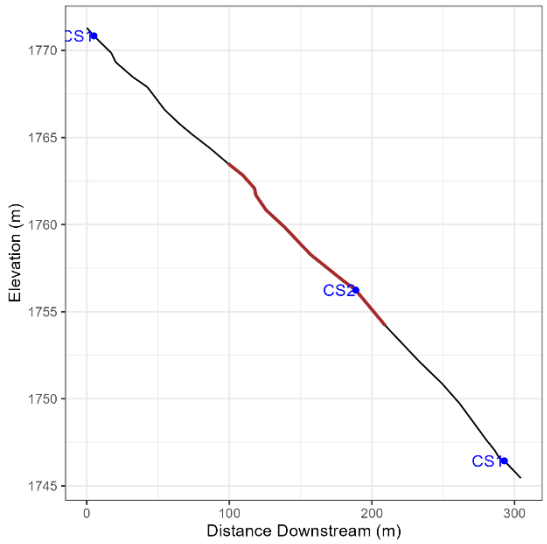

CS2

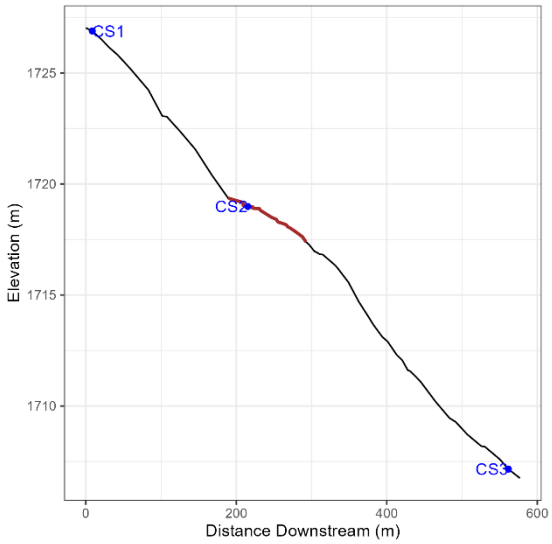

CS4

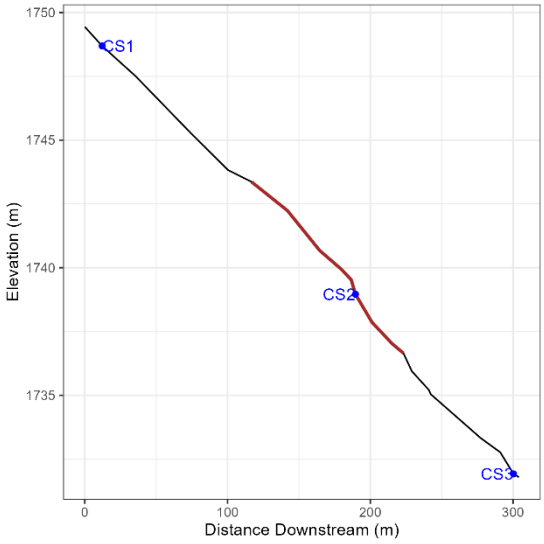

CS5

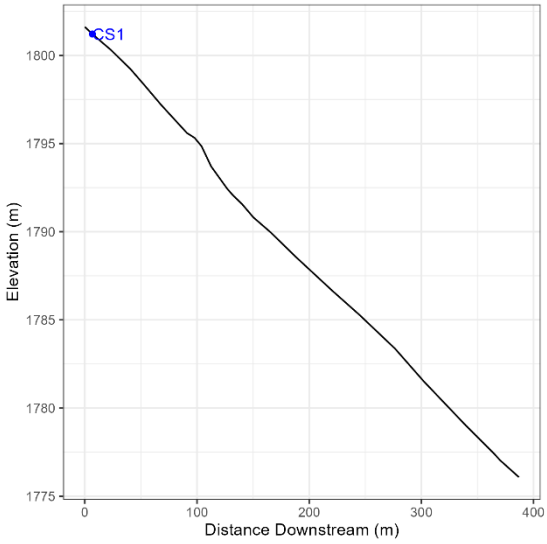

CS6

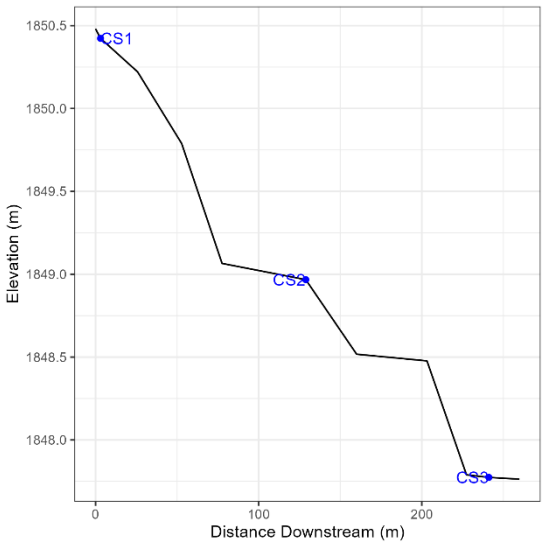

DR1

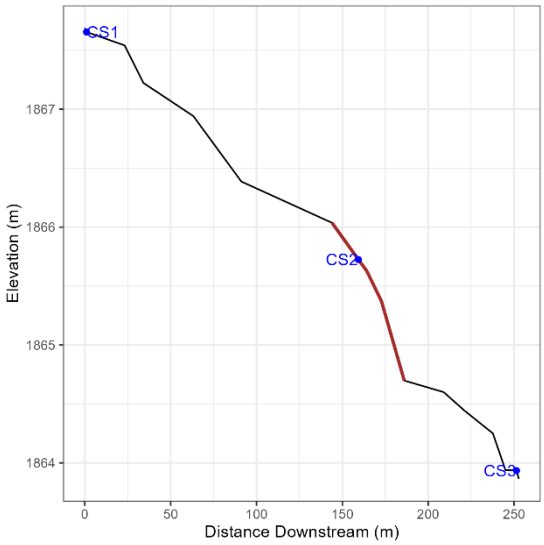

DR2

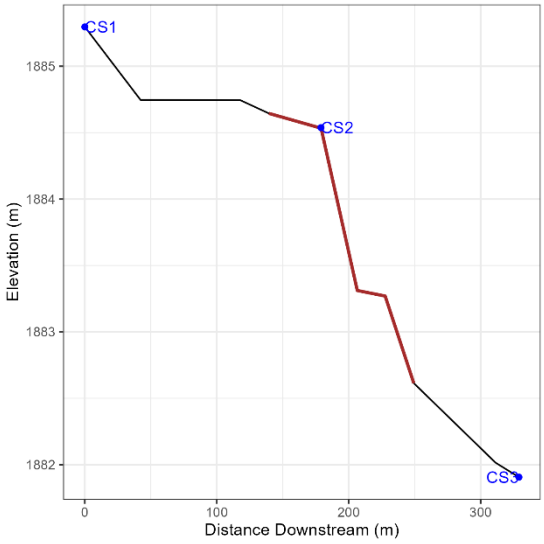

DR4

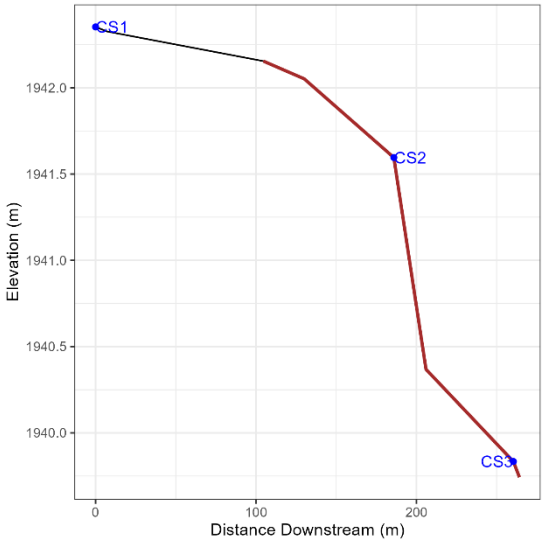

DR5

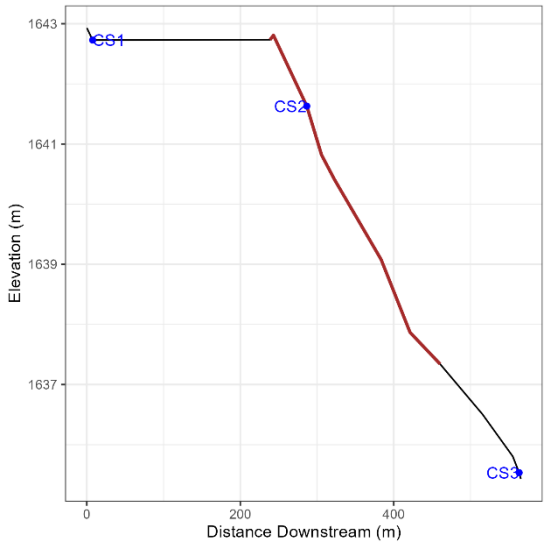

LF1

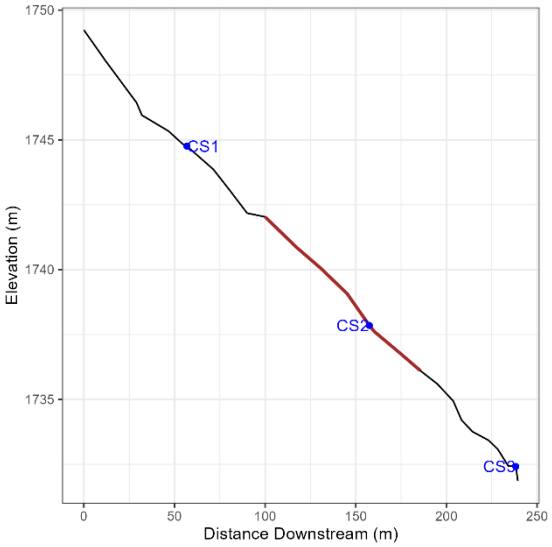

PC1

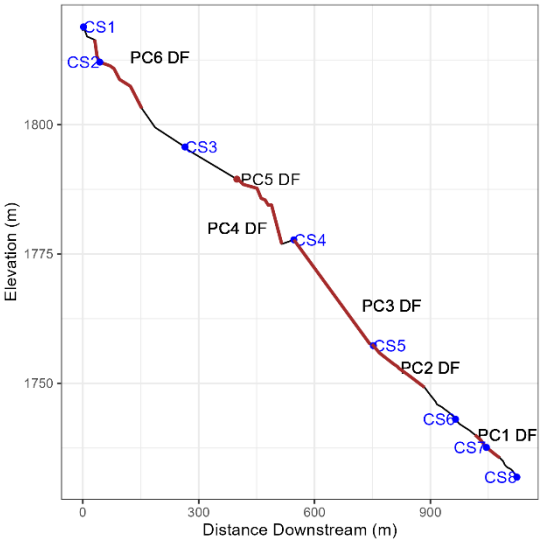

PC6 to PC1

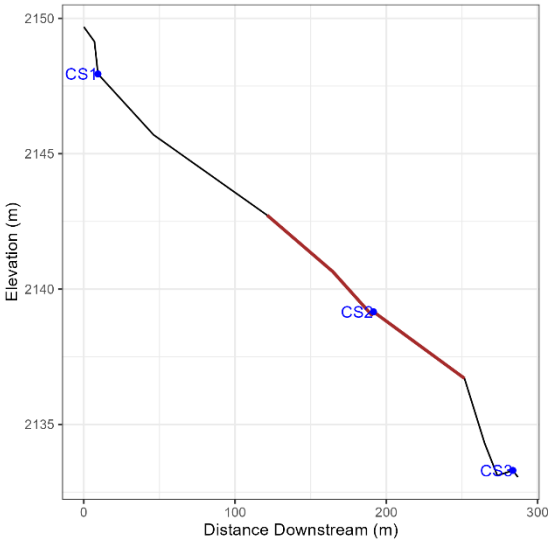

Sh2

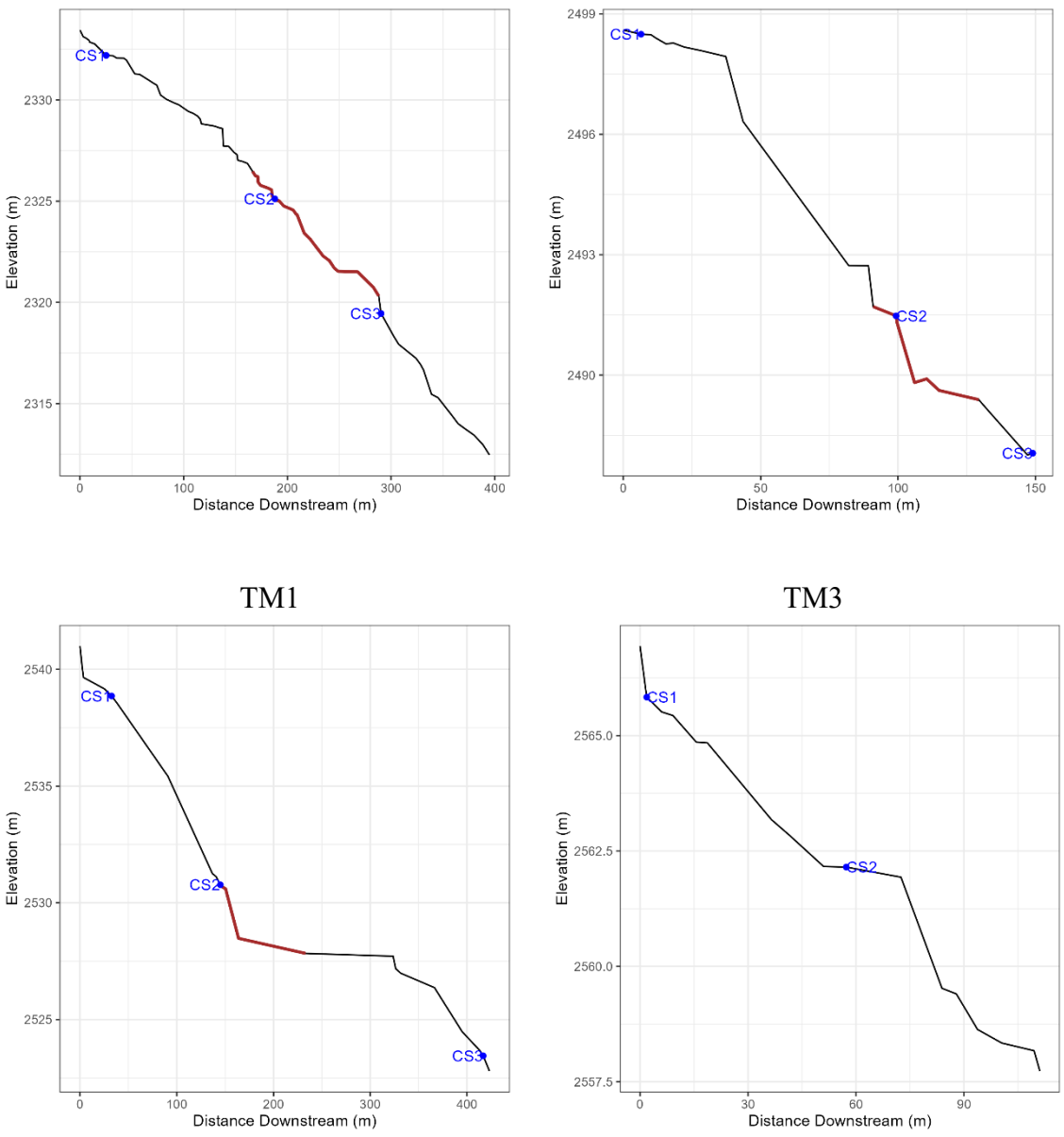

Figure D.2. Long profiles for surveyed field sites during summer 2023. Areas with a brown line represent the approximate location where the debris flow toe is crossing the axial river. The blue dots represent the approximate locations of cross-sections, labeled from upstream to downstream.

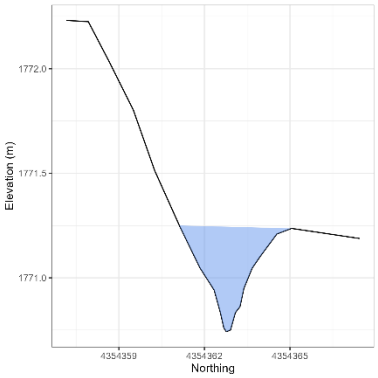

CS2 up

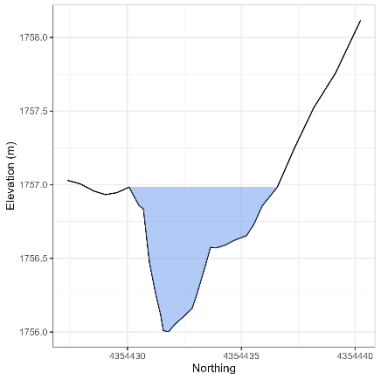

CS2 center

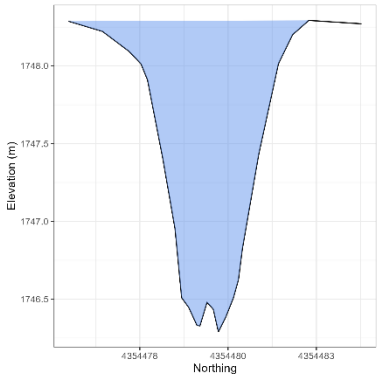

CS2 down

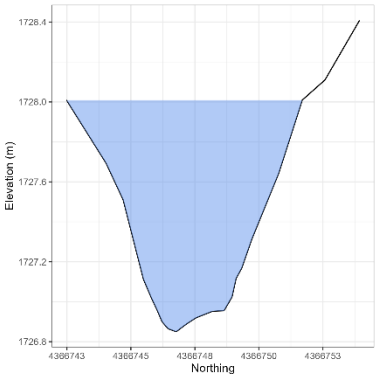

CS4 up

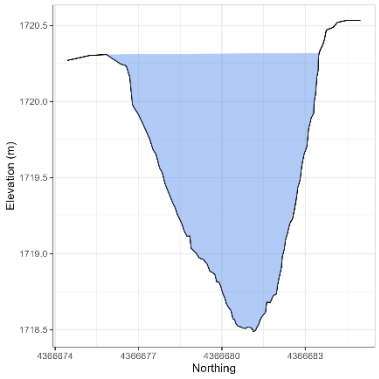

CS4 center

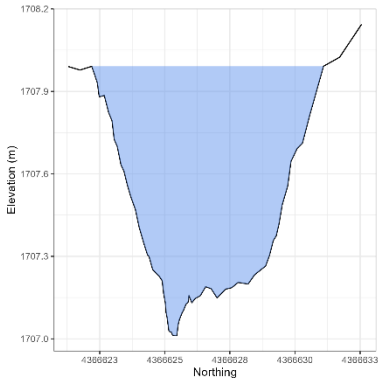

CS4 down

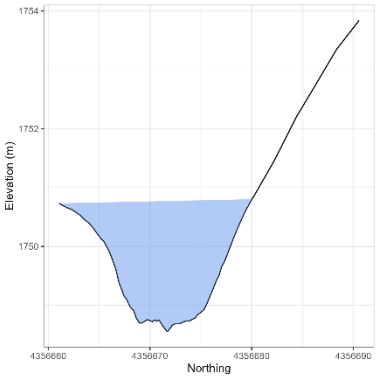

CS5 up

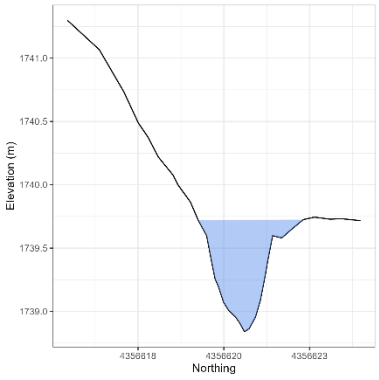

CS5 center

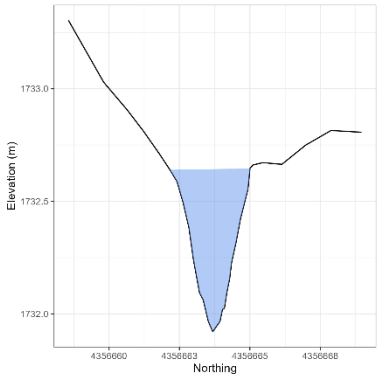

CS5 down

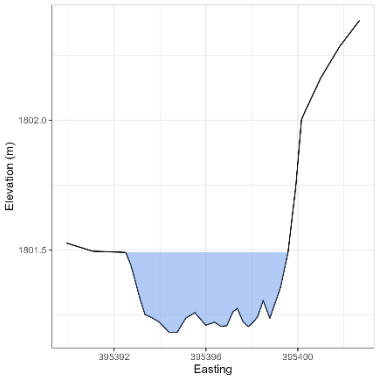

CS6 up

omit, road

CS6 center

omit, road

CS6 down

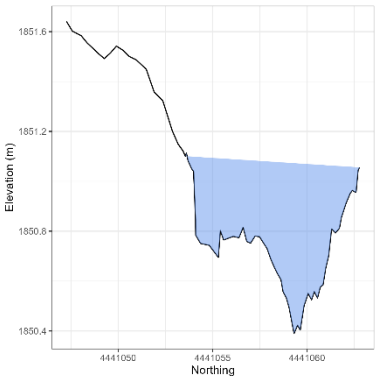

DR1 up

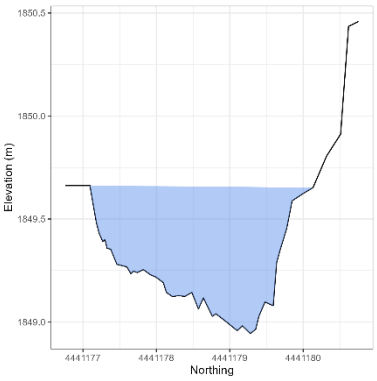

DR1 center

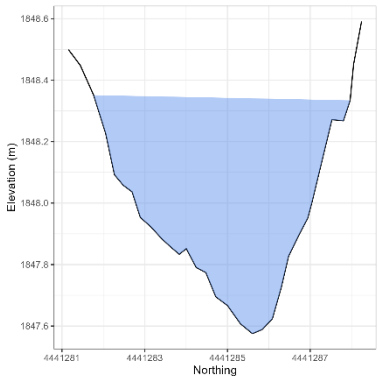

DR1 down

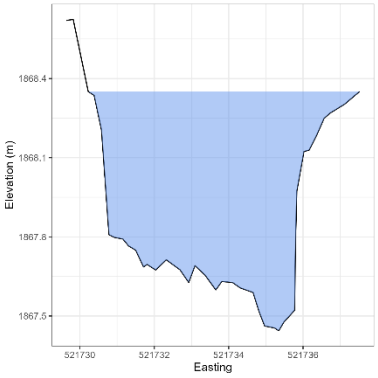

DR2 up

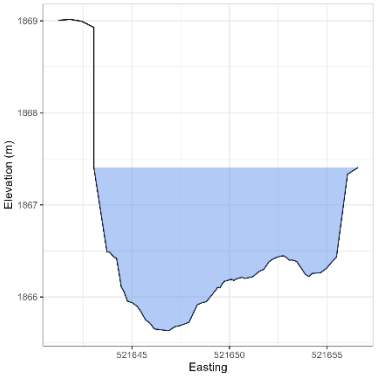

DR2 center

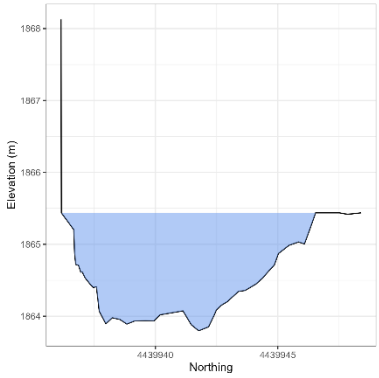

DR2 down

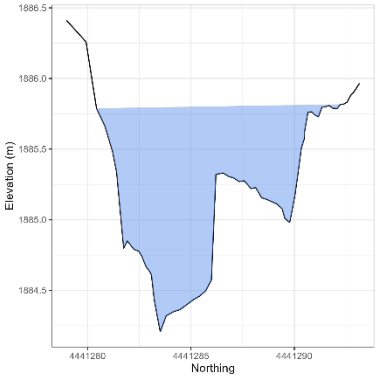

DR4 up

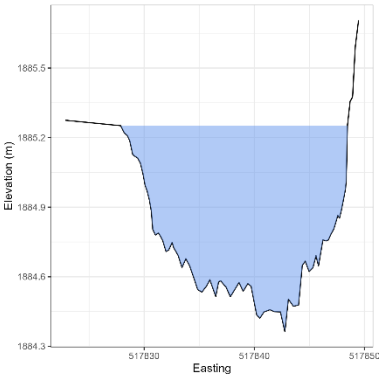

DR4 center

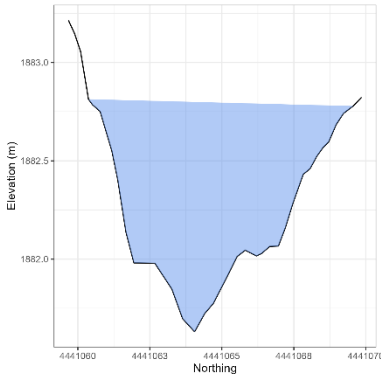

DR4 down

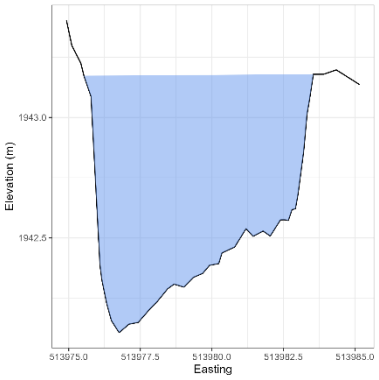

DR5 up

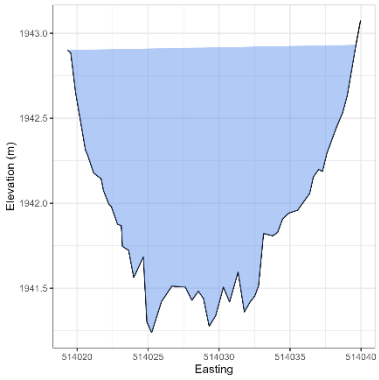

DR5 center

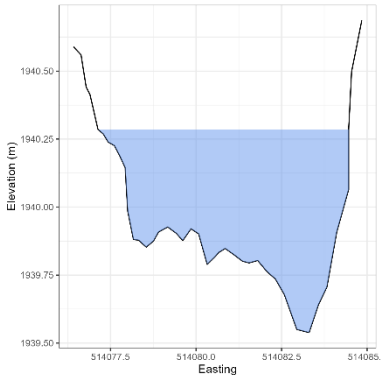

DR5 down

omit, bad RTK-GPS

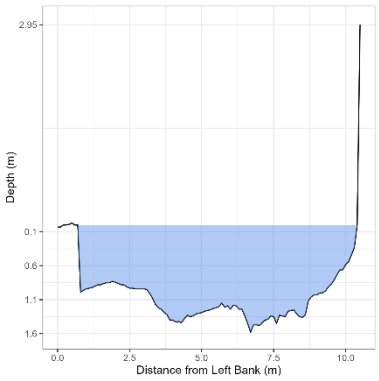

FC5 center (waded)

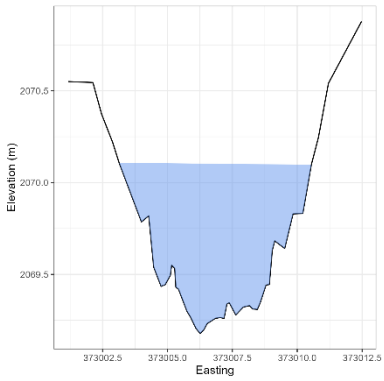

FC5 down

omit, bad RTK-GPS

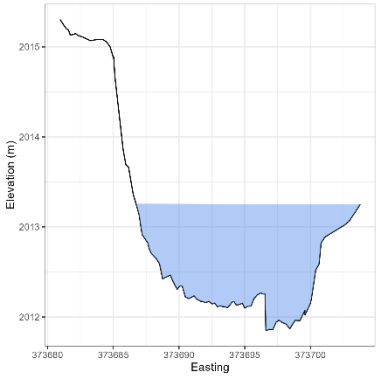

FC7 center

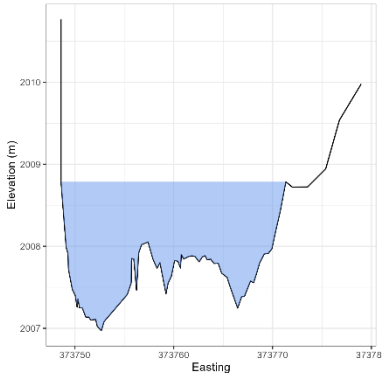

FC7 down

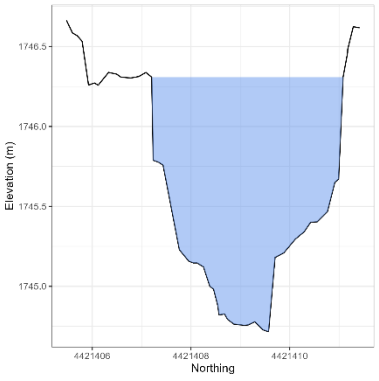

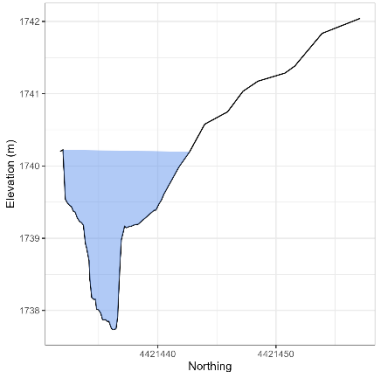

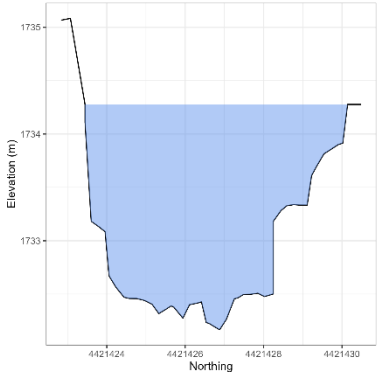

PC1 up

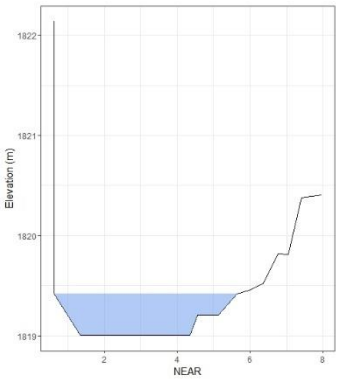

PC1 center

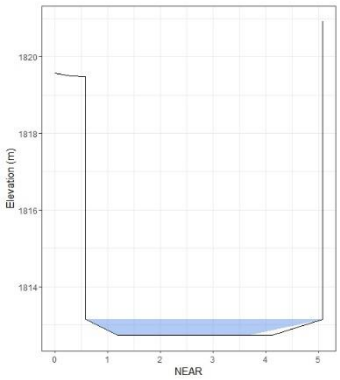

PC1 down

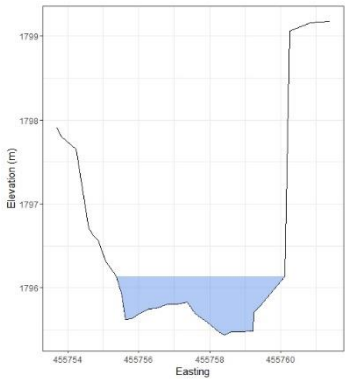

PC6 up

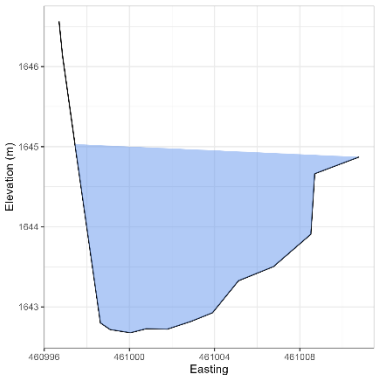

PC6 center

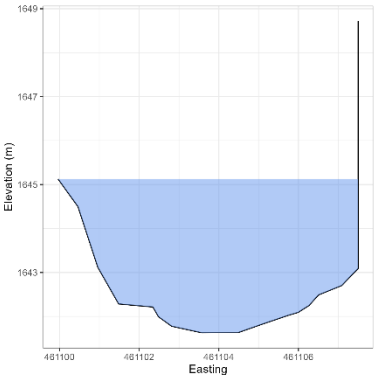

PC6 down

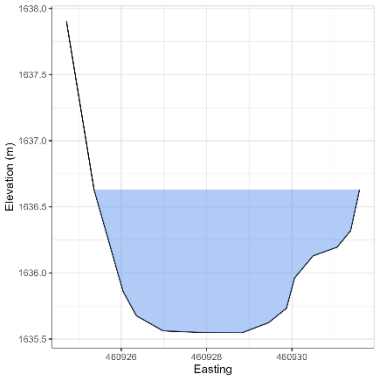

LF1 up

Not surveyed

LF1 center

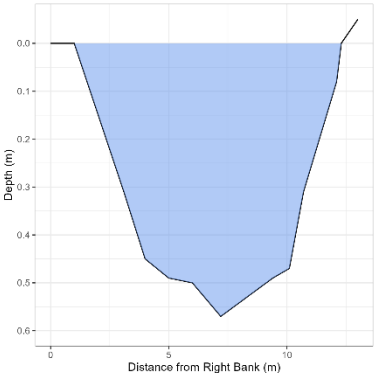

LF1 down

Not surveyed

S1 up

Not surveyed

S1 center

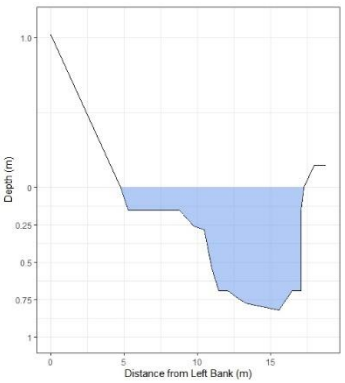

S1 down

Not surveyed

S2 up

Not surveyed

S2 center

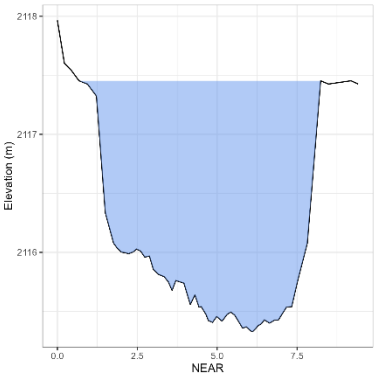

S2 down

Not surveyed

Sh1 up

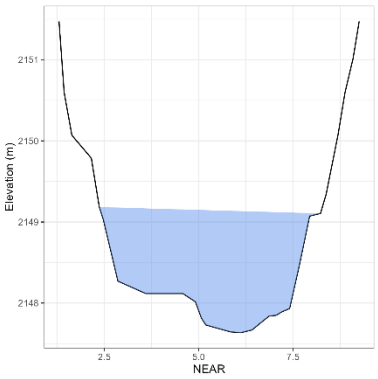

Sh1 center

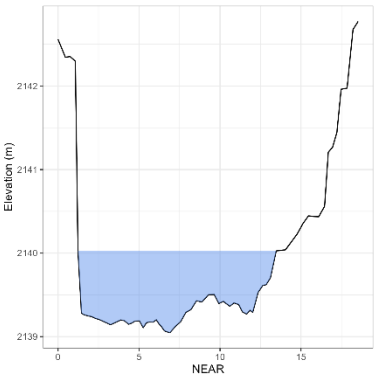

Sh1 down

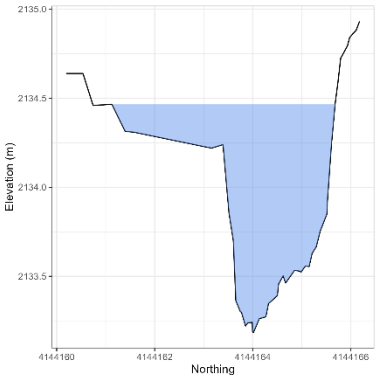

Sh2 up

Not surveyed

Sh2 center

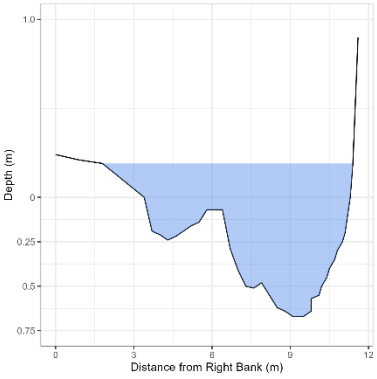

Sh2 down

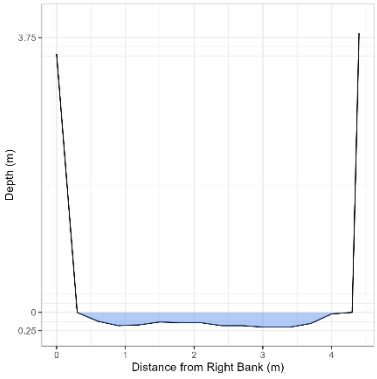

TM1 up August

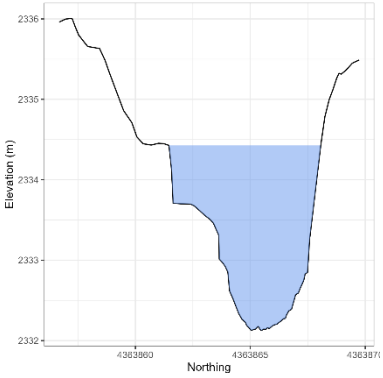

TM1 center August

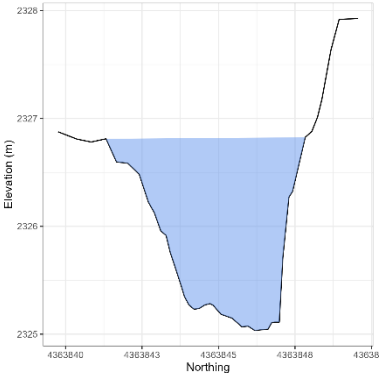

TM1 down August

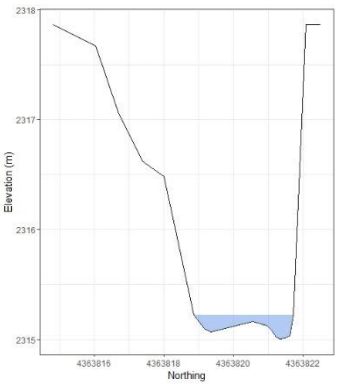

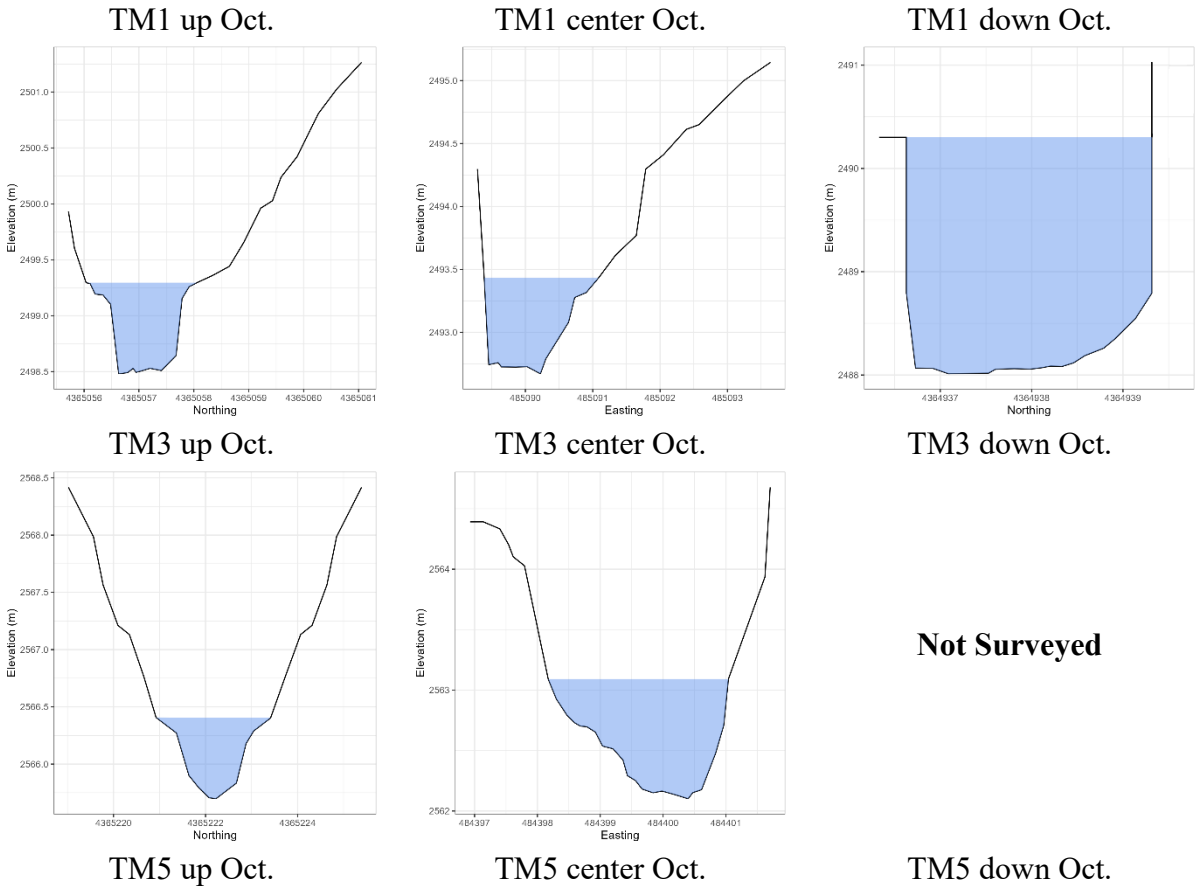

Figure D.3. Axial channel cross-sections surveyed in the field during summer 2023. Shaded light blue area represents the estimated bankfull cross-sectional area. Sites are labeled below the corresponding figure. Generally, the center cross-section represented the area where the debris flow toe was intersecting the axial river.